VIBRATIONALLY STATE SELECTED ION MOLECULE EXPERIMENTAL AND COMPUTATIONAL STUDIES OF BOTH REACTANT CHARGE STATES OF $[NO_2 + C_2H_2]^+$ AND HOD^+ WITH NO_2

by

Jason M. Boyle

A dissertation submitted to the faculty of
The University of Utah
in partial fulfillment of the requirements for the degree of

Doctor of Philosophy

Department of Chemistry

The University of Utah

May 2011

The University of Utah Graduate School

STATEMENT OF DISSERTATION APPROVAL

The dissertation of **Jason M. Boyle**

has been approved by the following supervisory committee members:

Scott L. Anderson	, Chair	**11/11/2010** Date Approved
Peter B. Armentrout	, Member	**11/11/2010** Date Approved
Michael D. Morse	, Member	**11/11/2010** Date Approved
Mark Ji	, Member	**11/11/2010** Date Approved
Jordan Gerton	, Member	**11/11/2010** Date Approved

and by **Henry S. White**, Chair of the Department of **Chemistry**

and by Charles A. Wight, Dean of The Graduate School.

ABSTRACT

Ion molecule studies have not only determined reactivity of systems that would have otherwise been unavailable, but also provide a perspective that improves the understanding of the mechanisms that drive reaction. Presented here are studies of three ion molecule systems one of which is accompanied by an extensive set of direct dynamics trajectory calculations. In the first system presented, NO_2^+ in six different vibrational states was reacted with C_2H_2 over the center-of-mass energy range from 0.03 to 3.3 eV. The effects of the symmetric bend overtone (02^00) excitation are particularly strong (factor of 4) while the delta overtone (02^20) effects are much weaker. A large set of quasi-classical trajectories were calculated at the PBE1PBE/6-311G** level of theory, in an attempt to understand the mechanistic origins of this observation. The trajectories reproduce experiment where comparable. Analysis of these trajectories resolves the mechanistic origins of this vibrational effect.

Similar experimental measurements were made for the first excited electronic state of this system where the charge is localized on the acetylene. The $C_2H_2^+$ reactant was prepared in four distinct modes. Because both reactants have one unpaired electron, collisions can occur with either singlet or triplet coupling of these unpaired electrons, and the contributions the three channels (charge, O^-, and O transfer) are separated based on distinct recoil dynamics. The effects of $C_2H_2^+$ vibration are modest, but mode specific.

Integral cross sections and product recoil velocity distributions were also measured for reaction of HOD^+ with NO_2, in which the HOD^+ reactant was prepared in its ground

state, and with mode-selective excitation in the 001 (OH stretch), 100 (OD stretch) and bend (010) modes. In addition, we measured the 300 K thermal kinetics in a selected ion flow tube reactor and report product branching ratios different from previous measurements. Reaction is found to occur on both the singlet and triplet surfaces with near unit efficiency. Origins of discrepancies in the thermal versus beam experiments are discussed. Nine mechanisms contribute to four product channels (proton, deuteron, charge, and O- transfer) with the contributions from each resolved. Vibrational effects allow determination of energy partitioning in proton and deuteron transfer reactions near the product ion dissociation threshold.

TABLE OF CONTENTS

LIST OF FIGURES

LIST OF TABLES

ACKNOWLEDGMENTS

I would like to thank Prof. Scott L. Anderson for his patient assistance in helping me become a more competent scientist as well as for the opportunity to work on this project. I am also grateful to the students in the Anderson group for their positive contributions towards my time here. Special thanks to Dr. Jianbo Liu for his close guidance, both experimentally and computationally, during the early portion of my graduate career. The chemistry department electronics and machine shops have been insightful, attentive and supportive. This journey would not have been the same without them. The faculty here at the chemistry department has been patient, available and incredibly helpful. I would also like to offer special thanks to the members of my committee.

Throughout my doctoral studies my personal life has grown as well. I met my beautiful wife, Joanna, and we have a healthy son, Quinten. Their support has greatly contributed to my sanity in trying times. I owe much of my life's direction and perspective to my late grandmother Geneva Moore who will always be in my thoughts. Finally, I would like to thank my parents who have never ceased to amaze me.

CHAPTER 1

INTRODUCTION

State specific molecular dynamics has proven useful to practical applications (chemical lasers and in the field of atmospheric chemistry), but its strong justification lies in fundamental details that advance the understanding of matter itself.[1] Molecular dynamics has provided a path to observe the details of single collisions that are unavailable in bulk reactions. Still, no single molecular collision is observed in isolation but instead a statistical average of single collisions.[2] This experimental development, coupled with modern computational techniques, has painted a much more complete understanding of reactivity.

The work here focuses on small ion-molecule reactions because in the pursuit of fundamental details it is desirable to have as much control of experimental parameters as possible. The details that lead to a better understanding of the nature of matter are more accessible in small systems, such as the ones presented here. Ion-molecule systems are amenable to chemical dynamics studies because of the high collection efficiency, control of collision energy, initial ion state preparation, product mass discrimination and easy product detection. Gas phase dynamics studies have revealed amazing complexity in small, seemingly simple systems.[3] Experimental and computational methods have improved over time to elucidate the details of ever more difficult systems. [4-6]

Experiments are carried out in a tandem mass spectrometer guided ion beam apparatus. The basic premise of the experiment is to guide a velocity-, mass- and vibrationally state-selected ion beam through a scattering cell containing a neutral molecule target. Reactant and product ions, contained in the ion guide, are passed

through a time-of-flight (TOF) region that allows for analysis of reactivity as well as reaction recoil dynamics. Reactant and products are observed individually to determine reactivity and product arrival time distributions. The interpretation of the intensity and distribution of ions as a function of experimental parameters provides a unique view of reactivity.

It has been suggested that the ultimate goal of computational molecular dynamics is to calculate the rate of reaction from first principles,[7] but the computational techniques used here do not attempt to predict the outcome of reactions or the reaction rates. Instead, we attempt to get computational results that qualitatively reproduce the available experimental observations to develop mechanistic insight. If the computational results reproduce the experimental observations, at least qualitatively, over many separate observations then we assume the computational results are appropriately modeling the "real" system. From there, the computational results can be utilized to examine details of the reaction that would not otherwise be available.

The application of this philosophy to state specific ion-molecule dynamics can be broken down into three parts. First, experimental results show us the nature of what happens in a molecular collision (see Chapters 3, 5 and 6). We measure reactivity, product branching and recoil dynamics as a function of reactant vibrational state and collision energy. From these measurements, along with product and reactant thermo chemical data, we can determine vibrational mode effects, product internal vs. translational energy partitioning, scattering dynamics and reaction complex lifetimes.[2]

Vibrational state selection of the reactant ion allows the properties of the early portion of the reaction coordinate to be probed, before the initial conditions are "forgotten". Molecular motion, by influencing passage through transition states, Frank-Condon factors and energy resonance, can strongly influence dynamics along the entrance coordinate of a collision, often nonstatistically. It is here, early in the reaction coordinate, before energy has the opportunity to be randomized, that reactant molecular motion, through vibrational state selection, can nonstatistically influence reactivity. These experimental observations, coupled with computation, help interpret the nature of the early reaction coordinate.

The second part of this story is geometry optimized single point energy and mode frequency calculations. Interpretations of experimental results are greatly advanced by this computational complement. Using an electronic structure modeling program a reaction coordinate (or lowest energy pathway from reactants to products) can be established through a combination of chemical intuition, trial and error initial geometries for optimization and other creative approaches. The typical ion-neutral pathway consist of a weekly bound reactant and product like complexes, transitions states, and often more strongly bound covalent complexes. Establishing a reaction coordinate is a very helpful tool and statistical methods can be used to determine if the reaction coordinate is in good agreement with experiment.[6] Furthermore, a credible reaction coordinate provides a way of visualizing the reaction. This can be incredibly helpful in interpreting the experimental results particularly when there is not a lot of available energy to the system.

However, as more energy is added to the system the lowest energy path is not as relevant because the system has access to higher energy portions of the potential energy surface.

Transition states (TS), or structures that facilitate transition between stable geometries, are crucial to the understanding of reactivity. For example, the transition state can be tight and restricting reactivity with high energy vibrational modes or it can be loose with low frequency modes so that large geometric distortions from the optimized transition state geometry can still pass through without excessive energy. Furthermore, the form of the potential on the entrance to a transition state determines how energy partitioning, such as vibrational state excitation, effects reactivity.[4,8] Branching is often determined by transition states and understanding the energy and nature of the TSs can help determine the source of experimental results as well. The energy and geometry of TS structures are insightful but the vibrational frequencies of the TSs along with total energy and complex geometry mode frequencies allow statistical methods to be employed, such as the Rice-Ramsperger-Kassel-Marcus (RRKM) theory, which can be used to get an estimate of the reaction rate that may be compared to experiment.[9] Clearly this computational insight to experimental results is of great benefit but much of the story is still out of reach. For example, experimentally strong vibrational effects are observed that cannot be explained through statistical methods (i.e., sometimes collision energy drives reactivity while vibrational energy inhibits it or a low energy mode enhances reactivity more than higher energy modes).

Single point calculations are inherently inaccurate and large discrepancies in energies exist amongst different levels of theory. The discrepancies do not constantly favor one

method over another and effort must be taken, such as benchmarking against known experimental values, to assure that the method is appropriate for the system being investigated. Furthermore, calculated vibrational frequencies and geometries may vary from the true structures even though the energies are reasonable.

The third and final part is a more complex system of calculations. Quasi-classical direct dynamic trajectory calculations[10-12] can be performed for many systems with good agreement with experiment.[13] These calculations distribute the available energy into quantum internal vibrational modes as designated and initiate collisions with a semi-random orientation and distribution of rotational energy. The reactants are given a defined intermolecular angular momentum and collision energy. The simulation program "steps" along the potential energy surface all the way through a molecular interaction by calculating potential energies, the gradients of those energies and atomic momenta. Due to the nature of the calculations, effects seen experimentally are often less apparent in calculations, as discussed in Chapter 4.

This allows investigation of how a potential surface facilitates nonstatistical dynamics such as vibrational mode effects that are not available from the lowest energy reaction coordinate. In Chapter 4, the results of quasi-classical direct dynamics trajectories elucidate how vibrational modes give atomic velocities and access to reactant geometries that facilitate passage through a tight transition state. The trajectories often avoid the deep well in the potential surface and show that the reactant vibrational state influences the complex formation in reactive collisions, thereby directly affecting recoil dynamics.[14] The change in recoil is qualitatively consistent with experiment. Without the trajectory

study it would not be possible to develop the in depth understanding of vibrational influence presented in Chapter 4. Nevertheless, some details remain evasive, such as smaller experimental effects that are not computationally reproducible.

The unique combination of experimental and computational techniques applied here to probe ion-molecule dynamics has advanced the understanding of molecular interactions. The discipline has come a long way in the last several decades making bigger and more complicated systems more accessible; yet it is through the studies of these smaller systems that we get the fundamental insight that lets us move forward to a more detailed understanding of larger systems. The thesis presented in the following chapters will work though some of the details of our contribution to the subject.

References

1. R. D. Levine and R. B. Bernstein, *Molecular Reaction Dynamics and Chemical Reactivity* (Oxford University Press, New York, 1987).

2. M. S. Child, *Molecular Collision Theory* (Academic Press, London and New York, 1974).

3. L. Paetow, F. Unger, W. Beichel, G. Frenking, and K.-M. Weitzela, J. Chem. Phys 132 (17), 174305/1 (2010).

4. J. C. Polanyi and W. H. Wong, J. Chem. Phys. 51 (4), 1439 (1969).

5. J. Liu, B. Van Devener, and S. L. Anderson, Journal of Chemical Physics 121, 11746 (2004).

6. J. M. Boyle, B. W. Uselman, J. Liu, and S. L. Anderson, J. Chem. Phys 128, 114304 (2008).

7. G. D. Billing and K. V. Mikkelsen, *Introduction to Molecular Dynamics and Chemical Kinetics* (John Wiley and sons, New York, 1996).

8. J. Liu, K. Song, W. L. Hase, and S. L. Anderson, J. Am. Chem. Soc. 126, 8602 (2004).

9. L. Zhu and W. L. Hase, A general RRKM program(QCPE 644) (Chemistry Department, Univeristy of Indiana, Bloomington, 1993).

10. M. J. Frisch, G. W. Trucks, H. B. Schlegel, G. E. Scuseria, M. A. Robb, J. R. Cheeseman, J. J. A. Montgomery, T. Vreven, K. N. Kudin, J. C. Burant, J. M. Millam, S. S. Iyengar, J. Tomasi, V. Barone, B. Mennucci, M. Cossi, G. Scalmani, N. Rega, G. A. Petersson, H. Nakatsuji, M. Hada, M. Ehara, K. Toyota, R. Fukuda, J. Hasegawa, M. Ishida, T. Nakajima, Y. Honda, O. Kitao, H. Nakai, M. Klene, X. Li, J. E. Knox, H. P. Hratchian, J. B. Cross, C. Adamo, J. Jaramillo, R. Gomperts, R. E. Stratmann, O. Yazyev, A. J. Austin, R. Cammi, C. Pomelli, J. W. Ochterski, P. Y. Ayala, K. Morokuma, G. A. Voth, P. Salvador, J. J. Dannenberg, V. G. Zakrzewski, S. Dapprich, A. D. Daniels, M. C. Strain, O. Farkas, D. K. Malick, A. D. Rabuck, K. Raghavachari, J. B. Foresman, J. V. Ortiz, Q. Cui, A. G. Baboul, S. Clifford, J. Cioslowski, B. B. Stefanov, G. Liu, A. Liashenko, P. Piskorz, I. Komaromi, R. L. Martin, D. J. Fox, T. Keith, M. A. Al-Laham, C. Y. Peng, A. Nanayakkara, M. Challacombe, P. M. W. Gill, B. Johnson, W. Chen, M. W. Wong, C. Gonzalez, and J. A. Pople, (Gaussian, Inc., Pittsburgh PA, 2003).

11. V. Bakken, J. M. Millam, and H. B. Schlegel, J. Chem. Phys. 111, 8773 (1999).

12. W. L. Hase, K. Bolton, P. de Sainte Claire, R. J. Duchovic, X. Hu, A. Komornicki, G. Li, K. Lim, D. Lu, G. H. Peslherbe, K. Song, K. N. Swamy, S. R. Vande Linde, A. Varandas, H. Wang, and R. J. Wolf, VENUS99: A general chemical dynamics computer program (1999).

13. K. Bolton, W. L. Hase, and C. Doubleday, Jr., J. Phys. Chem. B 103, 3691 (1999).

14. U. Lourderaj and W. L. Hase, J. Phys. Chem. 113, 17 (2008).

CHAPTER 2

EXPERIMENTAL

The differential and integral cross section measurements presented here were acquired in a home built tandem mass spectrometer guided ion beam apparatus shown in Figure 2.1. This is a pulsed experiment at 10 Hz. Each measurement is taken as follows. A pulse valve releases a plume of helium seeded with the reactant gas to generate a supersonic expansion. The coldest, fastest part of the plume is at the leading edge going directly forward. The center line of the plume then passes through a skimmer and into the ionization region. In the source region of the experiment, the laser beam, frequency tuned to a resonant vibrational mode of a reactant Rydberg state, intersects the leading edge of the molecular beam generating vibrationally state-selected ions. The position and kinetic energy of ions in the gas phase are controlled with electric fields. The nascent ions are given a little push by a repeller plate and are then guided and focused into the first quadrupole mass selector (QMS1). QMS1 removes any fragment ions that may have been generated during ionization. Between QMS1 and the first ocatupole ion guide (oct1) there is a split ion lens time-of-flight (TOF) gate (i.e., the lens is split into halves so that voltages can be individually applied to allow or prevent the passage of ions). The gate is opened for a (~10 μs) window to select a narrow temporal and kinetic energy distribution of the primary ion beam.

The ions from the source are injected into an octapole ion guide (oct1) that passes through a scattering cell where the neutral reactant is introduced. The energy of the ion beam can be controlled by the float voltage of the octapole. Unobstructed reactant ions as well as scattered reactant ions and product ions are contained in the ion guide and passed along to a longer TOF octapole (oct2) to allow product recoil analysis. The ions

exit the TOF octapole through an extraction lens and are focused into the second quadrupole mass selector (QMS2) so that one ion mass can be observed at a time. These mass selected ions are then focused through an Einzel lens onto a Daly detector where each ion pulse is counted by a 350 MHz multichannel scalar (MCS) controlled through in house programs. Due to noise related to the aging of the Daly detector it was switched to a Channeltron electron multiplier in the acetylene and water studies. Integral cross sections are calculated from the scattering cell pressure, the effective length of the scattering cell, the product ion counts and the reactant ion counts. Differential cross sections not only give a measure of reactivity and branching ratio from total ion counts but also give collision time and energy partitioning through ion time of arrival. What follows is an introduction to the concepts that make these state selected guided ion beam molecular dynamics studies possible.

Pulsed Jet Molecular Beam

The pulse valve (PV) chamber has been modified in the course of the work presented. For the $NO_2^+ + C_2H_2$ experiments a solenoid driven Parker valve, driven by a home built pulse generator, pulses gas to generate a molecular beam. The gas supply, from a lecture bottle, was a mixture of 5% NO_2 in Helium at up to 70 psi. There were no significant changes in beam velocity or rotational distributions between 40 to 70 psi backing pressure. The PV was mounted on the differential wall that separates the PV chamber form the source chamber ~1 cm from a 1.25 mm orifice skimmer. During operation, the pressure in the PV chamber is about 1×10^{-5} Torr while the source remains below $\sim 1 \times 10^{-6}$ Torr. The pulse width from each PV plume is around half a millisecond and

there is a second shorter plume of gas released from the poppet bouncing. The background pressure was maintained at less than 1 x 10^{-5} Torr to assure the skimmer is in the zone of silence where beam velocities are still greater than the speed of sound.[1] This worked very well for NO_2 ionization, because the ionization cross section is large and the wavelengths required for ionization are in a spectral region where laser power is not an issue.

Water is a more difficult ion to make for a couple of reasons. The ionization cross section is smaller, meaning that the laser power has to be increased to generate the same number of ions, and the wavelength required for ionization is more difficult to achieve with the required power. For these reasons, the pulse valve chamber and the PV itself were modified. The goal is to have the valve open fast so that the leading edge of the plume is dense and cold and to close fast to limit the amount of gas supplied to the chamber. Increasing the pumping speed in the PV chamber is also beneficial because it allows the valve to be driven harder, opening faster and releasing more gas while maintaining adequate background pressure.

The solenoid driven PV was replaced by a home built disc piezoelectric PV. This has the advantages of opening faster to supply an increased flow rate while also closing much faster (less than 100 μs) and it does not bounce. The piezoelectric PV is mounted on a xyz mount that is adjusted from outside vacuum making the alignment easier and allowing the PV-skimmer distance to be optimized during operation. Despite the decreased duty cycle of the piezoelectric PV the total gas load is increased primarily due to the increased PV orifice diameter and improved gas supply to the valve orifice. The

pumping speed was increased to account for the extra gas by replacing the chamber with a larger diameter chamber which changed the pump port from 8 inches to 10 inches and replacing an Edwards 160 vapor pump (600L/s) with an Edwards 250 vapor pump (1700L/s). This is the arrangement used in both the $C_2H_2^+ + NO_2$ and $H_2O^+ + NO_2$ systems presented in Chapters 5 and 6, respectively.

Laser Arrangement

The goal of this research is to analyze how molecular motions affect reactivity. To do this ions are generated with different vibrational states populated through resonant enhanced multi photon ionization (REMPI). The details of the two color REMPI scheme used in ionizing NO_2 have been discussed in detail previously.[2] To generate the two colors the second harmonic of a NY-82 continuum laser is split to pump two dye lasers, a Continuum ND 60 and a ND 6000. The NY-82 is a seeded Nd:YAG three rod high power pulsed laser running at 10 Hz generating 6 ns wide narrow line width 1064 nm light at up to 2 J/pulse. To pump the dye lasers this 1064 beam is frequency doubled to make an up to 950 mJ/pulse at 532 nm. Frequency doubling is a well established technique in which light responds to passing through a nonlinear media, here a KDP crystal, by effectively adding two photons together to make one photon with twice the energy.

The laser setup for producing state selected NO_2^+ ions had each dye laser pumped by ~350 mJ/pulse 532 nm doubled YAG radiation. Each of the dye laser fundamental frequencies is doubled and then aligned such that the two beams are copropagating and focused into the ion source. For C_2H_2 state selection, a single color frequency-doubled

dye beam is used, simplifying the setup significantly. For NO_2 and C_2H_2 it is possible to get well above 10 mJ/pulse for each color of resonant light, which is much more than what is needed. In the single color production of state selected water ions the fundamental of the dye laser is frequency-doubled and then this doubled light is summed with residual 1064 nm light from the YAG. Mixing after doubling is a distinctly more challenging task and for this reason the desired frequencies, ~230 nm, are much lower in intensity (4 mJ/pulse on a good day).

Resonance Enhanced Multiphoton Ionization

Vibrational state selection of the ion is made through resonance enhanced multiphoton ionization (REMPI) schemes with the details of each pathway used have been discussed in detail previously.[2,3] To get good ion state selection a multiphoton process is required to pump into a resonant transition of a bound Rydberg state followed by ionization due to a subsequent absorption. A Rydberg state is a bound electronic state near the ionization threshold, preferably with high angular momentum, so that the promoted electron does not interact strongly with the ionic core. The kinetic energy of the electron along with the ionization potential of the neutral precursor and laser frequency define the internal energy of the nascent ion.

For state exploration and state purity determination the guided ion beam experiment is convertible into an ion TOF mass spectrometer and a TOF kinetic energy analyzer for electrons. This is done by replacing the source with a field free μ-metal TOF tube that has interchangeable electrodes for ion and electron collections and a microchannel plate (MCP) detector. The electrode arrangement for ion collection utilizes Wiley-McLaren

space focusing to search for resonant nondissociative transitions. The laser frequencies are scanned while monitoring ion intensity to find resonant transitions. These transitions are then identified through photoelectron kinetic energy analysis and comparison to previously established literature.[4,5]

The purity of state selection in these transitions was checked by changing to a field free ionization region and monitoring electron kinetic energy through photoelectron spectroscopy. Electron collection efficiency is low, defined by the solid angle between the location of ionization and the one inch channel plate about a meter away (<0.5%). NO_2^+, $C_2H_2^+$ and H_2O^+ states and state purity are discussed in Chapter 3,5 and 6 respectively.

Ion Guides

The advent of ion traps to confine charged particles in inhomogeneous oscillatory electric fields in the 1950s and then the linear ion traps in the 1970s greatly enhanced the study of ion molecule reactions. In our tandem mass spectrometer guided ion beam apparatus there are five linear traps. One quadrupole ion guide, two quadrupole mass selectors (QMS1 and QMS2), and two octapole ion guides (oct1 and oct2). Each type of trap is utilized for its unique characteristics. The properties of each are briefly described below along with the purpose of its implementation in this experiment. The RF for the octapole and quadrupole ion guides was supplied by in house electronics.[6,7]

The principles of inhomogeneous electrical radio frequency fields for ion trapping and guiding have been evaluated in detail,[8,9] and discussed here in brief. Ion guides for low mass to charge operate by applying radio frequency (RF) oscillatory potentials with

opposite phase to n pairs of rods. For example in a four rod system (n = 2), or quadrupole, the rods opposite each other are shorted so that the electric potential applied to them are in phase while the potential applied to the other two rods are 180^{o} out of phase. This creates an environment where the potential along the centerline of the four rods overlap destructively making a nontime dependent field (i.e., constant potential equal to the average of the DC potential bias on the two sets of rods). Displacement from the center of the trap is characterized by an oscillatory field that is dependent on the displacement such that:

$$E_0(r,t) = E_0(r)\cos(\Omega t).$$

This time dependent field puts a force on the charged particle and the vector force has a component in the radial direction and magnitude proportional to its displacement. This generates a wiggling motion of the charged particle whose amplitude and frequency is dependent on the frequency and amplitude of the RF potential along with the ion displacement. The trapping arises from property that the field strength increasing with displacement form the center of the trap. The force is proportional to the second derivative of the position so it is being pushed towards the center of the trap when it is furthest from the centerline and it is being pulled from the center when it is closest to the center. The force is stronger when it is being pushed towards the center, because it is farther displaced from the center line, than it is when the charged particle is being pulled away from the center resulting in an effective potential (V^*) that pushes the particle towards the centerline. The effective potential is defined by:

$$V^* = \frac{1}{8}\frac{(qV_0)^2}{\varepsilon}\,(r/r_0)^{2n-2}$$

where q is the charge of the particle, V_0 is the amplitude of the RF at the electrode, ε is the characteristic energy, r_0 is the inscribed radius of the guide poles and n is the number of pole pairs. ε is defined as:

$$\varepsilon = \frac{1}{2n^2}\, m\omega^2 {r_0}^2$$

where ω is the angular frequency of the applied potential and m is the mass of the charged particle. The effective potential only traps the ions if the condition of the stability parameter (η)

$$\eta = \frac{(n-1)}{n}\,\frac{qV_0}{\varepsilon}\,(r/r_0)^{n-2}$$

is less than 0.3. This results because the amplitude of the fast wiggling motion is directly proportional to the value of η.

The motion of the charged particle in the trap can be determined from V^* if the trapping frequency is sufficiently high. Note that V^* depends on the number of poles. The quadrupole provides a quadratic trapping potential that is proportional to the square of V_0. This is useful for simultaneously guiding and focusing ions. Ions with significant radial velocity components are wiggling whenever they are much displaced from the center of the trap and well collimated ions with a narrow angular distribution remain close to the center of the trap. By going to a higher order linear trap, such as the octapole, where V^* is proportional to displacement to the sixth power, the area of the trap where V^* is small becomes larger allowing for less wiggling over a larger region and a larger pattern of the ions traveling the linear guide. This is preferred where focusing is

not a concern and where the energy distribution of molecular collisions is a concern. This is why octupoles are used to guide ions through the scattering cell and TOF regions.

Mass selection, here the quadrupole mass selector (QMS), is a unique application of inhomogeneous fields that consists of both a trapping, or stabilizing, RF field along with a static destabilizing DC field. By placing offset DC potentials on opposite sets of rods, a destabilizing field is made, yet the condition is dependent on the ion path. If we define the linear axis of the quadrupole trap as the z-axis, the plane that contains the center of the negatively charged poles as the yz –plane and the plane containing the positive poles as the xz-plane, then we will observe different behavior for positive ions in the xz and yz planes. Note that the centerline potential will be the average of the positive and negative pole potentials. This means that ions displaced from the centerline will not only encounter an RF potential gradient but also an axis dependant static potential gradient.

If the ion deviates in the y direction, from the static fields, it experiences a force towards the negatively charged pole extracting the ion. A restoring force applied by a RF potential can push the ions back but only if the ions are light enough so that the wiggling motion is large enough and therefore the effective potential is strong enough to push the ion back before It collides with the pole. If the ion is too heavy then the effective force will not be strong enough to restore the ion to the trap. Effectively the yz-plane acts as a low pass filter, allowing ions below a mass defined by the trap geometry, the RF and DC magnitude and the RF frequency to have stable trajectories.

In the xz-plane the DC potential pushes positive ions towards the center of the trap. The RF potential also restores the ions to the center of the trap but it is the combination of

the two forces that causes the amplitude of light ions to increase with time until the ion trajectory is no longer stable and the ion is lost. This creates a high pass filter only allowing ions above a mass to have a stable trajectory. It is the unique combination of the low pass and high pass filters in the QMS that allow for mass selection. QMS1 and QMS2 utilize the focusing attributes of the quadrupole to maximize ion transmission.

Scattering Cell

The ions are injected from the source into a 12 inch octapole ion guide (oct1). Oct1 guides the ions through a 10 cm long scattering cell where the neutral reactant is introduced. The rate of gas supply to the scattering cell is controlled by a leak valve and the pressure in the scattering cell is monitored by a capacitance monometer. A pneumatic valve diverts the gas flow between the scattering cell (cell on) and the chamber (cell off). The pressure difference between when the gas flow is going to the scattering cell and the background is the pressure used in to calculate the integral cross sections. Ion molecule collisions do occur outside the scattering cell but the rate of collisions outside the scattering cell does not change between cell on and cell off conditions. Integral cross sections are calculated from product ion cell on/cell off count subtraction to account for collisions that occur outside the scattering cell. The cell length used is the calibrated effective path length which is within 10% of the actual cell length.[10]

Data Acquisition

Mass selected reactant or product ion induced pulses are counted with a multi channel scalar (MCS) at up to 100 MHz limited by the pulse width. The P7882 FAST ComTec

MCS can count up to 350 MHz but the Channeltron electron multiplier generates pulses that are about 10 ns wide, limiting the count rate to less than 100 MHz. Ion pile up at the detector, resulting in multiple ions being counted as one, is only a potential problem when counting high energy reactant ions. As the energy of the reactant ion beam is increased the temporal distribution at the detector narrows. This is somewhat improved by slowing the ions through the source, but ultimately at high energy total reactant ion counts must be kept below ~4000 per second. The consequence of not accounting for all the reactant ions is an artificially high cross section yet, due to careful observation this was not an issue in the work presented here. Product ion arrivals are much more spaced out (up to 5 ms) and lower intensity and therefore ion pile up is not an issue in product ion counting.

References

1. G. Sanna and G. Tomassetti, *Introduction to Molecular Beams Gas Dynamics* (Imperial College Press, London, 2005).

2. B. Uselman, J. Liu, J. Boyle, and S. Anderson, Journal of Physical Chemistry **110** (4), 1278 (2006).

3. B. W. Uselman, J. M. Boyle, and S. L. Anderson, Chemical Physics Letters **440** (4-6), 171 (2007).

4. P. Bell, F. Aguirre, E. R. Grant, and S. T. Pratt, J. Phys. Chem. A **108** (45), 9645 (2004).

5. H. Dickinson, S. R. Mackenzie, and T. P. Softley, Physical Chemistry Chemical Physics **2**, 4669 (2000).

6. R. M. Jones, D. Gerlich, and S. L. Anderson, Rev. Sci. Instrum. **68**, 3357 (1997).

7. R. M. Jones and S. L. Anderson, Rev. Sci. Instrum. **71**, 4335 (2000).

8. P. H. Dawson, *Quadrupole Mass Spectrometry* (Elsevier Scientific Pub., Amsterdam, 1976).

9. D. Gerlich, Adv. Chem. Phys. **82**, 1 (1992).

10. Y.-H. Chiu, H. Fu, J.-T. Huang, and S. L. Anderson, J. Chem. Phys. **102**, 1199 (1995).

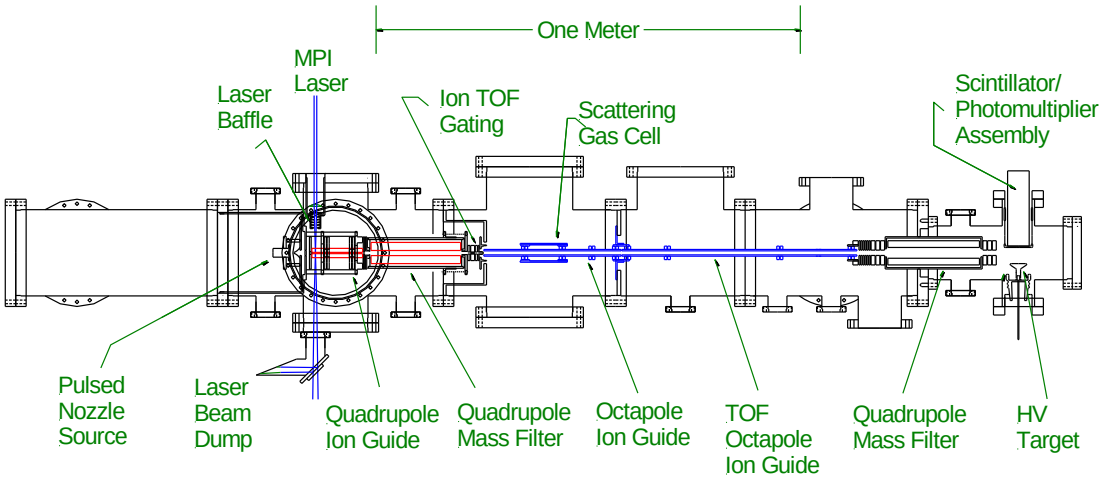

Figure 2.1. Tandem mass selecting guided ion beam experiment schematic.

CHAPTER 3

VIBRATIONAL EFFECTS ON THE REACTION OF NO_2^+ WITH C_2H_2: EFFECTS OF BENDING AND BENDING ANGULAR MOMENTUM

Overview

NO_2^+ in six different vibrational states was reacted with C_2H_2 over the center-of-mass energy range from 0.03 to 3.3 eV. The reaction, forming $NO^+ + C_2H_2O$ and $NO + C_2H_2O^+$, shows a bimodal dependence on collision energy (E_{col}). At low E_{col}, reaction is quite inefficient (<2%) despite this being a barrierless, exoergic reaction, and is strongly inhibited by $E_{col.}$ For E_{col} > ~0.5 eV, a second mechanism turns on, with efficiency reaching ~27% for E_{col}>3 eV. The two reaction channels have nearly identical dependence on E_{col} and NO_2^+ vibrational state, and identical recoil dynamics, leading to the conclusion that they represent a single reaction path throughout most of the collision. All modes of NO_2^+ vibrational excitation enhance both channels at all E_{col}; however the effects of bend (010) and bend overtone (02^00) excitation are particularly strong (factor of 4). In contrast, the asymmetric stretch (001), which intuition suggests should be coupled to the reaction coordinate, leads to only a factor of ~2 enhancement, as does the symmetric stretch (100). Perhaps the most surprising effect is that of bending angular momentum, which strongly suppress reaction, even though both the energy and angular momentum involved are tiny compared to the collision energy and angular momentum. The results are interpreted in light of *ab initio* and Rice-Ramsperger-Kassel-Marcus calculations.

Introduction

In studying complex reaction mechanisms, it is useful to have a variety of probes that each are sensitive primarily to different steps in the mechanism. In our approach to this problem, we use the effects of reactant vibrational excitation as a probe of the early time

dynamics, based on the idea that the initial mode of excitation is scrambled by any strong perturbations, such as formation of breaking of bonds.[1] Therefore, if significant mode-specific effects are seen, this implies that the rate-limiting step in the mechanism is early, and provides insight regarding which kinds of molecular motions are important. Product recoil velocity distributions probe reaction timescales, and disposition of the available energy into the products, i.e., the middle and late stages of the mechanism. When measured over a range of collision energies (E_{col}), and combined with theory, the mechanism can be unraveled in detail.[2,3]

While there is now a significant body of work probing effects of vibrational excitation mode on different classes of reactions, there is little information about the effects of vibrational angular momentum associated with bending of linear molecules. A number of studies of effects on energy transfer in low energy collisions have been reported[4]; however, we are aware of only two previous studies looking at effects on reactions. One, from our group,[2] studied energy transfer in NO_2^+-rare gas collisions leading to dissociation, and found a small but reproducible difference in dissociation cross section for the bend overtone state with, and without bending angular momentum. The other, from Kreher *et al.*[5] compared (among other states) the effect of exciting the (11^15) and (105) overtone combination band of HCN on the reaction with Cl to yield HCl+CN. Little difference was observed between the reactivity of the two states, even though both the bend quantum number and angular momentum changed. Here we report a very large (factor of ~2) effect of simply changing from the (02^00) state to the (02^20) state, even though both the energy difference (2 meV) and bend angular momentum are

negligible compared to the energy and angular momentum of the collisions.

Experimental and Computational Details

Experimental Details

NO_2^+ is produced by two color, three photon ionization, resonant at the two photon level with the E $^2\Sigma_u^+(3p\sigma)$ Rydberg state, as described previously.[6] State purity is measured by photoelectron spectroscopy to be better than 96% for all states probed in this study. The ionization scheme allows production of NO_2^+ in its ground state, with one quantum in any of the three vibrational modes, or with two quanta of bending excitation. The fundamental levels, labels, and energies are as follows: Symmetric stretch (1,0,0) 170meV, asymmetric stretch (0,0,1) 290meV, bend (0,1,0) 78meV. We can also produce ions in two levels associated with the overtone of the bend. The $(0,2^0,0)$ level (153 meV) corresponds to planar bending motion. The $(0,2^2,0)$ level (155 meV) corresponds classically to NO_2^+ having one quantum of bending each in the *xz* and *yz* planes, 90° out of phase, resulting in a molecule with fixed bend angle, rotating at the vibrational frequency.

The differential cross section measurements were made in a guided-ion beam scattering instrument described in detail previously,[7,8] along with our calibration and data analysis procedures. Briefly, a 1:5 mixture of NO_2 in He was passed through a pulsed valve, and the resulting molecular beam was collimated by a skimmer before entering the ionization region. Ionization occurred just inside the end of a radio frequency (rf) quadrupole ion guide that focused the ions into a quadrupole mass filter, which, for this system, was also operated as an ion guide (rf only). The time-of-flight (TOF) gating at

the end of this second quadrupole was used to narrow the temporal and kinetic energy distributions of the NO_2^+ reactant beam and to reject NO^+ fragment ions produced in the resonantly enhanced multiphoton ionization source. The state- and kinetic energy-selected ions were injected into an eight-pole rf ion guide, that guided them through a scattering cell filled with acetylene to 2 x 10^{-4} Torr. This pressure was chosen to provide reasonable signal for the small reaction cross sections in this system, while keeping multiple collision effects to an insignificant level. Unreacted NO_2^+ ions, together with any product ions, were collected by the ion guide, and passed into a second ion guide for TOF velocity analysis. Finally, the ions were mass analyzed and counted using a multichannel scalar (MCS). Integral cross sections were calculated from the ratio of product and reactant ion intensities, using the calibrated effective length of the scattering cell.[7] The width of the ion kinetic energy distribution (~ 0.15 eV) and zero of the center-of-mass collision energy (E_{col}) scale was measured by TOF. TOF was also used to measure the axial velocity (v_{axial}) distributions for the NO^+ and $C_2H_2O^+$ products, i.e., the projection of the full two-dimensional distributions on the ion guide axis.

The $NO_2^+ + C_2H_2$ reaction is quite inefficient, thus many data sets (cross sections versus vibrational state and collision energy) were required to achieve a reasonable signal-to-noise ratio. Because the measurements are time-consuming, a typical day's data do not include cross sections for all NO_2^+ vibrational states, however, each data set includes a measurement for ground state NO_2^+. In averaging data sets taken over a period of a month, we used the ground state cross section as an indicator of possible instrumental problems, such as potential barriers in the ion guides that block transmission

of low energy ions. If the ground state cross section for a particular day deviated by more than ten percent from the average of all the data sets, then *all* data from that day were discarded. The data presented are averages of the retained data sets, and error bars are taken from the standard deviations. The relative error in comparing cross sections for different states is estimated to be 15 %, which includes both random error, and our best estimate of possible sources of systematic error (e.g., day to day variations in ion beam energy distribution shape). In addition, we estimate about a 20% uncertainty in the absolute scale of the cross sections, due to factors such as uncertainty in the scattering cell pressure-length product and possible mass-dependence of the final mass spectrometer transmission efficiency.

Computational Details

To construct a reaction coordinate and to get energetic information, *ab initio* structure optimizations were performed at the B3LYP/6-311++G** level of theory, using GAUSSIAN 03.[9] For all stable structures found, the calculations were repeated at the MP2/6-311++G** and G3 levels of theory. The energetic trends for the three levels of theory were consistent. The B3LYP/6-311++G** level of theory was chosen because it best agrees with single point calculations done at the QCISD(T)/cc-pVTZ level of theory. Geometries were optimized calculating the force constants at every point. The resulting vibrational frequencies and zero-point energies were scaled by factors of 0.9613 and 0.9804, respectively.[9] All transition states (TSs) were verified to be first order saddle points by frequency calculations, and intrinsic reaction coordinate (IRC) calculations were used to determine which potential wells are connected by all the TS structures that

were found.

After standard TS-searching algorithms failed repeatedly to find a key transition state (TS2) for breakup of one of the intermediate complexes, we performed trajectory calculations to identify better starting geometries for TS searching. Trajectories were started at the equilibrium geometry of the complex, with randomly distributed internal energy equivalent to what the complex would have in a 1 eV collision. TS searches were then started from a number of likely looking high potential energy geometries, leading to identification of TS2, which was shown to be the desired TS by IRC calculations.

To examine the kinetic consequences of the various complexes and TSs, Rice-Ramsperger-Kassel-Marcus (RRKM) rate and density-of-states calculations were performed with the program of Zhu and Hase,[10] using its direct state count algorithm, and energetics, moments of inertia, and vibrational frequencies (scaled) from the B3LYP/6-311++G** calculation.

Results

Integral Cross Sections

Product ions are observed at masses 30 and 42 corresponding to O and O^+ transfer reactions,

$$NO_2^+ + C_2H_2 \rightarrow NO^+ + C_2H_2O \quad \text{(O transfer)} \quad \Delta H_{rxn} = -2.98 \text{ eV}$$

$$\rightarrow C_2H_2O^+ + NO \quad (O^+ \text{ transfer}) \quad \Delta H_{rxn} = -2.62 \text{ eV}$$

where the energetics are experimental,[11] and refer to the most stable structure of the $C_2H_2O^{(+)}$ product in each case (see below). Note that the two channels differ only in which product carries the charge, i.e., they are simply the lowest two electronic states of

$[NO + C_2H_2O]^+$. The integral cross sections for O and O^+ transfer in reaction of ground state NO_2^+ with C_2H_2 are shown in Figure 3.1, over the center-of-mass collision energy (E_{col}) range from 0.03 to 3.5eV. Also shown in the inset are the total reaction cross section (σ_{total}), and an estimate of the collision cross section ($\sigma_{collision}$), taken as the greater

of the capture cross section ($\sigma_{capture}$) and the hard sphere cross section ($\sigma_{hardsphere}$). $\sigma_{hardsphere}$ was calculated from the orientation-averaged contact radii of NO_2^+ and C_2H_2,assuming covalent radii for each atom, and exceeds $\sigma_{capture}$ for E_{col} > 2.5eV.

The two channels have similar dependence on E_{col}, although O transfer dominates over the entire range of E_{col}, with O/O^+ transfer branching ratios ranging from ~6 at low E_{col}, dropping to ~2 for E_{col} around 1 eV, then returning to ~4 for high E_{col}. The fact that the cross sections rise sharply with decreasing E_{col} at low E_{col}, shows that both channels are barrierless (i.e., there are no barriers on the reaction coordinate in excess of the reactant energy). Nonetheless, reaction efficiency, i.e., $\sigma_{total}/\sigma_{collision}$, is only ~2 % at our lowest energy point (~0.03 eV). Reactivity falls sharply with increasing energy, such that for E_{col} near 0.4 eV, the reaction efficiency is only ~0.5 %. At higher energies, both channels are enhanced by collision energy, such that the reaction efficiency reaches 27 % at our highest energy point. This pattern suggests the presence of a severe bottleneck to reaction, and that collision energy inhibits passage of the bottleneck for E_{col} < 0.4 eV, but allows the system to bypass the bottleneck at higher E_{col}.

Computational Results

The *ab initio* results for the $NO_2^+ + C_2H_2$ system are summarized in Figure 3.2 and Table 3.1. One important point is that there are two isomers of both C_2H_2O and $C_2H_2O^+$,

giving rise to four possible product channels. For both C_2H_2O and $C_2H_2O^+$, the ketene (H_2CCO) isomer is substantially more stable than the ethynol (HCCOH) isomer, although all four channels are exoergic. The energetics used in Figure 3.2, are experimental[11] for reactants and for the ketene isomer of the product channels. Energetics for complexes, transition states and the ethynol product isomer ($[NO + HCCOH]^+$) are from B3LYP/6-311++G** calculations.

Four complexes that might mediate reaction were found. There is an electrostatically bound reactant-like complex (RC) ~0.5 eV below the reactant energy. In this complex, the charge is partly delocalized, such that the Mulliken charges are 0.66 and 0.34 for the NO_2 and C_2H_2 moieties, respectively. The partial charge transfer in RC is reflected by an ONO bond angle (155°) that is intermediate between the values calculated for NO_2^+ (linear) and NO_2 (134°) at this level of theory. Because this complex can form from reactants with no rearrangements, no barrier to its formation is expected.

Complexes PC1 and PC2 are analogous electrostatically bound complexes of the ketene and ethynol isomeric products, respectively, each bound by ~1 eV with respect to the corresponding product asymptotes. In PC1, the Mulliken charge is nearly equally shared between the NO and H_2CCO moieties while in PC2 the NO moiety carries ~65% of the charge. Because the dissociation energies of PC1 and PC2 to products are small compared to the available energy (> 0 eV for all E_{col}), their lifetimes will be short, and they are unlikely to be dynamically significant. In addition, such product-like complexes clearly come after the rate-limiting step on the reaction coordinate, and therefore cannot influence the measured vibrational or collision energy effects on reactivity. The high

energy and tightness of TS3, compared to the orbiting TSs governing dissociation of PC1 to $[NO + H_2CCO]^+$ products, implies that both kinetic and energetic factors should strongly favor the ketene isomeric products. Therefore, the ethynol ($[NO + HCCOH]^+$) product channels are expected to be negligible at all collision energies.

In addition to these weakly bound electrostatic complexes, there is a covalently bound, five-membered ring complex ("ring") with C_{2v} symmetry and a binding energy of ~3 eV with respect to reactants. We were unable to locate any stable covalently bound complexes where only a single CO bond is formed (see below). The ring complex can be accessed from RC by rotating the reactants into a C_{2v} geometry, then passing over TS1, which lies only 0.18 eV above RC. The imaginary vibrational frequency corresponding to the reaction coordinate at TS1 is ~70 cm^{-1}. Calculation of the IRC connecting the ring to PC1 via TS2 indicates that as the ring falls apart, first one C-O bond breaks, then the N-O bond breaks at TS2, which then rearranges by a 1,2-hydrogen shift, yielding PC1. PC1 can then form the ketene product channels, with no barrier in excess of the dissociation energy. The minimum energy reaction path outlined here (reactants→RC→ TS1→ring→TS2→PC1→products) is consistent with the experimental finding that the reaction is barrierless. To account for the very low reactivity and unusual E_{col} dependence, we need to consider the kinetics expected for such a reaction path, as discussed below.

Recoil Velocity Distributions

TOF data were collected for product ions at a series of collision energies and for each vibrational state. Lab frame axial velocity (v_{axial}) distributions for the NO^+ product of the

O transfer channel are given in the top four frames of Figure 3.3, for E_{col} ranging from 0.41 to 3.35 eV. Because the cross section for $C_2H_2O^+$ production (O^+ transfer) is so small, only the v_{axial} distribution for E_{col} = 3.35 eV is shown (bottom frame). The points are the raw v_{axial} data, and the smooth curves are fits based on simulations of the experiments (*vide infra*). The solid vertical lines in each frame indicate the lab velocity of the center-of-mass frame, averaged over the collision energy distribution ($<V_{c.m.}>$).

The dashed vertical lines indicate the product ion velocities predicted by the spectator-stripping mechanism V_{SS}.[12] Axial velocity (v_{axial}) distributions are simply projections of the full velocity distributions on the ion guide axis. Because our experiment is axially symmetric, the lab frame v_{axial} distributions can be approximately converted to the center-of-mass (c.m.) frame simply by subtracting $<V_{c.m.}>$. The raw laboratory-frame v_{axial} distributions, thus, provide useful dynamical insight. For example, if reaction is mediated by a complex with lifetime ($\tau_{collision}$) greater than its rotational period ($\tau_{rotation}$), the resulting v_{axial} distribution must be symmetric about $<V_{c.m.}>$. Conversely, an asymmetric v_{axial} distribution is a clear sign that reaction is direct (i.e., not complex-mediated), and also reveals the dominant scattering mechanism (i.e., forward versus. backward scattering). Finally, some insight into the partitioning of available energy into product recoil can be inferred from displacement of the v_{axial} distribution with respect to $<V_{c.m.}>$.

There are a few limitations of this technique, as implemented here. Product ions that are strongly backscattered in the c.m. frame may have negative lab frame velocities. To collect such ions, the lens at the ion guide entrance is biased positive relative to the guide

potential, reflecting these ions toward the detector. The reflected ions arrive at long flight times, appearing as if they had low, but positive laboratory velocities. In addition, the slowest ions are most likely to have their velocities perturbed by small inhomogeneities in the surface potentials on the ion guides or by secondary collisions. Finally, these distortions in the low velocity portion of the v_{axial} distributions are exacerbated by the singular TOF-to-velocity Jacobian. For these reasons, v_{axial} data below 500 m/s are given zero weight in the fitting process used to extract information from the distributions. Here, the problem is serious only for low E_{col} (because $V_{c.m.}$ is small), therefore we show and analyze data only for $E_{col} > 0.4$ eV.

For ground state reactant ions at high E_{col}, the velocity distribution for NO^+ from the O-transfer channel is asymmetric (Figure 3.3, second frame from bottom), peaking well forward of (i.e., faster than) $V_{c.m.}$, but with a substantial tail extending into the backward (slower than $V_{c.m.}$) direction. The bottom frame shows that the corresponding distribution for the O^+ transfer channel is also asymmetric, but backward peaked relative to $V_{c.m.}$. Note, however, that we define "forward" and "backward" as product *ions* with lab velocity greater or smaller, respectively, than $V_{c.m.}$. Therefore, in comparing a pair of channels like $NO^+ + C_2H_2O$ and $C_2H_2O^+ + NO$, the dynamical sense of forward/backward is reversed. In this case, the velocity peak for both channels corresponds to small angle scattering, i.e., to a mechanism wherein NO_2^+ transfers O or O^+ to the C_2H_2 reactant, with the NO^+ or NO product continuing along in the same general direction as the original velocity of NO_2^+ reactant. As E_{col} is reduced, the distributions become increasingly symmetric, and by 0.4 eV, the distribution is forward-backward symmetric within

experimental error. Because of the small cross section for O^+ transfer, and kinematics that are less favorable for resolving structure in the $C_2H_2O^+$ v_{axial} distribution, it is not possible to say if the same transition to symmetric distributions occurs for the $C_2H_2O^+$ product.

To extract a more quantitative picture, it is necessary to fit the data, thereby correcting for the broadening that results from the distributions of NO_2^+ and C_2H_2 reactant velocities. Our fitting program and procedures have been described previously.[7] In essence, a model recoil velocity distribution is assumed, and then run through a Monte Carlo simulation of the experiment to include the effects of all broadening factors. The resulting convoluted v_{axial} distribution is compared with experiment, and the input parameters of the model are varied to optimize the fit. Because the data are only projections of the full velocity distribution, it is important to use a model that is physically reasonable, but which depends on only a few parameters. Here, both the v_{axial} and RRKM results suggest that the mechanism may involve a short-lived complex at low E_{col}, transitioning to direct scattering with increasing energy.

The osculating complex model[13] was developed to describe angular distributions in just such systems, and has been used here for that purpose. In the model, a fleeting complex is assumed to form, with lifetime $\tau_{complex}$ and rotational period $\tau_{rotation}$. It is also assumed that in absence of any complex rotation, the products would scatter at some particular angle, θ_{peak}, here assumed to be either 0° or 180°, depending on whether the measured distribution is forward or backward peaked. The rotation of the complex broadens the angular distribution, and the extent of measured forward-backward

asymmetry determines the ratio $\tau_{collision}/\tau_{rotation}$. Because $\tau_{rotation}$ can be estimated from the moment of inertia of the complex and the available angular momentum, the forward-backward asymmetry is directly related to the complex lifetime. Assuming a complex like RC in Figure 3.2, $\tau_{rotation}$ drops smoothly from ~0.9 ps at E_{col} = 0.1eV to ~0.4 ps at E_{col}=3.0 eV. The other input needed to simulate the recoil velocity measurements is a model for the recoil energy distribution, P(E_{recoil}). Here, P(E_{recoil}) is assumed to be a Gaussian parameterized in terms of the energy available to the products (E_{avail}). The parameter describing the peak fraction of E_{avail} going into recoil (f_{peak}) is constrained by the measured displacement of the v_{axial} peak from $V_{c.m.}$. The fractional width parameter (f_{width}) is constrained by the shape of the high (or low) v_{axial} fall-off. In summary, the model is physically reasonable, all four parameters are dynamically significant, and each is constrained by a different feature of the measured v_{axial} distributions.

The fits are shown as solid curves in Figure 3.3, and the corresponding fit parameters are summarized in Table 3.2. It is important to note that the fit shown for the $C_2H_2O^+$ channel at 3.35 eV was done using the same parameter values that gave the best fit to the NO^+ channel at the same E_{col}, with the exception that θ_{peak} was taken as 180°, rather than 0°. In both cases, the parameters correspond to short collision times, 19% of E_{avail} in recoil, and a propensity for small angle scattering. Clearly the O and O^+ transfer channels have very similar recoil dynamics, at least for high E_{col}.

Vibrational Effects

All modes of NO_2^+ vibrational excitation enhance both O and O^+ transfer reactions at all collision energies, albeit with strong dependence on vibrational mode. To better show

the vibrational effects, Figure 3.4 gives vibrational enhancement factors for each NO_2^+ reactant state plotted against the vibrational energy, E_{vib}. Each point corresponds to a particular NO_2^+ reactant state, indicated by the labels. The enhancement factors are simply ratios of the cross section for reaction of a particular state $\sigma(v^+)$ to the cross section for reaction for the ground state $\sigma($gs). Results are shown for three E_{col} ranges of interest, and to reduce the uncertainties in the ratios, the data for E_{col} points within each range were averaged. Error bars are the standard deviations. Where not shown, they are smaller than the height of the symbols. Note that both the magnitudes and mode dependence of the vibrational effects are nearly identical for O and O^+ transfer, again suggesting that the channels are dynamically linked. Because the larger O- transfer cross sections lead to smaller uncertainties, we will focus the discussion on that channel. Note that while all modes enhance both reactions, the relative effects (*per* unit E_{vib}) of NO_2^+ bending excitations ((0,1,0) and (0,2,0)) are much greater than those of the symmetric (1,0,0) and asymmetric stretch (0,0,1) modes. There is also a substantial difference in the effects from excitation of the $(0,2^0,0)$ and $(0,2^2,0)$ states, even though they differ by only ~3 meV in energy.

Figure 3.5 shows the effects of NO_2^+ vibrational excitation on the NO^+ v_{axial} distributions for E_{col} = 3.35 eV. Vibrational effects on the distributions for other collision energies above 1 eV are similar, although the distributions gradually become less forward peaked, as shown in Figure 3.3. Detailed comparison at energies below 1 eV was not attempted because the v_{axial} distributions are relatively featureless (Figure 3.3). The data for each vibrational state are scaled such that the integral under each curve is proportional

to the measured integral cross section for that state. For the (000) and (02^00) states, the raw data are shown as large filled symbols, along with curves obtained by smoothing the data. For the other states, where the distributions overlap and are hard to follow because of noise in the raw data, we show only the smoothed data, plotted with small, open symbols to allow the three curves to be distinguished. Excitation of all four excited states preferentially enhances the forward-scattered component of the v_{axial} distribution, such that the ratio of forward-scattered to backward-scattered intensity increases from ~1.8 for the ground state, to ~3.5 for the (02^00) state, with the other states lying in between.

In addition, it can be seen that different reactant modes have different effects on the shape of the distributions. For example, excitation of either bend overtone ((02^00) or (02^20)) shifts the corresponding v_{axial} distribution to higher velocities such that it peaks at the spectator stripping velocity, V_{SS}. The two stretch excitations ((100) or (001) give enhancement factors similar to that for (02^20) excitation, however, the v_{axial} distributions continue to peak well below V_{SS}, similar to that for the ground state.

Discussion

The NO_2^++C_2H_2 reaction was previously studied, both experimentally and computationally, by Bernardi et al.[14] The experiments included Fourier transform-ion cyclotron resonance measurements using charge transfer with Xe^+ to produce NO_2^+ ions with $E_{internal}$ < ~2.5 eV. It is likely that much of this excitation was in the bend mode, owing to the bent-to-linear geometry change when NO_2 is ionized. For some experiments, the NO_2^+ was collisionally relaxed prior to reaction. They did not report rate constants or branching ratios, but stated that both NO^+ and $C_2H_2O^+$ product channels

were observed for internally hot NO_2^+, but that only NO^+ was seen if the NO_2^+ was relaxed. Based on our results, which extend down to the thermal kinetic energy range, we suspect that they simply did not have the sensitivity to see the minor $C_2H_2O^+$ channel for ground state reactants. Given the enhancements we observe for modest levels of NO_2^+ vibrational excitation, it is likely that their reaction rates for hot NO_2^+ were large enough for both channels to be detected.

Bernardi *et al.* found three reaction pathways at the MP2/6-311+G* level linking the reactants to the observed product masses, all of which correlated to the ketene product isomer. In our study at the B3LYP/6-311++G** level, we only found the pathway (also found by them) through the five-membered ring complex shown in Figure 3.2. The other pathways involve intermediates such as four-membered rings that we found to be unstable or well above the reactant energy at the B3LYP/6-311++G** level. From their Meta-stable Ion Kinetic Energy Spectroscopy study of decomposition of $C_2H_2NO_2^+$, they concluded that the five-membered ring pathway is the only one significant in this reaction, and as shown below, this single pathway is sufficient to account for our measurements as well. Further discussion of the effects of theoretical method on the computed reaction coordinate(s) are given in the Chapter 4 study exploring this system with trajectory methods.

Product Channel Coupling and Branching

One aspect of the reaction mechanism for this system that appears to hold across the entire E_{col} range probed, is that the O and O^+ transfer channels are strongly coupled. The two channels have similar E_{col} dependence (Figure 3.1), vibrational effects (Figure 3.4),

and product scattering dynamics (Figure 3.3). Mode specific effects probe early time dynamics, before collisional interactions have scrambled the initial mode of excitation. The recoil dynamics probe both collision time scale (forward-backward asymmetry) and energy partitioning into the products ($P(E_{recoil})$). The similarities between the channels indicate that the channels are coupled throughout most of the collision process, and such a picture is consistent with the reaction coordinate shown in Figure 3.2. In essence, the reaction takes place on a single potential surface up to PC1, with charge delocalized as long as the interreactant or interproduct separation is small. It is only when the products finally separate that the charge has to localize on either the NO or C_2H_2O moieties, and because localization is so late in the collision, the two channels show nearly identical dynamics. In this scenario, we might expect that the branching between $NO^+ + C_2H_2O$ and $C_2H_2O^+ + NO$ channels should be controlled largely by the relative energetics in the two channels, which favor NO^+ production by 350 meV. Experimentally, the $NO^+/C_2H_2O^+$ branching ratio falls with increasing E_{col} from ~6 at our lowest E_{col} to ~2 for E_{col} between 1 and 2 eV, then increases again to ~4 at E_{col} = 3.2 eV.

If branching is controlled by product channel energetics, then statistically the branching would simply reflect the ratio of the densities of states (DOSs ratio) for the two channels. The DOS ratio will clearly fall with increasing E_{col} as the energy difference between the channels (350 meV) becomes small compared to E_{avail}. Note, however, that even at our lowest E_{col}, 350 meV is less than 12% of E_{avail}, thus the experimental branching ratio (~6) seems surprisingly large. To estimate the DOS ratio more quantitatively, we calculated the DOS for the $NO^+ + C_2H_2O$ and $NO + C_2H_2O^+$ channels,

using the experimental energetics, scaled vibrational frequencies from the *ab initio* results, orbiting TSs for both channels, and the direct state count algorithm in the RRKM program of Zhu and Hase.[15] The resulting ratio falls smoothly from ~2.5 at our lowest E_{col} to ~1.8 at E_{col} =3 eV. In other words, the DOS ratio is about a factor of 2 smaller than the experimental branching ratio at low E_{col}, and less strongly dependent on E_{col} – both factors consistent with the fact that the channel energy difference is small compared to the exoergicity. We conclude that statistical factors probably account for some of the measured propensity toward the $NO^+ + C_2H_2O$ channel in the $E_{col} \leq 2$ eV range, but that other factors are probably also at work.

The observed doubling of the branching ratio as E_{col} increases from 2 to 3.3 eV is clearly opposite to the trend expected from a statistical perspective. A possible contributing factor is collision-induced dissociation (CID) ($NO_2^+ + C_2H_2 \rightarrow NO^+ + O + C_2H_2$), contributing only to the NO^+ branching. CID has a threshold of 2.85 eV for the spin-forbidden channel producing $O(^3P)$, whereas the spin-allowed channel is inaccessible in our study [E_0 for O (^1D) production = 4.82 eV]. We recently studied CID of NO_2^+ in collisions with rare gases,[2] and found that the spin-forbidden channel is reasonably efficient for Xe, presumably due to the strong spin-orbit coupling in this fourth row atom; however, for Kr and the lighter rare gases, only the spin-allowed channel is observed. In fact, for Ne and Ar, the CID cross section is insignificant for E_{col} below ~8 eV, thus it seems unlikely that CID contributes significantly to the NO^+ signal or branching ratio for the energy range here.

A factor that may well influence product branching is vibrational dynamics in the exit channel. For example, the NO^+ bond length[16] is ~0.09Å shorter than that of NO, thus the relative energetics of the two channels will vary depending on how the NO moiety is distorted as the product separation distance reaches the critical range where the charge must localize. Similar arguments apply to distortions of the H_2CCO moiety. Vibrational dynamics this late in a rearrangement reaction are expected to essentially unaffected by the reactant vibrational state, consistent with the negligible effects observed of reactant state on product branching ratio. On the other hand, it is not unreasonable to expect that as the products separate from a high energy, constrained geometry such as TS2, the potential surface may impart particular vibrational motions that might significantly influence branching, and because the product separation dynamics and timescale will change with E_{col}, these effects may vary non-monotonically.

Regardless of what factors control branching, it is clear that the O and O^+ transfer channels are coupled well past the rate-limiting point on the reaction coordinate. Therefore, in the balance of this discussion, we will treat them as a single channel. For most purposes we will focus on the $NO^+ + C_2H_2O$ data, because the larger signal allows more detailed analysis.

Reaction Mechanism at Low Collision Energies

It is apparent in Figure 1, that reactions at low and at high E_{col} occur by different mechanisms, and that neither mechanism is efficient at energies between about 0.3 and 0.5 eV. We focus first on the low E_{col} mechanism.

The fact that the low E_{col} reaction efficiency rises sharply with decreasing E_{col}, but remains quite inefficient (~2%), implies a bottleneck to reaction, passage through which is strongly inhibited by E_{col}. TS1, with its need to make two simultaneous CO bonds, is a plausible candidate for such a bottleneck. We tested this hypothesis by exploring the potential energy surface near TS1, using single point calculations at the B3LYP/6-311++G** level to map how the energetics change as the structure is distorted in various ways. Note that TS1 is only ~0.4 eV below reactants, thus small changes in energy are sufficient to block passage for low E_{col}. The results are given in Figure 3.6, where the energies are all referenced to TS1. In essence, any distortion that prevents simultaneous formation of both nascent CO bonds raises the energy significantly, particularly if one CO distance is shortened significantly (curve A) while the other remains at the long distance found in TS1 (2.60 Å). Note also that it is important for the NO_2 moiety to bend such that the N atom is away from the C_2H_2. In any geometries where the N atom is bent toward C_2H_2, even at long inter-reactant separation, the energy is substantially higher. The exception is if angle C is reduced enough to allow C-N bond formation, the energy drops, however, this is a mechanistic dead end, i.e., does not lead to products. We conclude that the strong dependence of energy on geometry around TS1 is sufficient to account for the low reactivity.

The increase in reaction efficiency at high energies is clearly consistent with Figure 3.6 – given enough energy the system can react in a wide range of geometries. The sharp increase in efficiency at very low energies requires a different enhancement mechanism. A plausible scenario is that a complex mediates reaction at low energies, providing time

for the reactants to find their way through TS1 along the minimum energy path. The forward-backward symmetric v_{axial} distributions at low E_{col} are necessary, but not sufficient evidence supporting complex mediation at energies up to ~0.5 eV. The question is whether any of the complexes on the reaction coordinate are stable enough to support a mechanistically significant complex.

RRKM calculations were performed for all the complexes shown in Figure3.2, using vibrational energies and rotational constants from the B3LYP/6-311++G** calculations. For decay of RC to reactants and of PC1 and PC2 to products, we assumed orbiting transition states, and otherwise used TS1 - TS3 as appropriate. To estimate the angular momentum in the complexes, we assumed complex formation governed by capture, i.e., used the impact parameter-weighted average angular momentum for capture collisions at each energy. As suggested above, the product-like complexes PC1 and PC2 are mechanistically insignificant, i.e., decay is 100% to the corresponding products, and the RRKM lifetimes are negligible. Figure 3.7 gives the RRKM results for both the RC and ring complex. We give the complex lifetimes and the forward-branching ratio, i.e., the fraction of complex decay that tends to carry the system toward products, as opposed to back to reactants. Also shown are the rotational period of the complex and the "fly-by" time, given as a measure of how long a “direct” collision would last at the same collision energy. The fly-by time was arbitrarily taken as the time for reactants to move 5 Å relative to each other – surely an upper limit on the time during which strong inter-reactant forces would be active in a direct encounter.

The ring complex is stabilized by relatively large barriers at TS1 and TS2, resulting in a lifetime longer than the rotational period for E_{col} up to ~1 eV. This complex, therefore, could account for the forward-backward symmetric v_{axial} distributions observed at low $E_{col.}$ Note, however, that the forward branching ratio for the ring complex is near unity over this energy range, i.e, if a statistical ring complex forms at low collision energies, it almost always goes on to products. In that case, the rate-limiting step has to come before the Ring complex, therefore this complex cannot affect reactivity, including the low E_{col} reactivity spike and vibrational effects.

The RC is weakly bound, and has a mechanistically significant lifetime ($\tau_{complex} > \tau_{Fly\text{-}by}$) only for E_{col} below 0.1 eV. Furthermore, the forward-branching ratio falls off quickly with energy, such that RC decay would contribute little to the net product signal above 0.1 eV. Experimentally, the low E_{col} reactivity spike is somewhat broader than 0.1 eV, however, we note that there is a ~170 meV collision energy distribution at low E_{col}, implying that the actual reactivity spike is quite sharp. We conclude, therefore, that mediation by this weakly bound reactant-like complex is sufficient to account for the low E_{col} mechanistic component. Furthermore, comparing the forward branching ratios for RC and Ring complexes, it is clear that the rate-limiting point, at least in a statistical mechanism, is TS1, i.e., formation of the ring complex. Finally, while RC enhances reaction probability at E_{col} <0.1 eV, it cannot account for symmetric v_{axial} distributions up to ~0.5 eV. It seems, therefore, that both complexes are important at low E_{col}, with RC controlling reactivity, and the ring complex stretching the collision time sufficiently to account for the forward-backward symmetry.

The properties of RC and TS1 appear sufficient to account for the strong inhibition by E_{col} at low energies within a statistical mechanism. On the other hand, the vibrational effects observed at our lowest energies are inconsistent with a purely statistical mechanism. In such a mechanism, E_{col} and E_{vib} are not expected to be equivalent, because adding E_{col} also increases the available angular momentum. The angular momentum tends to suppress reaction, because the orbiting TS governing decay back to reactants is substantially looser than TS1, thus we might expect that E_{vib} should cause less inhibition than the equivalent amount of E_{col}. To illustrate this effect, Figure 3.7 also shows the effect on forward branching of adding vibrational energy equivalent to 1 or 2 quanta of the bend (large open diamonds). For this calculation, RC was given energy and angular momentum corresponding to the lowest E_{col} point plus the appropriate E_{vib}. Note that the RRKM model predicts less inhibition from E_{vib} than from E_{col}, but strong inhibition nonetheless. In contrast, the experiments show strong and mode-specific vibrational enhancement at low energies. Vibrational effects are discussed further below.

Reaction at High Energies

A new mechanism clearly turns on for E_{col}>~0.4 eV eventually reaching 27% efficiency at high E_{col}. This energy is well past the range where complexes can have any significant effect on the scattering, thus the limiting mechanism must be direct. The v_{axial} distributions support this scenario–as the E_{col} is increased, the distributions become increasingly asymmetric. Note, however, that even at E_{col} = 3.35 eV, where the collision energy dependence has flattened out, the v_{axial} distributions are far from the stripping limit, with a substantial backward-scattered component. Within the osculating complex

model, this backward component is attributed to collisions where the complex rotated ~180° before decaying to products. Clearly, in the high energy limit, the complex lifetimes are too short to allow significant rotation (Figure 3.7); therefore, we need to reinterpret the v_{axial} distributions. In the limit of negligible complex rotation, the forward-scattered component corresponds to large impact parameter collisions, wherein NO_2^+ transfers O, and the nascent NO^+ continues forward. (The same is true for the backward-scattered component of the O^+ transfer channel.) This mechanism is essentially stripping, but there is clearly considerably more translational-to-internal energy conversion than in the spectator stripping limit. If impact parameter is the primary determinant of scattering angle, then the backward-scattered NO^+ (or forward-scattered $C_2H_2O^+$) corresponds to collisions at small impact parameters, leading to product rebound. Of course, at intermediate energies, the v_{axial} distributions presumably depend on both impact parameter and the effects of (ring) complex rotation.

One question is what sets the limiting high energy reaction efficiency at 27%. At low energies, the O/O^+ transfer reaction path requires a very constrained geometry (TS1) so that two CO bonds can form simultaneously. At high energies, the relatively high reaction efficiency implies that a considerably wider range of reactant geometries is reactive, consistent with the potential surface cuts in Figure 3.6. If we assume that O/O^+ transfer can occur in geometries with only one strongly interacting C-O pair, then 27% efficiency seems reasonable. Note, however, that the strong vibrational enhancements, particularly from the bend, imply that reactivity is controlled by more than just the impact geometry, even at high E_{col}.

Vibrational Effects

This system shows strong, and quite mode-specific enhancements from NO_2^+ vibrational excitation (Figure 3.4). Bending is particularly efficient, with effects approximately linear in bending energy for the (010) and (02^00) states, however, the bend overtone enhancement is roughly halved, if the state with angular momentum (02^20) is selected. Finally, the two stretches give even smaller enhancements, despite these being the highest energy modes. One point to note is that the (100) mode is in Fermi resonance with the (02^00) mode. Grant[17] have shown that the mixing from the Fermi resonance is at the ~10% level, i.e., the mode we label (100) has ~90% symmetric stretch character, and ~10% bend overtone character. Conversely, the mode we label (02^00) is ~90% bend overtone and ~10% symmetric stretch. Presumably, if it were possible to prepare the unmixed bend overtone and symmetric stretch states, the already large difference in vibrational effect would be somewhat larger.

As discussed above, the low E_{col} reactivity spike is attributed to trapping into the complex RC, thereby increasing collision time and the chance that the system can find the low energy pathway through TS1. It is conceivable, albeit unlikely, that addition of NO_2^+ vibrational excitation somehow enhances trapping into RC, and thereby enhances the complex-mediated mechanism. As shown in Figure 3.7, however, the suppressing effect of E_{vib} on forward branching (and lifetime) is so large as to cancel any hypothetical enhancement of complex formation. Instead, we propose that NO_2^+ vibration has its effect at TS1, even though TS1 comes after RC on the reaction coordinate. It is interesting to compare the period of the different vibrations with the collision time scale.

The classical vibrational periods associated with the fundamentals of the different modes range from 54 fs for the bend (010), to ~14 fs for the asymmetric stretch (001). The collision time scale is somewhat arbitrary, however, at low E_{col} the relevant scale is the RC lifetime (Figure 3.7). (The ring complex is irrelevant here because it comes after the rate-limiting point on the reaction coordinate, and thus can have no effect on reactivity.) Over the E_{col} range of the reactivity spike, the RC lifetime is at least an order of magnitude longer than any of the vibrational periods. The proposed mechanism, therefore, implies that the initial NO_2^+ vibrational state must remain largely uncoupled to other modes of RC for >10 periods, so that it can influence the breakup of the complex, increasing the branching through TS1 to products. If reactant vibration did couple in RC, the additional energy in the active modes of the complex would strongly inhibit reaction as shown in Figure 3.7.

Presumably the observed pattern of mode effects indicates that particular molecular motions help drive the system toward the TS1 geometry, and thus shift the RC decay branching toward products. The large bending enhancement is reasonable because the NO_2 moiety in TS1 is strongly bent. This scenario also accounts for the relatively weak effects of the symmetric and asymmetric stretches, because TS1 is symmetric with NO bond lengths similar to those in NO_2^+. The additional energy in either stretch mode would strongly inhibit reaction if randomized in the complex; therefore the observed weak enhancements imply that the stretch modes also remain mostly uncoupled in RC, and exert some control over the decay branching, possibly by weakening the geometric constraint to passing through TS1.

The idea that reactant vibrational excitation can survive many vibrational periods in a weakly bound reactant-like complex, then influence the branching during complex decay, is an important result of mode-selective studies. Such behavior has been observed in other systems with weakly bound reactant-like complexes, including some with considerably stronger, and longer-lived complexes than RC (e.g., $C_6H_5OH^+ + ND_3$, with $E_{binding}$ ~1.2 eV and RRKM $\tau_{complex}$ ~1 ns).[18]

At high E_{col}, both reaction efficiency and stripping-like dynamics indicate that reaction can occur in asymmetric geometries where only one NO bond is strongly interacting with the C_2H_2 reactant. One might expect, therefore, that the NO_2^+ bend angle should be less important. Furthermore, because reaction requires ON–O bond scission, one might expect enhancement of a stripping-like mechanism from stretching, particularly the asymmetric stretch (001) which is clearly is coupled to the reaction coordinate, and the highest energy mode. As shown in Figure 3.4, however, the whole pattern of mode effects is qualitatively similar over the entire range of E_{col}, despite the changes in available energy, reaction mechanism, and collision time. It would seem, therefore, that neither vibrationally driven distortion toward the TS1 geometry, nor energy in vibrational motion can directly account for the large and mode-specific vibrational enhancements observed. The suggestion is that vibration, particularly the bend, has some other, indirect mechanism for influencing the dynamics.

The fact that NO_2^+ is linear, but NO_2 is bent at 135°, suggests that NO_2^+ bending excitation might facilitate temporary intrareactant charge transfer during the collision, by lowering the energy difference between the $NO_2^+ + C_2H_2$ and $NO_2 + C_2H_2^+$ states. To the

extent that charge transfer occurs during collisions, it should enhance reactivity, because it converts the system from one consisting of two closed-shell reactants ($NO_2^+ + C_2H_2$) to one with both reactants open shell ($NO_2 + C_2H_2^+$). A similar mechanism was noted in trajectory calculations on the NO_2^+ + Kr system, and found to have a dramatic effect on CID consistent with experiment.[2] If the $Kr^+ + NO_2$ charge state is accessed during a trajectory, the strong Kr^+ - ONO interaction results in temporary Kr-O bond formation, leading to efficient translational-to-vibrational energy transfer, and ultimately to dissociation. In the case of NO_2^+ + Kr, the $NO_2 + Kr^+$ state lies 4.41 eV above reactants (at infinite separation), such that significant interreactant charge transfer occurs only if NO_2^+ becomes strongly distorted along the bending, and to a lesser extent, symmetric stretching coordinates during collision. This requirement for distortion leads to a substantial enhancement from both bending and symmetric stretching excitation, in both experiment and trajectory calculations.[2] (The (001) state was not studied in that system.)

In the present system, O-abstraction in the $C_2H_2^+ + NO_2$ charge state, with or without subsequent charge transfer between the products, could efficiently generate both sets of observed products. Note, however, that the $NO_2 + C_2H_2^+$ charge state lies only 1.8 eV above reactants at infinite separation. Therefore, we might expect that substantial charge transfer (i.e., delocalization) should occur in most collisions, regardless of whether the NO_2^+ distorts strongly or not. Indeed, in complexes like RC, the charge is distributed ~65:35 between the NO_2 and C_2H_2 moieties, reflected in the fact that the NO_2 bend angle (155°) is intermediate between that in NO_2^+ (linear) and NO_2. It is unclear, therefore, whether a vibrationally-induced charge transfer mechanism might still explain the strong

effects of vibration in this system. In addition, such a mechanism does not obviously explain why the (02^20) state is so much less reactive than the (02^00) state, or why the symmetric stretch has so little effect, compared to the effect it has on CID in Kr collisions. A detailed trajectory study, investigating the origin of the strong high E_{col} mode effects, is underway.

Of particular interest is the factor of ~2 suppressing effect of the angular momentum associated with the (02^20) state. As noted in the introduction, there have been only two studies of the effects of bending angular momentum on reactions,[2,5] and the effects were small-to-negligible, as might be expected from the fact that both the angular momentum and associated energy differences were trivial compared to the angular momentum and energy of collisions. The origin of the large difference in reactivity between the (02^00) and (02^20) states is not obvious, but it is useful to consider the nature of the classical vibrational motion. To give a somewhat more realistic (but still classical) picture of the motion, we calculated trajectories of the NO_2^+ vibrational motion in different quasiclassical initial states, using force constants evaluated at the PBE1PBE/6-311G** level of theory. The analysis of collision trajectories will be presented in a future publication. The NO_2^+ zero point motion explores ONO angles between 160° and -160°; however, the reactant is most probably found in near-linear geometry around 175°. In the (02^00) state, the angular range explored increases to ±148°, with the reactant most probably found in the rather broad range between 155° and 165°. Classically, the (02^20) state rotates at the vibrational frequency at fix bend angle; however, when zero-point

motion is included, the quasiclassical motion explores an angular range between 150° and 170°, with most probable angle around 160° and no probability for being linear.

What is different about the (02^20) state, therefore, is that the NO_2^+ never bends to small ONO angles, and that its plane is rotating rapidly (τ_{bend} ~54 fsec). Either factor could potentially reduce reactivity. For example, if distorting to a small ONO angle is important in driving reaction (perhaps by charge transfer), then the considerably smaller ONO angle reached in the (02^00) state would tend to make it more reactive. Note that the ONO angle in the (02^20) state is similar to the minimum ONO angle reached in the (010) state. If the ONO angle at some critical time in the collision is the critical factor, then we might expect that the (02^20) state should be somewhat more reactive than the (010) state, because it spends all its time at the minimum ONO angle, whereas the (010) state reaches its minimum angle for only a fraction of each vibrational period. This expectation is correct, as shown in Figure 3.4. A "maximum distortion" mechanism seems plausible at low E_{col}. At high E_{col}, however, where the vibrationally-driven distortions are presumably small compared to those driven by the collision dynamics, and where the system reacts with reasonably high efficiency even for the ground state, it is not obvious why the (02^20) state continues to be substantially less reactive than the (02^00) state.

The other possibility is that the enhancement from bending is partially canceled by rapid rotation of the NO_2^+. As shown in Figure 3.6, the energy of the rate limiting TS1 is greatly increased if ONO is not oriented such that the two O atoms bend toward the C_2H_2 reactant. One might, therefore, imagine that rapid rotation of the ONO bend plane in the (02^20) state makes it difficult for the system to find the minimum energy path. Such an

argument seems reasonable at low energies, where the collision time is long compared to τ_{bend}. In particular it seems likely that in a complex like RC, where the reactant approach is one of the low frequency modes of the complex, that rotation of ONO on a faster time scale would make finding TS1 unlikely. At high E_{col}, where the collision time becomes short and the reactivity less dependent on orientation (reaction efficiency >25%), it is harder to see why ONO rotation should continue to have a large suppressing effect.

References

1. R. J. Green, H.-T. Kim, J. Qian, and S. L. Anderson, J. Chem. Phys. 113, 4158 (2000).

2. J. Liu, B. W. Uselman, J. M. Boyle, and S. L. Anderson, J. Chem. Phys. 125, 133115 (2006).

3. J. Liu, B. Van Devener, and S. L. Anderson, J. Chem. Phys. 123,204313/1 (2005); J. Liu, K. Song, W. L. Hase, and S. L. Anderson, J.Phys. Chem. A 109, 11376 (2005); J. Liu, B. Van Devener, and S. L.Anderson, J. Chem. Phys. 121, 11746 (2004); J. Liu, B. Uselman, B. VanDevener, and S. L. Anderson, J. Phys. Chem. A 108, 9945 (2004); J. Liu,K. Song, W. L. Hase, and S. L. Anderson, J. Am. Chem. Soc. 126, 8602 (2004); J. Liu and S. L. Anderson, J. Chem. Phys. 120, 8528 (2004); J. Liu, K. Song, W. L. Hase, and S. L. Anderson, J. Chem. Phys. 119, 3040 (2003).

4. B. J. Orr, Chem. Phys. 190, 261 (1995); A. E. Depristo and L. C. Geiger, Surf. Sci. 176, 425 (1986); D. C. Clary, J. Chem. Phys. 75, 209 (1981).

5. C. Kreher, R. Theinl, and K.-H. Gericke, J. Chem. Phys. 104, 4481 (1996).

6. B. Uselman, J. Liu, J. Boyle, and S. Anderson, J. Phys. Chem. 110, 1278 (2006).

7. Y.-H. Chiu, H. Fu, J.-T. Huang, and S. L. Anderson, J. Chem. Phys. 102, 1199 (1995).

8. J. Liu, H.-T. Kim, and S. L. Anderson, J. Chem. Phys. 114, 9797 (2001).

9. M. J. Frisch, G. W. Trucks, H. B. Schlegel, G. E. Scuseria, M. A. Robb, J. R. Cheeseman, J. J. A. Montgomery, T. Vreven, K. N. Kudin, J. C. Burant, J. M. Millam, S. S. Iyengar, J. Tomasi, V. Barone, B. Mennucci, M. Cossi, G. Scalmani, N. Rega, G. A. Petersson, H. Nakatsuji, M. Hada, M. Ehara, K. Toyota, R. Fukuda, J. Hasegawa, M. Ishida, T. Nakajima, Y. Honda, O. Kitao, H. Nakai, M. Klene, X. Li, J. E. Knox, H. P. Hratchian, J. B. Cross, C. Adamo, J. Jaramillo, R. Gomperts, R. E. Stratmann, O. Yazyev, A. J. Austin, R. Cammi, C. Pomelli, J. W. Ochterski, P. Y. Ayala, K. Morokuma, G. A. Voth, P. Salvador, J. J. Dannenberg, V. G. Zakrzewski, S. Dapprich, A. D. Daniels, M. C. Strain, O. Farkas, D. K. Malick, A. D. Rabuck, K. Raghavachari, J. B. Foresman, J. V. Ortiz, Q. Cui, A. G. Baboul, S. Clifford, J. Cioslowski, B. B. Stefanov, G. Liu, A. Liashenko, P. Piskorz, I. Komaromi, R. L. Martin, D. J. Fox, T. Keith, M. A. Al-Laham, C. Y. Peng, A. Nanayakkara, M. Challacombe, P. M. W. Gill, B. Johnson, W. Chen, M. W. Wong, C. Gonzalez, and J. A. Pople, GAUSSIAN 03 (Gaussian, Inc., Pittsburgh PA, 2003).

10. L. Zhu and W. L. Hase, QCPE 644, a general RRKM program (Chemistry Department, University of Indiana, Bloomington, 1993).

11. S. G. Lias, in *NIST Standard Reference Database Number 69*, edited by P. J. Linstrom and W. G. Mallard (National Institute of Standards and Tech- nology, Gaithersburg, MD, 2003); http://webbook.nist.gov.

12. A. Ding, A. Henglein, and K. Lacmann, Z. Naturforsch. A 23, 779 (1968).

13. G. A. Fisk, J. D. McDonald, and D. R. Herschbach, Discuss. Faraday Soc. 44, 228 (1967).

14. F. Bernardi, F. Cacace, G. de Petris, F. Pepi, I. Rossi, and A. Troiani, Chem.-Eur. J. 6, 537 (2000).

15. L. Zhu and W. L. Hase, Quant. Chem. Prog. Exchange, QCPE 644, a general RRKM program (Quantum Chemistry Program Exchange, Bloomington, IN, 1993).

16. K. P. Huber and G. Herzberg, *Molecular Spectra and Molecular Structure IV. Constants of Diatomic Molecules* (Van Nostrand Reinhold, New York, 1979).

17. E. R. Grant, J. Mol. Spectrosc. 175, 203 (1996).

18. S. L. Anderson, J. Chem. Phys. 112, 5717 (2000).

19. S. G. Lias, J. E. Bartmess, J. F. Liebman, J. L. Holmes, R. D. Levin, and W. G. Mallard, in *NIST Chemistry WebBook, NIST Standard Reference Database Number 69*, edited by W. G. Mallard and P. J. Linstrom (National Institute of Standards and Technology, Gaithersburg, MD, 2000); http://webbook.nist.gov.

Table 3.1.

Experimental and *ab initio* energies (eV) relative to reactants ($NO_2^+ + C_2H_2$)

	B3LYP/6-311++G**[a]	MP2/ 6-311++G**	G3 (0 K)	Experimental[b]
$NO^+ + CH_2CO$	-2.54	-2.35	-2.58	-2.98
$NO + CH_2CO^+$	-2.68	-1.60	-2.30	-2.62
$NO^+ + HCCOH$	-0.93		-1.09	-1.66
$NO + HCCOH^+$	-0.88		-0.38	
Reactant complex	-0.54		-0.44	
Ring complex	-2.97		-2.90	
Product complex 1	-3.74			
Product complex 2	-2.16			
TS1	-0.36			
TS2	-1.01			
TS3	-1.40			

[a]Including zero-point energy calculated at B3LYP/6-311++G** and scaled by 0.9804.

[b]NIST Chemistry Web Book (Ref. 19)

Table 3.2.

Fit results for NO^+ v_{axial} distributions.

E_{col} (eV)	$< E_{avail} >$ [a] (eV)	$<E_{recoil}>$ (eV)	$<E_{recoil}>/<E_{avail}>$ (%)	$\tau_{collision}$ (ps)	τ_{flyby} [b] (ps)
0.411	2.98	0.36	12	1.3	0.23
1.07	3.64	0.47	12	0.21	0.14
2.19	4.76	0.57	12	0.17	0.10
3.33	5.90	1.10	19	0.10	0.08

[a] < > =mean value

[b] $\tau_{fly\text{-}by}$ defined as time for reactants to travel a relative distance of 5Å.

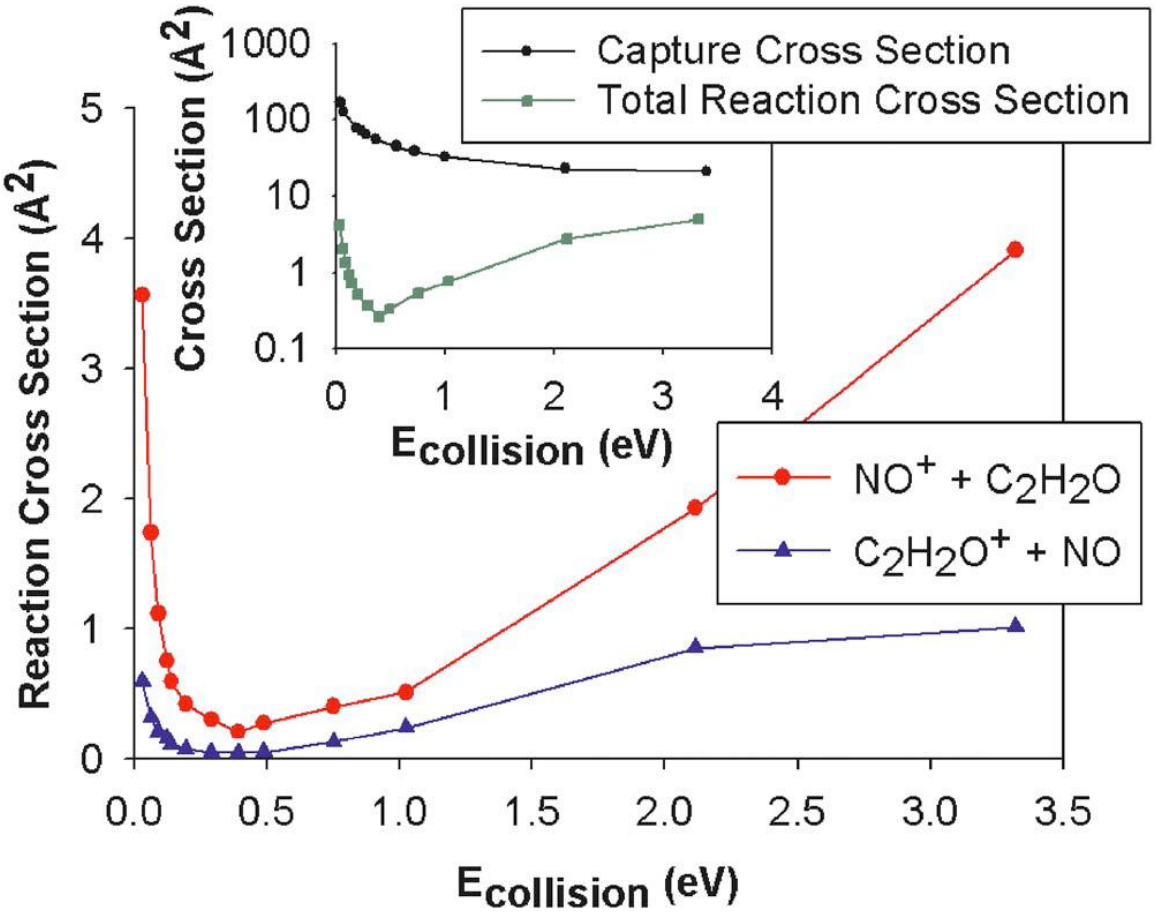

Figure 3.1. Ground state reaction cross section vs. collision energy. Inset: total cross section and the estimated collision cross section.

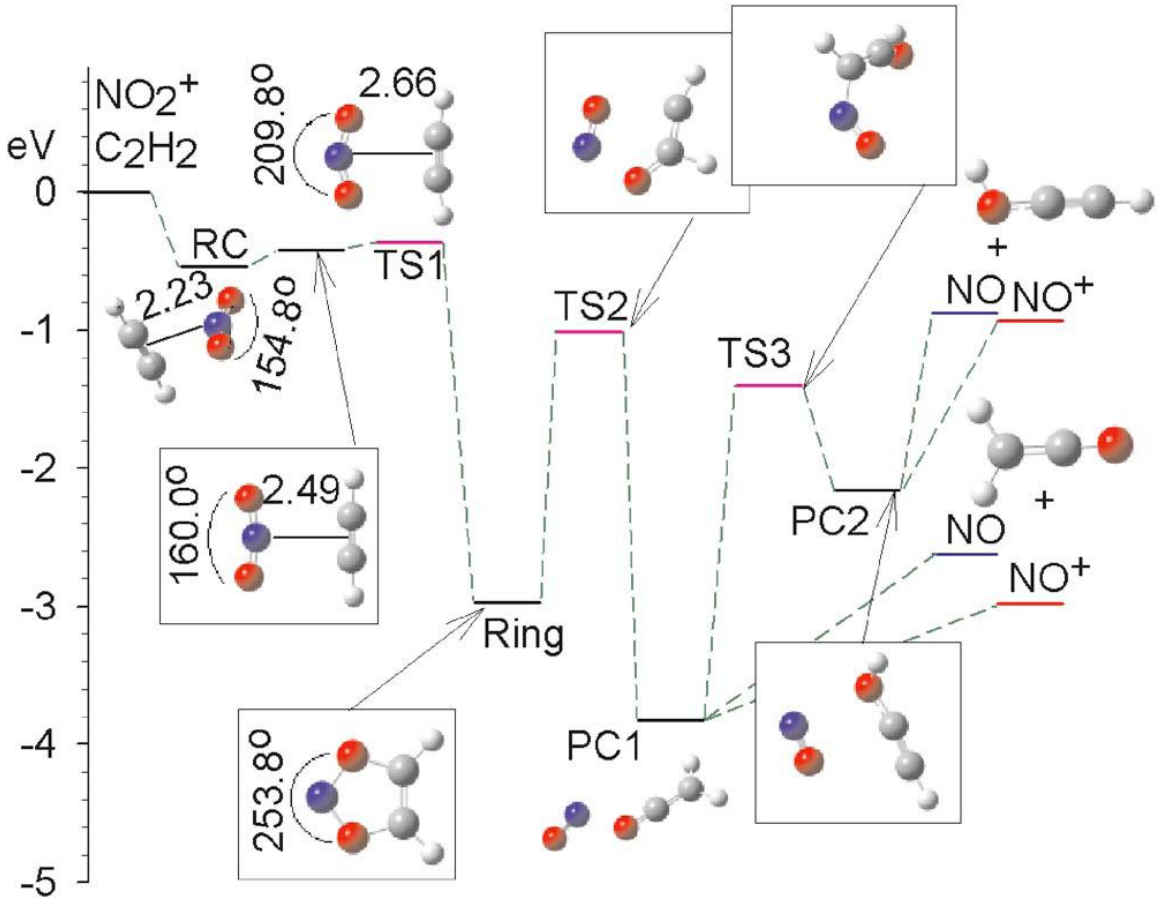

Figure 3.2. Reaction coordinate for $NO_2^+ + C_2H_2$.

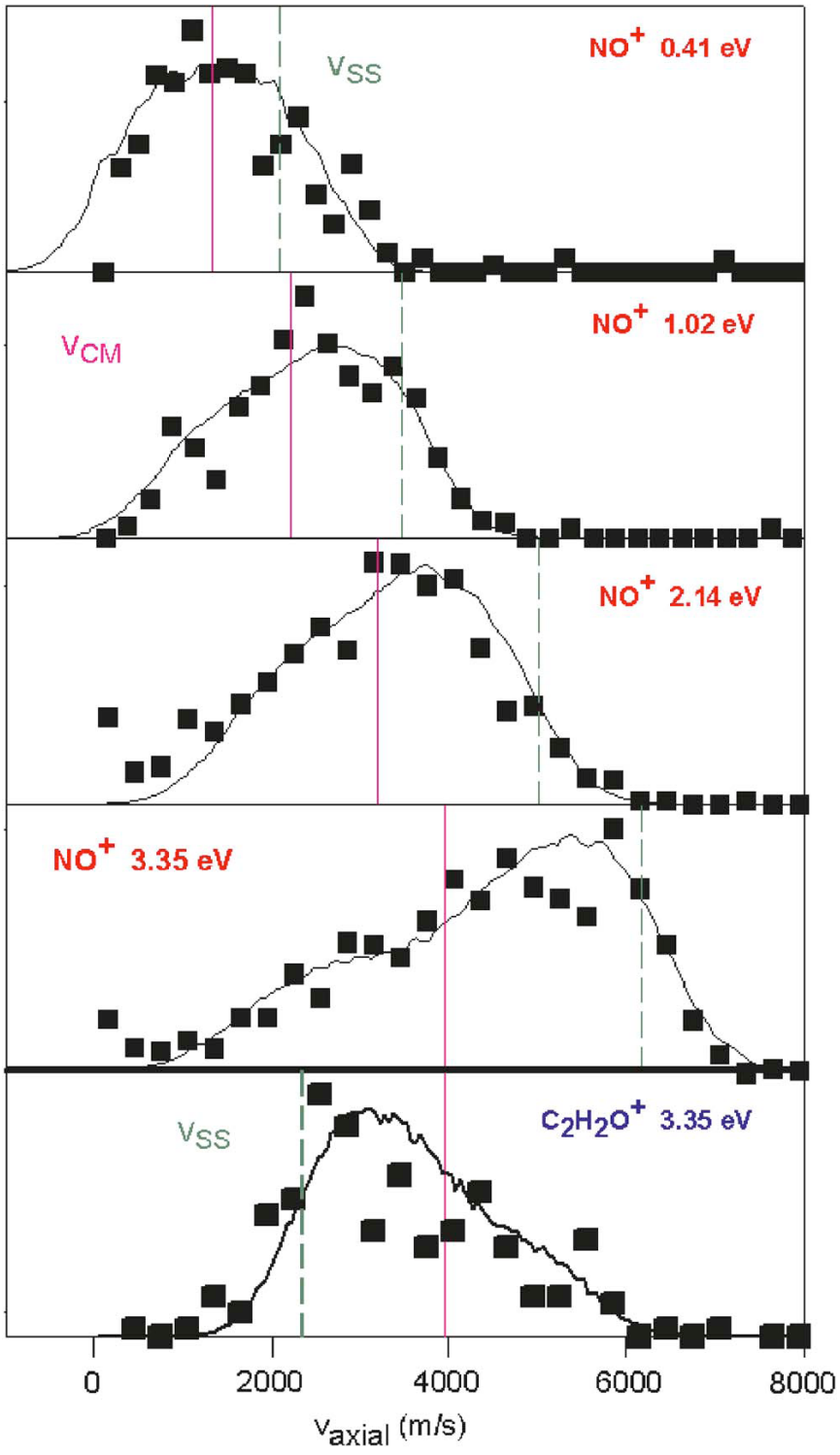

Figure 3.3. Axial recoil velocity distributions for the NO^+ channel (top four frames) and $C_2H_2O^+$ channel (bottom frame). Points are experimental. Solid curves are simulations. Solid vertical line is $\langle V_{c.m.} \rangle$. Dashed vertical line is $\langle V_{SS} \rangle$.

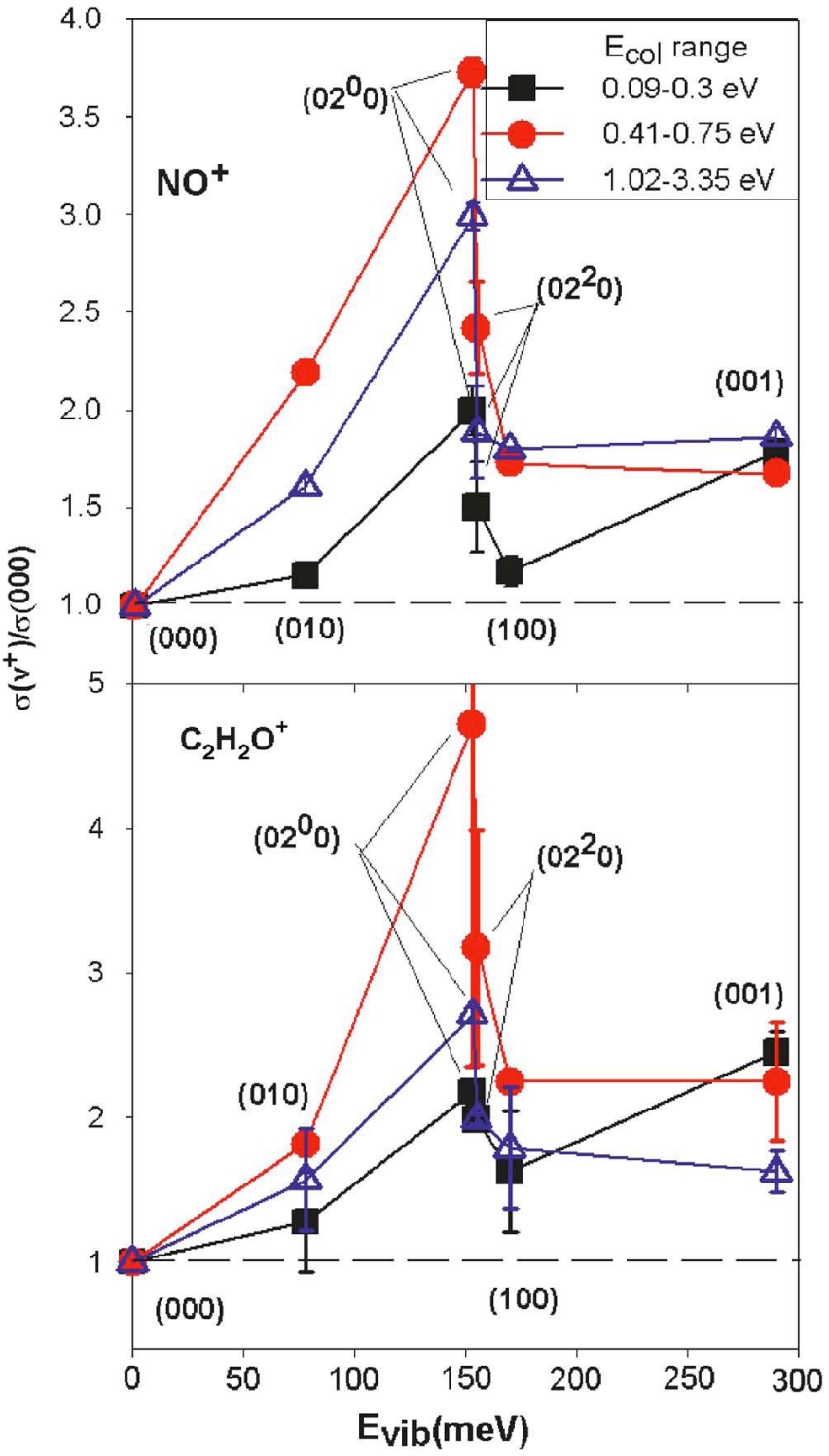

Figure 3.4. Vibrational enhancement factors vs vibrational energy, and averaging collision energy points within the indicated ranges.

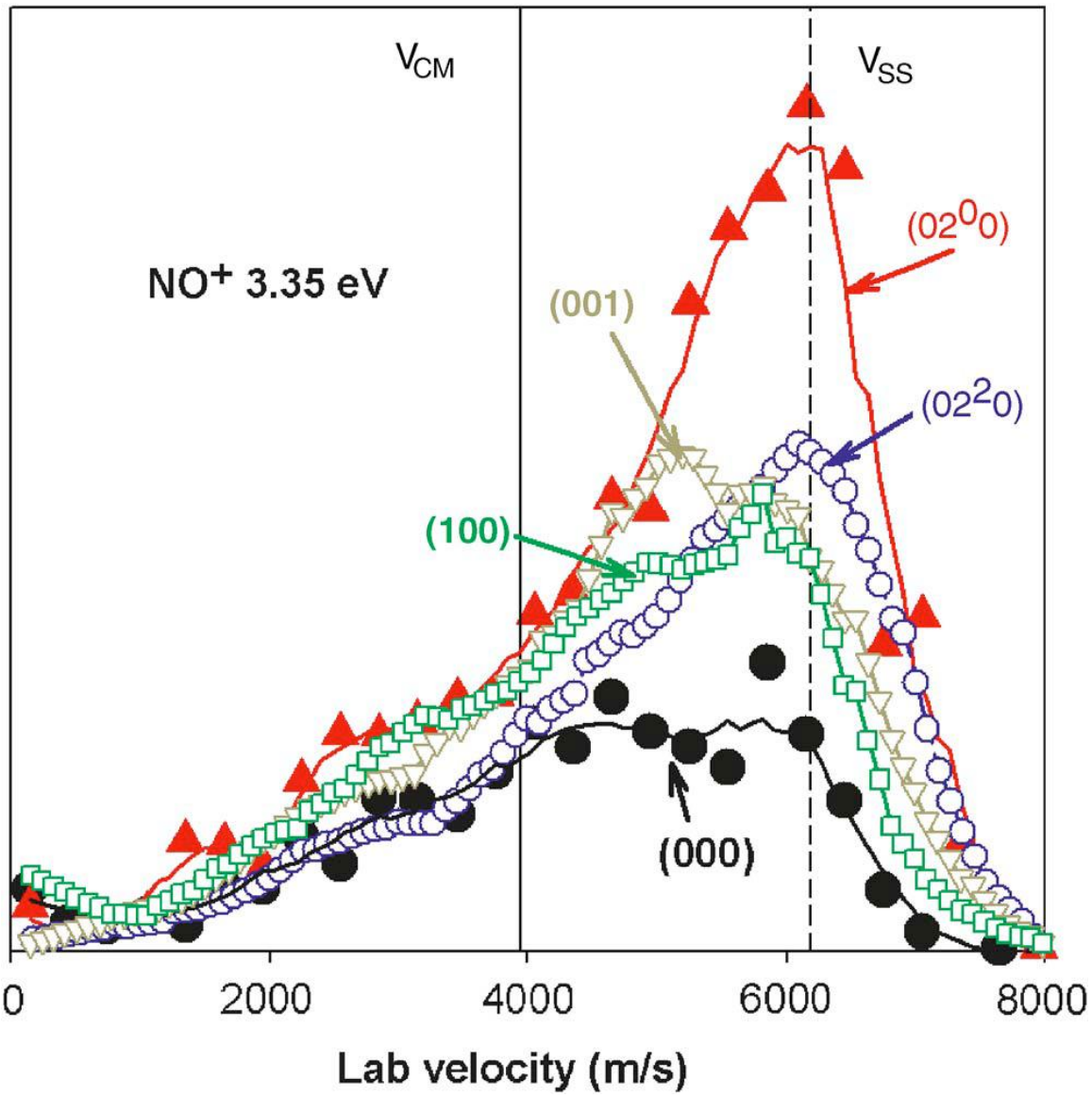

Figure 3.5. Axial recoil velocity distributions for the (000), (100), (001), (02^00), and (02^20) states at 3.35 eV collision energy. Solid vertical line: $<V_{c.m.}>$. Dashed vertical line: $<V_{SS}>$.

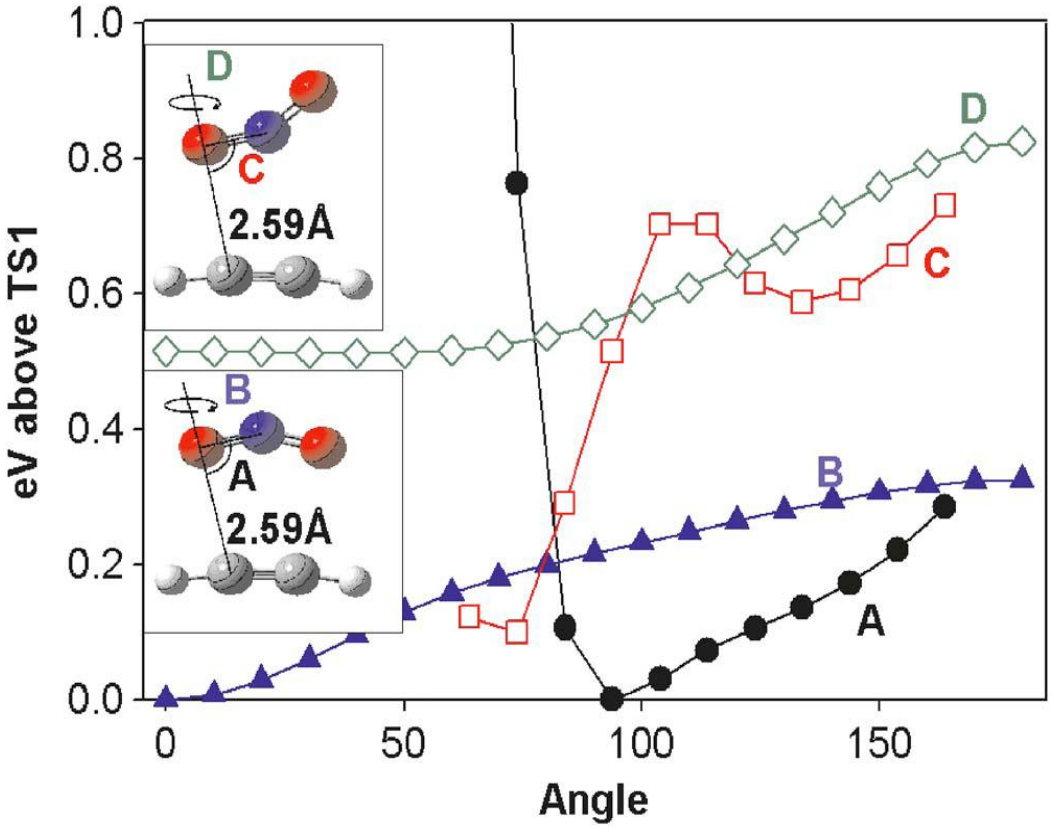

Figure 3.6. Cuts through the potential energy surface near TS1 for the indicated distortions of the TS1 structure. Energies are relative to TS1.

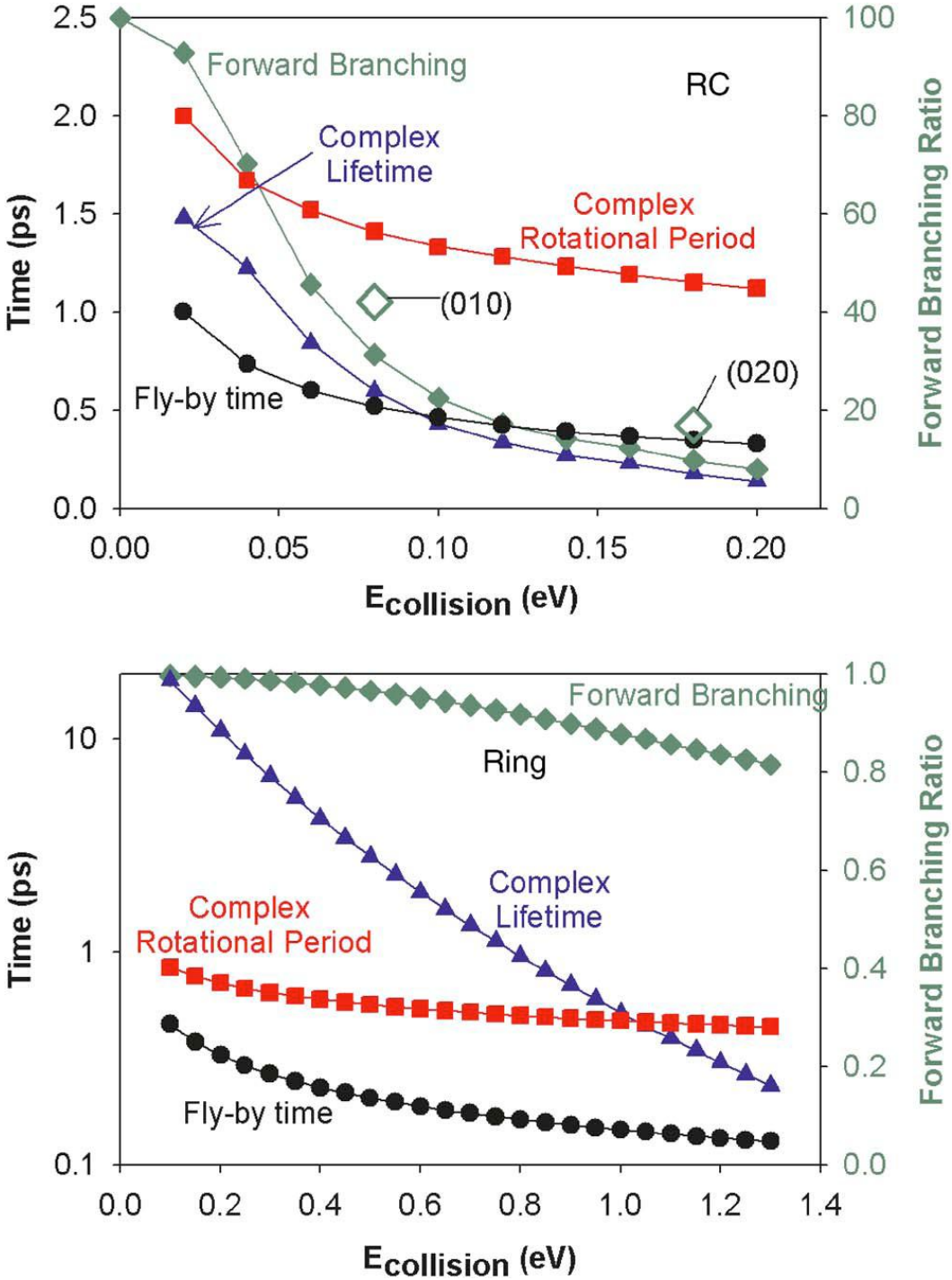

Figure 3.7. Left hand scales: RRKM lifetime and rotational period vs. collision energy for the RC (top) and ring (bottom) complexes, compared to Fly-by time (see text). Right hand scale: forward branching ratios.

CHAPTER 4

EFFECTS OF BENDING AND BENDING ANGULAR MOMENTUM ON REACTION OF NO_2^+ WITH C_2H_2: A QUASI-CLASSICAL TRAJECTORY STUDY

Overview

A large set of quasi-classical trajectories were calculated at the PBE1PBE/6-311G** level of theory, in an attempt to understand the mechanistic origins of the large, mode-specific enhancement of the O-transfer reaction by NO_2^+ bending vibration, and the surprisingly large suppressing effect of bending angular momentum. The trajectories reproduce the magnitude of the absolute reaction cross section, and also get the dependence of reactivity on NO_2^+ vibrational state, and the vibrational state dependent scattering behavior qualitatively correct. Analysis of the trajectories shows that the bending effect is not simply a consequence of enhanced reactivity in bent geometries, but rather, that excitation of bending motion allows reaction in a wider range of orientation angles, even if the NO_2^+ is not bent at the onset of the collisional interaction. There is a strong interplay between NO_2^+ bending and transient charge transfer during the collisions. Such charge transfer enhances reactivity, but only if the reactants are oriented correctly.

Introduction

Chapter 3 reports an experimental study of vibrational mode and collision energy effects on the dynamics of oxygen transfer in the $NO_2^+ + C_2H_2$ reaction.[1] The dynamics of this apparently simple reaction proved to be surprisingly complex, with several features that could not be rationalized on the basis of the experimental results, including RRKM analysis of an ab initio reaction coordinate. Here, we report a quasi-classical trajectory (QCT) study of $NO_2^+ + C_2H_2$ collisions, aimed at understanding the following key features of this system at high collision energies: (1) The severe bottleneck to this

atom-transfer reaction; (2) The strong vibrational enhancement, particularly from NO_2^+ bending; (3) The strong suppressing effect of bending angular momentum; (4) The mechanism by which bend excitation influences the product recoil dynamics. Before describing the QCT methodology and results, we first outline the key features of the reaction coordinate and experimental results.

Summary of the Experimental Results and Properties of the System

An ab initio reaction coordinate, calculated at the B3LYP/6-311++G** level of theory, is shown in Figure 4.1. The two product channels, $NO^+ + H_2CCO$ and $NO + H_2CCO^+$, represent two different, nearly isoenergetic, electronic states of $(NO + ketene)^+$. The two channels show virtually identical dynamics, including dependence on collision energy and reactant vibrational excitation, as well as product recoil behavior. The reason is clear in Figure 4.1. The reaction coordinate bifurcates into the two product channels quite late in the collision, as the products separate, and the charge has to localize on one or the other. Mulliken charge calculations indicate that the charge is delocalized in all of the complexes and TSs of interest during the collision. Properties such as vibrational state or collision energy dependences can only depend on dynamics leading up to the rate-limiting step on the reaction coordinate, which in this case occurs early in the collisions (see below). Recoil behavior, of course, will depend on dynamics throughout the course of the collisions; however, the gross features of the scattering (stripping vs rebound dynamics, energy disposal) are apparently only weakly dependent on dynamics occurring during product separation. For the purposes of this report we, therefore, focus on the factors controlling total reactivity, i.e., on dynamics leading up to the rate-limiting

step. Early time dynamics are ideal for quasi-classical trajectories, because error tends to be cumulative during a trajectory (see below) and because the method is not amenable to studying the process of branching into two product states.

The experimental reactivity results are summarized in Figure 4.2a, which gives the collision energy ("E_{col}", center-of-mass frame) dependence of the total cross section (σ_{Total}), and Figure 4.2b, which plots the effect on reactivity of exciting the various NO_2^+ vibrational states, as a function of the vibrational state energy (E_{vib}) for several ranges of E_{col}. To show the vibrational effects more clearly, Figure 4.2b gives ratios of the cross section for reaction of vibrationally excited NO_2^+ to the ground state cross section: $\sigma_{Total}(n_1n_2n_3)/\sigma_{Total}(000)$. The notation ($n_1n_2n_3$) gives the number of quanta excited in the symmetric stretch, bend, and asymmetric stretch modes, respectively. The x-axis of Figure 4.2b gives the vibrational state energies.

Note (Figure 4.2a) that the cross section has strong bimodal dependence on E_{col}, and is substantially smaller than the collision cross section, which is taken as the larger of the ion-induced dipole capture cross section and hard sphere cross sections. Clearly there is a bottleneck inhibiting this barrierless, exoergic reaction, and RRKM analysis of the various complexes and transition states on the reaction coordinate suggests that the bottleneck (at least for low E_{col}) is TS1.[1] The bottleneck was attributed to TS1 being tight, i.e., the energy increases rapidly for distortion away from the C_{2v} symmetry TS1 geometry. The spike in reactivity at low E_{col} was attributed to mediation by the weakly bound complex "RC", allowing the system time to find its way to the TS1 geometry. At high E_{col}, the cross section increases because there is enough energy to react in non-

optimal geometries, although σ_{Total} remains well below $\sigma_{collision}$. At E_{col} near 0.5 eV, the RC lifetime is too short to mediate reaction, but the available energy is still too low to significantly loosen the geometric requirement for reaction, thus reaction occurs only in the small fraction (<1%) of collisions that occur near the ideal TS1 geometry.

All modes of NO_2^+ vibration enhance reaction (Figure 4.2b) at all collision energies, even at low E_{col} where collision energy inhibits reaction. At high E_{col}, where both E_{col} and E_{vib} enhance reaction, asymmetric stretch (001) excitation has an enhancing effect roughly 3 times larger than the effect of adding an equivalent amount of E_{col} (0.29 eV). Enhancement from this mode is not surprising–asymmetric ON-O stretching should be

the mode most strongly coupled to the reaction coordinate for oxygen transfer. The other modes give even larger enhancements, however. Symmetric stretch (100) excitation is about five times more effective than the equivalent amount (0.17 eV) of E_{col}, and bending excitation is up to 16 more efficient. The bend enhancements are, however, strongly dependent on whether there is angular momentum associated with the bending motion. Compare the effects of the two bend overtone states: (02^00) with E_{vib} = 153 meV, and (02^20) with E_{vib} = 155 meV, where the 0 or 2 superscript refers to the angular momentum associated with bending. The (02^00) state gives rise to approximately twice the enhancement seen for the (010) state, as might be expected, however, (02^20) excitation is considerably less effective (but still more effective than either stretch vibration). The difference in both energy and angular momentum between the (02^00) and (02^20) states is negligible compared to the energy and angular momentum of the collisions; thus the reactivity difference must reflect a difference in the nature of the

reactant motion. This is, by far, the largest effect of bending angular momentum on reactivity ever observed,[2-6] and elucidating the mechanism is one of the main goal of the QCT study.

Another unusual feature of this reaction is that the pattern of vibrational mode effects is constant over a wide range of E_{col}, even though the reaction mechanism clearly changes from complex-mediated (E_{col} < ~0.4 eV) to direct (E_{col} > ~1 eV). Over the same E_{col} range the timescale of the collisions decreases from being many times the vibrational timescale, to being comparable. The magnitude of the vibrational effects remains large, even at high E_{col} where the E_{vib} is only a few percent of the total reactant energy.

Finally, the experimental study found that NO_2^+ vibrational excitation, particular bending, results in substantial changes in the product recoil dynamics at high collision energies, leading to a more forward-scattered velocity distribution than for the ground state. In past studies of vibrational effects on product recoil in ion reactions, we have seen insignificant effects on product recoil, even for reactions where vibration strongly affects reactivity.[5,7-17] Lack of vibrational effects on recoil is not surprising – energy is likely to be scrambled in reactive collisions, and reactant E_{vib} is typically only a small fraction of the total energy available to products, particularly at high E_{col}. As might be expected, the exception has been for endoergic reactions near threshold, where E_{vib} ***is*** a significant fraction of the energy available to products.[14,18] The present reaction is more than 2.5 eV exoergic, such that the bending vibrations contribute <3.5% of the available energy at high E_{col}.

Computational Methodology

Quasi-classical, direct dynamics trajectories were calculated for a collision energy of 2 eV, and for NO_2^+ in its ground, (02^00), and (02^20) states. The QCT method is not suitable for low energy collisions, both because the trajectory time scale is unfeasibly long, and because errors arising from treating vibration classically become severe (see below). The method used to calculate quasi-classical initial conditions for states including vibrational angular momentum and ZPE was discussed in detail by Lourderaj et al.[19] The quasi-classical initial vibrational state is simulated by giving the reactant atoms displacements from equilibrium and kinetic energies appropriate to the desired initial rovibrational state, with random phases for the different modes, and random initial orientations. Because the experiments generated NO_2^+ by REMPI of a supersonic molecular beam, a 50 K Boltzmann distribution was sampled to select the NO_2^+ initial rotational state. The NO_2^+ vibrational state included the desired mode-selective vibrational excitation plus zero-point energy (ZPE) in all modes. The C_2H_2 in the experiments was at room temperature, thus the trajectory initial state included ZPE for all vibrational modes, and a rotational state sampled from a 300 K Boltzmann distribution. The VENUS program of Hase and co-workers[20] was used to calculate initial atomic positions and velocities, and trajectories were integrated using the updating Hessian method of Schlegel and co-workers,[21] implemented in GAUSSIAN03.[22]

In order to get statistics good enough to examine vibrational effects for a reaction with small cross section, thousands of trajectories are required, and we try to use theoretical methods that require less than ~12 CPU hours/trajectory. Candidate methods

and basis sets were benchmarked against single point calculations at the QCISD(T)/cc-pVTZ level of theory. Following the approach we have used successfully for several other ion-molecule systems,[5,23-25] we initially tested how well each method reproduced benchmark energies for approach of NO_2^+ to C_2H_2, and for important stationary points on the reaction coordinate, leading up to the rate-limiting point (TS1). This process lead to selection of the MP2/6-31G* method for the initial set of trajectories; however, the calculated reaction cross sections were much smaller than the experimental cross sections and failed to reproduce the observed vibrational effects. The reason is that while MP2/6-31G* reproduces benchmark energies for reactant approach in several symmetric geometries, and also the complex and TS1 energies, it overestimates energies of non-symmetric points near TS1, i.e., the critical TS is too tight at the MP2/6-31G* level. Conversely, B3LYP/6-31G* results in an overly loose TS1, such that the calculated reaction efficiency is nearly unity independent of vibrational state.

Clearly it is critical to identify a level of theory that reasonably represents the regions of the potential surface that the trajectories actually explore as they approach the rate-limiting step in the reaction. For this purpose, we took several reactive and non-reactive trajectories calculated at the MP2/6-31G* and B3LYP/6-31G* levels, and selected six geometries corresponding to points where bonds appeared to be breaking or forming in various reactant orientations. A variety of levels of theory were then compared to QCISD(T)/cc-pVTZ energies at these selected geometries. On the basis of the overall level of agreement and computational speed, we chose the PBE1PBE/6-311G** level of theory for the main set of trajectories. At this level of theory, each trajectory takes ~22

CPU hours on our Athlon 64-based cluster, forcing us to limit the scope of the calculations.

Trajectories were calculated for only one collision energy (2 eV) and for the three reactant states of greatest interest (ground state, ($02^{0}0$), and ($02^{2}0$)). Because the number of trajectories was necessarily limited, we adopted the following strategy in order to minimize the uncertainty in comparing behavior for different NO_2^+ states or impact parameters. For each state, batches of trajectories (typically 300) were calculated for discrete values of the reactant impact parameter (b = 1, 1.5, 2, 2.5Å) rather than randomly sampling the b distribution. Collisions at impact parameters below 1Å were omitted because their weighting in the integral cross section is small, and only 60 trajectories were calculated for each state at b= 2.5Å because no reaction was observed.

In addition, the random number generator seed used in setting up initial conditions for each batch of trajectories was identical. Each trajectory batch, therefore, used the same pseudorandom sequence to sample the reactant parameter space (orientations, rotational energies, rotational and vibrational phases, etc.). The main motivation for this pseudorandom sampling procedure was to avoid a potentially serious problem that arises when reactivity is sharply dependent on one or more reactant parameters. For example, in our previous studies of H_2CO^+ reactions with CD_4 and D_2,[23,24] reactivity was found to be highly sensitive to orientation. As a result, when trajectory batches for different reactant states (for example) were calculated with random sampling of the initial conditions, the slightly different distributions of orientation in different batches resulted in variations in reaction probability that were comparable to the effects of reactant state.

By using the same pseudorandom sequence for each batch, the error from inadequate sampling of reactant parameter space is the same for all batches, and tends to cancel when comparing batches for different states or impact parameters. A secondary benefit is that trajectories for different NO_2^+ states or impact parameters can be compared directly, because corresponding trajectories from different batches have identical initial conditions, apart from the parameter being varied (i.e., the NO_2^+ state or impact parameter).

Trajectory integration was performed with a step-size of 0.25 $amu^{1/2}$bohr (~0.56 fs), and trajectories were terminated either when the distance between the final products exceeded 9.0 Å or after 500 steps. To minimize time spent calculating the reactant approach phase of the trajectories, they were started at an initial interreactant separation of 7Å. At this distance, the long-range ion-induced dipole interaction is not negligible. Using the angle-averaged polarizability of acetylene[26], we can estimate that the potential is ~12 meV at 7 Å. This means that if the trajectories had been started at infinite separation, the collision energy would have been increased by ~12 meV by the 7Å separation. In effect, by starting the trajectories at 7Å with a relative energy of 2 eV, we effectively are simulating collisions at 1.988 eV collision energy. This shift from the 2 eV nominal energy is insignificant compared to the 0.38 eV collision energy spread in the experiments, which results from both the energy distribution of the primary beam (0.15 eV) and Doppler broadening from thermal motion of the acetylene target.[27] Energy conservation was better than 0.01 eV for all trajectories. The analysis below is based on a total ~2900 trajectories, corresponding to ~ 6.8 years of Athlon 64 CPU time.

Because trajectories were calculated at discrete *b* values, the trajectory cross sections were estimated using an extended closed trapezoidal approximation[28] to the usual integral form, where P(*b*) is the fraction of reactive trajectories at each impact parameter, i.e., the opacity function

$$\sigma = 2\pi\int_0^{b_{\max}} P(b)bdb \approx \pi\sum_{b_i=0}^{b_{\max}} [P(b_i)\times b_i + P(b_{i+1})\times b_{i+1}]\times (b_{i+1} - b_i)$$

For trajectory visualization we use the program gOpenMol.[29] Detailed analysis of individual trajectories and statistical analysis of the trajectory ensemble were done with programs written for this purpose,[25] available from the corresponding author upon request.

Potential Problems with QCT

There are several issues with using the QCT method to probe vibrational dynamics in systems like $NO_2^+ + C_2H_2$. One obvious point is that vibration is not quantized, leading to several types of nonphysical behavior. At the start of the trajectories, the vibrational energy is partitioned appropriately to represent the classical analog of the desired initial quantum state. During the time required for reactant approach, the initial energy partitioning can decay via anharmonic coupling of the normal modes, such that the vibrational motion at the moment of collision no longer represents the state of interest. Several factors help minimize this issue for the present system. The collision energy is high, and we start the trajectories with reactant center-of-mass separation of only 7Å, so that only ~100 fs elapse prior to the collision. Because both reactants are small molecules, the number of symmetry-allowed mode combinations capable of coupling to the initial state is limited.

It is easy to check for decay of the initial vibrational state by simply monitoring the vibrational amplitudes of various molecular geometric parameters as the reactants approach each other. For example, perhaps the most likely combination for intermode energy transfer is $(02^{0}0) \leftrightarrow (100)$, because these two states have the same symmetry, and similar frequencies (the quantum states are in Fermi resonance with ~10% mixing of the 0^{th} order stretch and bend overtone levels). If the initial $(02^{0}0)$ excitation decayed during reactant approach, this would be obvious as a decrease in the amplitude of the NO_2^+ bending motion, with corresponding amplitude increase in some other mode, such as the symmetric stretch. As can be seen in the trajectory plots discussed below, the amplitudes are quite constant up to the point where collisional interaction begins to perturb the motion. In fact, we see little change in amplitudes even in non-colliding test trajectories where the total time monitored is five times longer than the typical reactant approach. We conclude that at the "moment of collision" the trajectories still represent the desired states, at least to the extent possible in the quasiclassical framework.

Lack of quantization presumably has a significant effect on how energy is distributed between vibrational modes during and after collisions.[30,31] Here again, the fact that we are interested in high E_{col} helps, in that the available energy is large compared to the vibrational quanta, reducing the error associated with treating the motion classically. More importantly, the observables of greatest interest for our purposes are the effects of NO_2^+ vibration on the cross section, which depend only on dynamics up to the rate-limiting point on the reaction coordinate. The experimental observation of strong, mode-

specific vibrational effects indicates that the rate-limiting point must be early in the collision, before the initial excitation is scrambled. Such systems are ideal for QCT.

Another issue in this system is the fact that two electronic states contribute to the lowest Born-Oppenheimer (BO) surface that the trajectories run on. Figure 4.3 shows the two lowest energy diabatic surfaces for $(NO_2\text{-}C_2H_2)^+$, cut along the NO_2 bend and symmetric stretch coordinates at infinite NO_2 – C_2H_2 separation. The NO_2^+ + C_2H_2 reactant state is the global minimum by 1.8 eV; however, because of the difference in equilibrium geometry between NO_2^+ (linear) and NO_2 (134°), there are regions in configuration space where the NO_2 + $C_2H_2^+$ charge state is lower in energy. As reactants approach, the crossing becomes avoided, and the lowest BO surface smoothly connects regions where the electronic configuration corresponds to NO_2^+ + C_2H_2 and NO_2 + $C_2H_2^+$. As discussed previously, the charge is roughly equally shared between the reactant moieties in geometries like RC, TS1, or the Ring complex.[1]

There are two concerns here. One is that the QCT code used does not allow for non-adiabatic (surface hopping) transitions at surface crossing seams. Surface hopping would be important if the transition between the two charge states during collisions were abrupt, i.e., if the avoided crossing was localized, with small intersurface splitting, and/or if the motion perpendicular to the seam were rapid. There is no reason to expect any of these conditions to hold. The motion perpendicular to the seam is ONO bending, which is a relatively low frequency motion (54 fs). The transition between NO_2^+ + C_2H_2 and $C_2H_2^+$ + NO_2 seems to be smooth, as indicated by the charge on the C_2H_2 moiety during the trajectories (Figure 4.4). It appears that by the time the collisional interaction is strong

enough to distort the system into geometries where $C_2H_2^+ + NO_2$ becomes the dominant configuration, the interaction also has mixed the diabatic states strongly enough to result in gradual transitions.

Another potential problem for systems with avoided crossings is that there might be geometries near the crossing seam where a single reference wave function is inadequate, leading to inaccurate forces in the DFT calculations. We tested for this problem by running single point CASSCF(8,8) calculations for geometries explored by a sample set of trajectories. The coefficient of the Hartree-Fock configuration was greater than 0.95 in all but one geometry, and even there the coefficient was >0.85. Use of a single reference DFT method should not be a serious problem.

Results and Discussion

Before the calculations are presented, it is useful to review the nature and time scales of the motions we are simulating. The time scale of the collisions is somewhat arbitrary, but three numbers are relevant. The time between trajectory start and the onset of strong intermolecular interaction is 80 – 100 fs, depending on reactant orientation. The time during which the interaction is strong can be hundreds of femtoseconds if the system traps into the 5-membered ring complex (Figure 4.1), but for most trajectories it is in the 50 – 100 fs range. A more important time period is that between the onset of strong interaction and the point when the first new bond begins to form. This period (30 – 50 fs) is important because this first bond formation event is at or near the critical point in the collision; thus dynamics occurring after bond formation have no effect on the integral cross section and vibrational enhancements. The classical vibrational periods of the

different NO_2^+ modes range from 54 fs for the bend (010) to ~14 fs for the asymmetric stretch (001). The acetylene vibrational periods range from 55 fs to 9.9 fs. For the levels of excitation relevant for reactants, rotational time scales are tens of picoseconds. It can be seen that vibration is on a time scale comparable to the collision time, while rotational motion is very slow.

Linear NO_2^+ has two degenerate bend modes, corresponding to bending in the x-z or y-z plane, with classical turning point near 167° (i.e., ~13° from linear) for the (010) state (including zero point energy). In the (02^00) state, the bending motion is also in a single plane, with classical turning point of ~163° (17° from linear). The (02^20) state has one quantum in each of the orthogonal bend planes, 90° out of phase, such that the molecule classically is bent at a fixed angle of ~167°, rapidly "twisting" about what would be the molecular axis in linear NO_2^+. We use the term "twist" for this motion which occurs on a vibrational time scale (τ_{twist} ~ 35.4 fs), to draw the distinction with the usual rotation of NO_2^+ about an axis perpendicular to the molecular axis ($\tau_{rotation}$ ~ 40 picoseconds for J=1). From this classical perspective, the relevant differences between the two bend overtone states appear to be as follows: The (02^00) turning point is more bent than the fixed bend angle in the (02^20) state, the (02^00) state explores both linear and bent geometries, and the (02^20) state undergoes a high frequency twisting motion. The time-averaged bend angle for the two states is quite similar.

Typical Trajectories

Before discussing the results in detail, we first will briefly present typical non-reactive and reactive trajectories to illustrate the nature of the motion and changes in energy throughout the collision. The top half of Figure 4.4 summarizes a typical non-reactive trajectory, tracking the ONO bend angle, and distances from both O atoms to the N and C atoms as a function of time. The atom numbering scheme used to label the distances is shown in the inset. For example, RNO7 is the distance between the N atom and one of the O atoms, which happens to be atom number 7. Also shown are the potential energy (PE) of the system and the Mulliken charge on the C_2H_2 moiety. The oscillations in the various distances and ONO bend angle during reactant approach reflect the vibrations of the reactants, and it can be seen that the amplitudes are nearly constant during reactant approach, but have changed after the collision, reflecting translation-to-vibrational (T→V) energy transfer. The strong collisional interaction begins at about 120 fs, as indicated by both the PE and collision-induced distortion of the ONO angle. There is substantial transfer of charge to the C_2H_2 moiety during the strongly interacting phase of the collision. There is also a peak in the PE, during this phase of the collision, reflecting the fact that the interaction is predominantly repulsive.

The reactive trajectory shown in the bottom half the figure is generally similar. In this particular trajectory the transferred O atom (O7) initially bonds to both C atoms forming a three-membered ring (oxirene) structure, which subsequently rearranges to give the ketene product. Again there is substantial charge transfer to C_2H_2 during the

collision, but the changes in PE are not so obvious, indicating that the contributions from attractive and repulsive interactions roughly cancel.

Trajectory Validation

As discussed above, there are potential problems with the QCT method, and while we can argue that they may not be serious, the best test is how well the trajectories reproduce the experiments. Table 4.1 gives the calculated opacity functions, P(*b*), for the three states studied, and compares the resulting cross sections to those measured in the experiments. The error limits given for the trajectory cross sections are statistical, based on the number of trajectories (~970) calculated for each state, and obviously do not include any systematic errors. As discussed above, use of identical pseudorandom initial conditions for each trajectory set should significantly reduce the relative uncertainty in comparing the cross sections for reaction of different NO_2^+ states; however, it is difficult to quantify this reduction.

The uncertainty in the absolute scale of the experimental cross sections was estimated to be 20%, and we estimated that the relative uncertainty in comparing cross sections for difference vibrational states was ~15%. Considering that the cross sections are small, there are no adjustable parameters, and that the level of theory is necessarily modest, the agreement with the experimental absolute cross section is quite reasonable – within experimental error for the ground state. The fact that we did not calculate trajectories for b = 0.5 Å or below means that the trajectory cross section is a lower limit; however the effect should be small because such low b collisions are relatively infrequent. As discussed below, reaction at this energy is controlled to a large extent by collision

orientation; thus there is no reason to expect that P(b) will increase dramatically at small b. If we assume that P(b) for b < 1 Å is similar to the value at b = 1.0Å, then the correction to the cross section from these lower b collisions would be ~15%.

The more important result, both in the trajectories and experiments, is the cross section dependence on NO_2^+ vibrational state. The trajectories show the correct trend for the two excited states, with a greater enhancement for the (02^00) state compared to the (02^20) state. Note, however, that the magnitude of the vibrational enhancements is smaller in the trajectories than in the experiments. This "damping" of the vibrational effects is typical in our experience with QCT studies of vibrational effects[5,23-25] and we tentatively associate it with the failure to quantize vibrational motion.

The other experimental observation that the trajectories can be tested against is the product recoil velocity distribution. We do not expect QCT to be as accurate in calculating product properties because they are sensitive to accumulation of error throughout trajectories, whereas reactant effects depend only on early time behavior. Experimentally there are two product channels, $NO^+ + C_2H_2O$ and $NO + C_2H_2O^+$, which form in a ~4:1 ratio at high E_{col} but otherwise have nearly identical dynamics, including recoil behavior.[1] The trajectories are only able to probe the major channel, as this corresponds to the lowest Born-Oppenheimer surface. Despite these limitations, it is interesting to see how well the trajectories predict the recoil behavior.

The experiments measured only the projection of the full two-dimensional recoil velocity distribution on the axis of the instrument (the v_{axial} distribution). Because the experiment is cylindrically symmetric, the relative velocity vector of the collisions (v_{rel}) is

coincident, on average, with the instrument axis, thus the v_{axial} distribution provides several types of dynamical information. The top frame of Figure 4.5 shows the experimental v_{axial} distributions for the NO^+ product from reaction of NO_2^+ in its ground and (02^00) states at a nominal collision energy of 2 eV. The distributions are normalized such that the area under each curve is proportional to the integral cross section for that state. Note that the ground state distribution peaks at positive velocity, corresponding to forward scattering. The peak is quite broad, however, as might be expected if reaction occurred for a range of impact parameters, leading to scattering over a wide angular range from forward (large *b*) to backward (small *b*). For the (02^00) state, the growth in signal is mostly in the forward-scattered half of the distribution, which becomes considerably more forward peaked. A similar, but smaller shift to more forward scattering was observed for the (02^20) state. These changes indicate that the vibrational enhancement comes mostly from collisions that result in more strongly forward-scattered products. In fact the peak of the distributions shift to near the velocity expected for a spectator stripping mechanism (dashed vertical line labeled V_{SS}).

The lower frame of the figure shows the analogous trajectory v_{axial} distributions (lines with data points) generated by adding together the *b*-weighed distributions calculated from the sets of trajectories at b = 1, 1.5, 2, and 2.5Å (although none of the 2.5Å trajectories reacted). The area under each curve is proportional to the trajectory integral cross section. The three curves without data points show how each range of impact parameter contributes to the v_{axial} distribution for the ground state reaction. As expected, as *b* is increased, the scattering shifts forward. If we had calculated trajectories at $b \leq$

0.5Å, these presumably would have contributed primarily to the backward-scattered tail, improving agreement with the experimental distributions. The agreement between the trajectories and experiments is not bad, considering the limitations of the calculations. The overall shape of the distributions is reasonably consistent, and the vibrational enhancement comes almost entirely from collisions that lead to forward-scattered products.

Note, however, that the trajectories suggest a reinterpretation of the origin of the vibrational effects on reactivity and recoil behavior. The obvious interpretation for a simultaneous increase in reactivity and shift toward more forward-scattered products is that vibrational excitation increases reaction probability at large impact parameters, which tend to scatter forward. Table 4.1 shows that vibrational excitation, instead, enhances reaction probability at intermediate values of *b*, with no enhancement at large impact parameters. Instead, the increase in forward-scattered intensity with vibrational excitation in the trajectories results from two changes in scattering behavior for these intermediate *b* collisions. The angular distribution calculated at b = 1.5 Å shifts to smaller scattering angles with vibrational excitation – the peak shifts from ~65° for ground state NO_2^+ , to ~50° for the (02^00) state. In addition, the recoil energy increases with vibrational excitation. Both factors contribute to the shift to higher axial velocities.

In summary, the trajectories correctly predict the absolute cross section magnitude and qualitative trends in cross section versus vibrational state, and even the product scattering is qualitatively right. We, therefore, feel justified in analyzing trajectory details to extract further dynamical insight.

Dependence on Bend Angle

One obvious question, given the strong enhancement from bend excitation, is whether reaction probability is a simple function of the bend angle at some critical point in the collision. For low energies the obvious critical point would be TS1; however, at high E_{col} trajectories do not follow the minimum energy path, and therefore the choice of an event to "trigger" recording the collision geometry is somewhat arbitrary. The ideal trigger should be early enough in the trajectory that collisional forces have not strongly distorted the reactants, but late enough that vibration or rotation does not significantly change the geometry in the time between the trigger and the onset of the strong collisional interaction. In past studies we have used the point where the potential energy (PE) first deviates significantly from the range of PE corresponding to zero-point motion of the reactants, or when some bond length goes outside the range expected for vibration of the reactants. In this system a wide variety of behavior is seen in the trajectories, and neither method provides a reliable trigger. Based on viewing hundreds of trajectories, we have chosen to record the collision geometry for each trajectory at the time step when the shortest CO distance first drops below a particular value. For most of the analysis below, this trigger distance was 2.5 Å, which is typically reached just as collisional distortion of the reactant geometry becomes obvious (see Figure 4.4, where this trigger distance ($4.7a_0$) is indicated).

The top frame of Figure 4.6 plots the distributions of the ONO bend angle ("aBend") recorded at the 2.5 Å trigger point for all three states. As expected, the ground state (GS) has a narrower distribution of bend angle, peaking at >170°. The distributions for

the ($02^{0}0$) and ($02^{2}0$) states are broadened and shifted to smaller angle compared to the ground state (GS), and as expected, the ($02^{2}0$) distribution does not extend to linear geometries but also peaks at larger aBend than the ($02^{0}0$) distribution. The small angle tail in the GS distribution, and the breadth of all three distributions, reflect the fact that for this trigger distance, there are some trajectories where collisional interaction has already begun to distort the NO_2^+. Further discussion of bend angle distribution changes with trigger distance is given below.

The lower frame of the figure gives the reaction probability as a function of aBend, i.e., the fraction of reactive trajectories in each range of aBend, averaged over the impact parameters studied with appropriate weighting. The main conclusion is that reaction probability is at most weakly dependent on NO_2^+ state, and also on aBend, over the ranges of aBend that each state explores. Therefore we cannot rationalize the increase in cross section with bend excitation as simply being due to increased probability of colliding in a bent geometry. It is true that the ground state appears to have a spike in reactivity around 160° (and zero reactivity for aBend $\leq$ 150°); however, the number of ground state collisions in this range of aBend is too small to have much effect on the cross section. Clearly, to understand why the different NO_2^+ vibrational states react with different efficiencies, we need to look further.

The Nature of the Bottleneck to Reaction

Before we get further into the details of the molecular motions that enhance and inhibit reaction in this system, it is useful to examine the nature of the bottleneck that controls reactivity. At low E_{col}, RRKM analysis clearly shows that TS1 is the rate-

limiting TS, and that decay of RC through TS1 can explain the sharp reactivity spike at low energies.[1] TS1 represents a point where CO bonds begin to form, and at low energies reaction is only energetically possible if two CO bonds form concertedly, generating the five-membered ring complex. Distortions away from the C_{2v} TS1 geometry such that only one CO bond can form initially, are energetically inaccessible at low E_{col}, and this strong orientation dependence is evidently the cause of the very low reaction efficiency (0.5 – 2.2% for E_{col} < 1 eV for ground state).

At high E_{col}, the system can react in less symmetric geometries. Indeed, only ~30% of reactive trajectories still go through a five-membered ring intermediate, and even in those, the two CO bonds usually form sequentially. The dominant mechanism involves collisions where only one CO bond ever forms, leading directly to $(NO + C_2H_2O)^+$ products by NO bond scission. The ability to react in collisions where only one O atom needs to interact with one C atom raises the question of whether collision orientation can still account the fact that reaction efficiency is only ~10% for ground state NO_2^+ at E_{col} 2 eV. One might imagine that such C-O interactions would occur in a larger fraction of collisions.

It turns out that collision orientation is still a significant controlling factor. One parameter of interest is the angle between what would be the molecular axes of the two reactants, if they were linear at the trigger point. We will call this angle “aCross”, and it is indicated on the schematic of the collision geometry in Figure 4.7.

The top frame of Figure 4.8 shows the reaction probability for all three states (lines with symbols, left hand scale), as a function of the value of aCross recorded at the same

2.5Å trigger point used for the analysis of the aBend dependence of reactivity. aCross = 0° corresponds to reactants colliding in a parallel geometry. aCross = 90° describes a range of geometries with the two limiting structures indicated by sketches superimposed on the aCross = 90° axis. For all three states, reactivity generally declines at high aCross, indicating a propensity to react in parallel configurations. The ground state reactivity peaks at aCross ~ 0°, while the two bend states show peak reactivity for aCross ~15°. Also shown in the top frame of the figure (heavy lines with no symbols, right hand scale), is the probability of colliding with aCross in a particular angular range (the probability is proportional to sin(aCross), within the statistical uncertainty). The product of the collision probability and reaction probability is the contribution of collisions in each range of aCross to the cross section, and this is plotted in the lower frame of the figure. Note that the differences in reaction probability at small aCross for the different states have no significant effect on the cross section. Instead, it is the higher reaction probability at aCross >30° for the two bend overtone states that which has the dominant effect. In any case, it is clear that orientation of the reactants is still an important factor.

Figure 4.6 showed that ONO bend angle, aBend, was not, by itself, a major factor controlling reactivity. There may be more to this issue, however, because the effect of bend angle may be correlated with other geometric parameters, such that one-dimensional plots such as Figure 4.6 cannot reveal the dynamics. We examined several two-dimensional correlations of reactivity vs. pairs of angles. For example, it seemed likely that aBend might have different effects for collisions in different ranges of aCross;

however, within the statistical uncertainty of the trajectory set, the aBend and aCross effects are not correlated.

A more interesting correlation was found between the effects of aBend and a dihedral angle we will call "dOrient" (Figure 4.7). dOrient describes the orientation of the ONO plane with respect to the plane containing the C_2H_2 CC backbone and the O atom that is attacking it. In essence dOrient tells whether the ONO is oriented such that its O atoms are bent toward the acetylene (small dOrient) or away from the acetylene (large dOrient). Figure 4.9 shows the correlated distributions of aBend and dOrient for all collisions ("All"), and also for only the subset of reactive collisions ("Reactive"). Distributions are given for the three NO_2^+ reactant states, and for geometries recorded at a series of trigger distances, defined as described above. First consider the all collisions distributions for ground state NO_2^+ in the left-most column of the figure. For the 4Å trigger point, the aBend distribution is, as expected, independent of dOrient within the statistical uncertainty, peaking near 175° and extending to 160°. By the time the trajectories reach the 3.0 Å trigger, there already is some correlation between the two angles, growing quite strong as the reactants approach to smaller separations. The dOrient distribution ultimately splits into two components, indicating that there is a strong torque on ONO orienting its bend plane either parallel or antiparallel to the CC-O plane. One component becomes quite sharply peaked near dOrient = 180° (ONO with the O atoms "bent away" from C_2H_2), and for this component the aBend distribution broadens and shifts to smaller angles (more strongly bend ONO) as the trigger distance decreases. The other component becomes increasingly peaked near dOrient = 0° (ONO with O atoms bent

toward C_2H_2) and for this component aBend also broadens and shifts to smaller angles, but less dramatically than for the "bent away" component.

The next column of the figure shows that the "bent away" component is entirely missing in the distribution of reactive collisions, while the "bent toward" component is present with lower intensity than in the all collisions distribution. The implication is that only ONO bent with its O atoms toward C_2H_2 can react, and that the reaction efficiency even for this favorable component is less than unity. Note that for all trigger distances, the shapes of this "bent toward" component are quite similar in the distributions of "all" and "reactive" trajectories; i.e., the fraction that react is not obviously dependent on the aBend angle.

The middle two columns of the figure show the analogous distributions for all and reactive collisions of NO_2^+ (02^00). At 4.0 Å distance the aBend distribution peaks near 165° and extends from 150° to 180° (i.e., this state inverts through the linear equilibrium geometry). Note that, as expected, the "all collisions" distribution shows no correlation between aBend and dOrient, however, for reactive collisions there is a weak correlation. Trajectories with ONO *bent away* are more reactive when sampled at 4.0Å trigger distance. The behavior as the trigger distance is reduced is generally similar to that for ground state NO_2^+. The distribution splits into two components, with reaction seen only for NO_2^+ which is *bent toward* C_2H_2. The change in reactive trajectories from "bent away" at 4.0 Å to "bent toward" for 2.7Å and shorter distances, reflects the time scale of the collisions. The time it takes reactants to move from 4Å to 2.7Å separation at 2 eV relative energy (~27 fs) is just about half the period of the bend vibration, thus to be bent

in the favorable (toward) orientation as the collision begins, the NO_2^+ should be bent away at 4Å. The one significant difference between the ground state and (02^00) behavior is that trajectories are reactive for the (02^00) state over a wider range of dOrient than for the ground state. This lower sensitivity to orientation is presumably associated with the higher reaction efficiency for this state. It is important to note that the increased range of reactive dOrient is *not* found only for those trajectories where NO_2^+ is more strongly bent at the "moment of collision" – the enhancement is found for the entire range of aBend explored by the states. It appears that some combination of bending distortion and the momentum associated with the bending motion are responsible for the ability to react in less favorable orientations.

One of the questions we are most interested in is why the (02^20) state is less reactive than the (02^00) state. The right two columns of Figure 4.9 give analogous aBend/dOrient maps for the (02^20) state. At 4Å, the aBend distribution for this state peaks at 162° (similar to the (02^00) distribution), but is considerably narrower (155° < aBend < 175°). There is no population at aBend > 175°, i.e., this state never samples the linear equilibrium geometry, instead twisting about the linear axis at ~fixed bend angle (the angle fluctuates somewhat due to zero-point motion). As in the ground state and (02^00) distributions, the reactive trajectories at 4Å already show some propensity for bending away, switching to a strong preference for bending toward at shorter trigger distances.

The question remains, why the (02^20) state is less reactive than the (02^00) state. Our hypothesis is that the momentum associated with the twisting motion in the (02^20) state makes it difficult for the reactants to remain in the favorable, bent-toward, orientation

long enough for the necessary CO bond(s) to form. In essence, this twisting momentum is perpendicular to the reaction coordinate. In contrast, those collisions of the (02^00) state that reach the critical distance (~2.5Å) in the bent-toward geometry experience no forces that would tend to disturb the orientation. As shown in Figure 4.9, these reactive trajectories are ones where the vibration has brought the O atom(s) into the favorable orientation just at the point where the forces between C and O atoms begin to be strongly attractive, thus the O atom vibrational momentum reinforces the chemical forces driving CO bond formation.

Intracomplex Charge Transfer

In an earlier experimental and trajectory study of NO_2^+ collisional excitation and dissociation in collisions with Kr atoms,[5] it was found that efficient energy transfer was strongly correlated to the degree of transient charge transfer to the Kr moiety during the collision. In all collisions, charge delocalization leads to transfer of at least 40% of the Mulliken charge to the Kr moiety during the strongly-interacting phase of the collision. For most collisions, the charge on Kr never exceeds 50%, and there is also very little T → V transfer, and no dissociation even at energies nearly double the dissociation threshold. A small subset of trajectories – those where the NO_2^+ became strongly bent during the collisions – resulted in > 80% charge transfer to Kr, and these trajectories ***all*** resulted in large T → V transfer, and 100% dissociation. In other words, transient charge transfer to Kr acts as a switch that turns on efficient energy transfer. The mechanism is also obvious in the trajectory results. Both reactants in the NO_2^+ + Kr system are closed shell, but with charge transfer the system becomes a radical-radical system. Kr^+ attacks

NO_2, forms a Kr-O bond, disrupts the NO bonding, and when the charge transfers back the system is left either dissociated, or with vibrational excitation above the dissociation threshold. NO_2^+ vibrational excitation enhances the energy transfer/dissociation process, because bending, and to a lesser extent stretching, raise the energy of the NO_2^+ + Kr reactant state, and lower the energy of the Kr^+ + NO_2 charge state.

Similar considerations should apply in the NO_2^+ + C_2H_2 system. As shown in Figure 4.3, NO_2^+ vibrational excitation should help drive the system onto the part of the lowest Born-Oppenheimer surface where the charge is transferred to the acetylene reactant, and the $C_2H_2^+$ + NO_2 combination should be substantially more reactive than the closed shell NO_2^+ + C_2H_2 reactants. Therefore, it is interesting to look at the degree of charge transfer during collisions, and how this correlates with reactivity. A representative set of reactive and nonreactive trajectories was reexamined, with the Mulliken charge calculated at every step during the strongly-interacting portion of the trajectory. The fraction of the Mulliken charge appearing on acetylene is shown for a typical pair of trajectories in Figure 4.4. At least for the set of trajectories examined, it is true that all reactive trajectories involve considerable transient charge transfer during the collision (> 60%). On the other hand, some, but not all, non-reactive trajectories also involve substantial intra-complex charge transfer, as shown in Figure 4.4. That such trajectories are non-reactive is simply the result of the strong dependence of reactivity on dOrient. Many of the trajectories in the "bent away" components (dOrient near 180°) of the "All" collisions distributions undergo substantial charge transfer, resulting in distortion to small ONO angles. None of these trajectories can react, because the O atoms are bent away from the

C_2H_2 reactant. The analogous "bent-away" collisions are also unreactive in the NO_2^+ + Kr system, but in addition they also never result in substantial charge transfer, presumably because more extreme distortion of the ONO is required to drive charge transfer in that system because Kr has a much higher ionization energy (14.0 eV) than C_2H_2 (11.4 eV). Kr-O bonding is essential to help drive this extreme distortion, and as a consequence there is a one-to-one correspondence between charge transfer and dissociation. In the present system, the system can be driven into geometries corresponding to charge transfer more easily, thus the correlation between charge transfer and reaction is weakened.

Conclusions

Quasi-classical trajectories calculated at the PBE1PBE/6-311G** level of theory are able to reproduce the magnitude of the absolute reaction cross section for oxygen transfer in NO_2^+ + C_2H_2. In addition, the QCT results get the dependence of reactivity on NO_2^+ vibrational state, and the vibrational state dependent scattering behavior qualitatively correct. Analysis of the trajectories shows that the bending effect is not simply a consequence of enhanced reactivity in bent geometries, but rather, that excitation of bending motion allows reaction in a wider range of orientation angles, even if the NO_2^+ is not bent at the onset of the strongly interacting phase of the collision. The effect is attributed to the fact that bending momentum is coupled to the reaction coordinate for CO bond formation, which is the rate-limiting step in the reaction. The suppressing effect of bending angular momentum is attributed to the fact that its momentum is essentially perpendicular to the CO bond formation coordinate. There is a strong interplay between

NO_2^+ bending and transient charge transfer during the collisions. Such charge transfer enhances reactivity, but only if the reactants are oriented correctly.

References

1. J. M. Boyle, B. W. Uselman, J. Liu, S. L. Anderson, J. Chem. Phys. 128, 114304 (2008).

2. B. J. Orr, Chem. Phys. 190, 261 (1995).

3. A. E. Depristo, L. C. Geiger, Surf. Sci. 176, 425 (1986).

4. D. C. Clary, J. Chem. Phys. 75, 209 (1981).

5. J. Liu, B. W. Uselman, J. M. Boyle, S. L. Anderson, J. Chem. Phys. 125, 133115/1 (2006).

6. C. Kreher, R. Theinl, K. H. Gericke, J. Chem. Phys. 104, 4481 (1996).

7. J. Liu, B. Van Devener, S. L. Anderson, J. Chem. Phys. 123, 204313/1 (2005)

8. J. Liu, B. Van Devener, S. L. Anderson, J. Chem. Phys. 121, 11746 (2004).

9. J. Liu, B. Van Devener, S. L. Anderson, J. Chem. Phys. 119, 200 (2003).

10. H.-T. Kim, R. J. Green, S. L. Anderson, J. Chem. Phys. 113, 11079 (2000).

11. H.-T. Kim, R. J. Green, S. L. Anderson, J. Chem. Phys. 112, 10831 (2000).

12. R. J. Green, H.-T. Kim, J. Qian, S. L. Anderson, J. Chem. Phys. 113, 4158 (2000).

13. J. Qian, R. J. Green, S. L. Anderson, J. Chem. Phys. 108, 7173 (1998).

14. H. Fu, J. Qian, R. J. Green, S. L. Anderson, J. Chem. Phys. 108, 2395 (1998).

15. J. Qian, H. Fu, S. L. Anderson, J. Phys. Chem. 101, 6504 (1997).

16. S. L. Anderson, Acc. Chem. Res. 30, 28 (1997).

17. Y.-H. Chiu, H. Fu, J.-T. Huang, S. L. Anderson, J. Chem. Phys. 105, 3089 (1996).

18. J. Liu, B. Uselman, B. Van Devener, S. L. Anderson, J. Phys. Chem. A, 108, 9945 (2004).

19. U. Lourderaj, E. Martinez-Nunez, W. L. Hase, J. Phys. Chem. A, 111, 10292 (2007).

20. W. L. Hase, K. Bolton, P. de Sainte Claire, R. J. Duchovic, X. Hu, A. Komornicki, G. Li, K. Lim, D. Lu, G. H. Peslherbe, K. Song, K. N. Swamy, S. R. Vande Linde, A. Varandas, H. Wang, and R. J. Wolf, VENUS99: A general chemical dynamics computer program (1999).

21. V. Bakken, J. M. Millam, H. B. Schlegel, J. Chem. Phys. 111, 8773. (1999).

22. M. J. Frisch, G. W. Trucks, H. B. Schlegel, G. E. Scuseria, M. A. Robb, J. R. Cheeseman, J. J. A. Montgomery, T. Vreven, K. N. Kudin, J. C. Burant, J. M. Millam, S. S. Iyengar, J. Tomasi, V. Barone, B. Mennucci, M. Cossi, G. Scalmani, N. Rega, G. A. Petersson, H. Nakatsuji, M. Hada, M. Ehara, K. Toyota, R. Fukuda, J. Hasegawa, M. Ishida, T. Nakajima, Y. Honda, O. Kitao, H. Nakai, M. Klene, X. Li, J. E. Knox, H. P. Hratchian, J. B. Cross, C. Adamo, J. Jaramillo, R. Gomperts, R. E. Stratmann, O. Yazyev, A. J. Austin, R. Cammi, C. Pomelli, J. W. Ochterski, P. Y. Ayala, K. Morokuma, G. A. Voth, P. Salvador, J. J. Dannenberg, V. G. Zakrzewski, S. Dapprich, A. D. Daniels, M. C. Strain, O. Farkas, D. K. Malick, A. D. Rabuck, K. Raghavachari, J. B. Foresman, J. V. Ortiz, Q. Cui, A. G. Baboul, S. Clifford, J. Cioslowski, B. B. Stefanov, G. Liu, A. Liashenko, P. Piskorz, I. Komaromi, R. L. Martin, D. J. Fox, T. Keith, M. A. Al-Laham, C. Y. Peng, A. Nanayakkara, M. Challacombe, P. M. W. Gill, B. Johnson, W. Chen, M. W. Wong, C. Gonzalez, and J. A. Pople, (Gaussian, Inc., Pittsburgh PA, 2003).

23. J. Liu, K. Song, W. L. Hase, S. L. Anderson, J. Phys. Chem. A, 109, 11376 (2005).

24. J. Liu, K. Song, W. L. Hase, S. L. Anderson, J. Am. Chem. Soc. 126, 8602. (2004).

25. J. Liu, K. Song, W. L. Hase, S. L. Anderson, J. Chem. Phys. 119, 3040. (2003).

26. *CRC Handbook of Chemistry and Physics*, edited by R. C. Weast, M. Astle, J., and W. H. Beyer (CRC Press, Boca Raton, 1985).

27. P. Chantry, J. J. Chem. Phys., 55, 2746. (1971).

28. W. H. Press, S. A. Teukolsky, W. T. Vetterling, B. P. Flannery, *Numerical Recipies in C. The Art of Scientific Computing*, 2nd ed.; (Cambridge University Press: Cambridge, 1992).

29. L. Laaksonen, gOpenMol (available at www.csc.fi/gopenmol/, Espoo, Finland, 2002).

30. W. H. Miller, W. L. Hase, C. L. Darling, J. Chem. Phys. 91, 2863 (1989).

31. A. Untch, R. Schinke, R. Cotting, Huber, J. R. J. Chem. Phys. 99, 9553. (1993).

Table 4.1.

Trajectory Opacity Functions and Cross Sections.

Comparison with Experimental

Absolute Cross Sections

Impact Parameter b (Å)	Reactant State		
	GS	$02^{0}0$	$02^{2}0$
1.0	0.328	0.397	0.331
1.5	0.265	0.347	0.281
2.0	0.140	0.140	0.140
2.5	0.000	0.000	0.000
σ (Å^2) trajectory	3.16 ± 0.35	3.76 ± 0.36	3.25 ± 0.38
σ (Å^2) expt	2.79	5.36	4.13

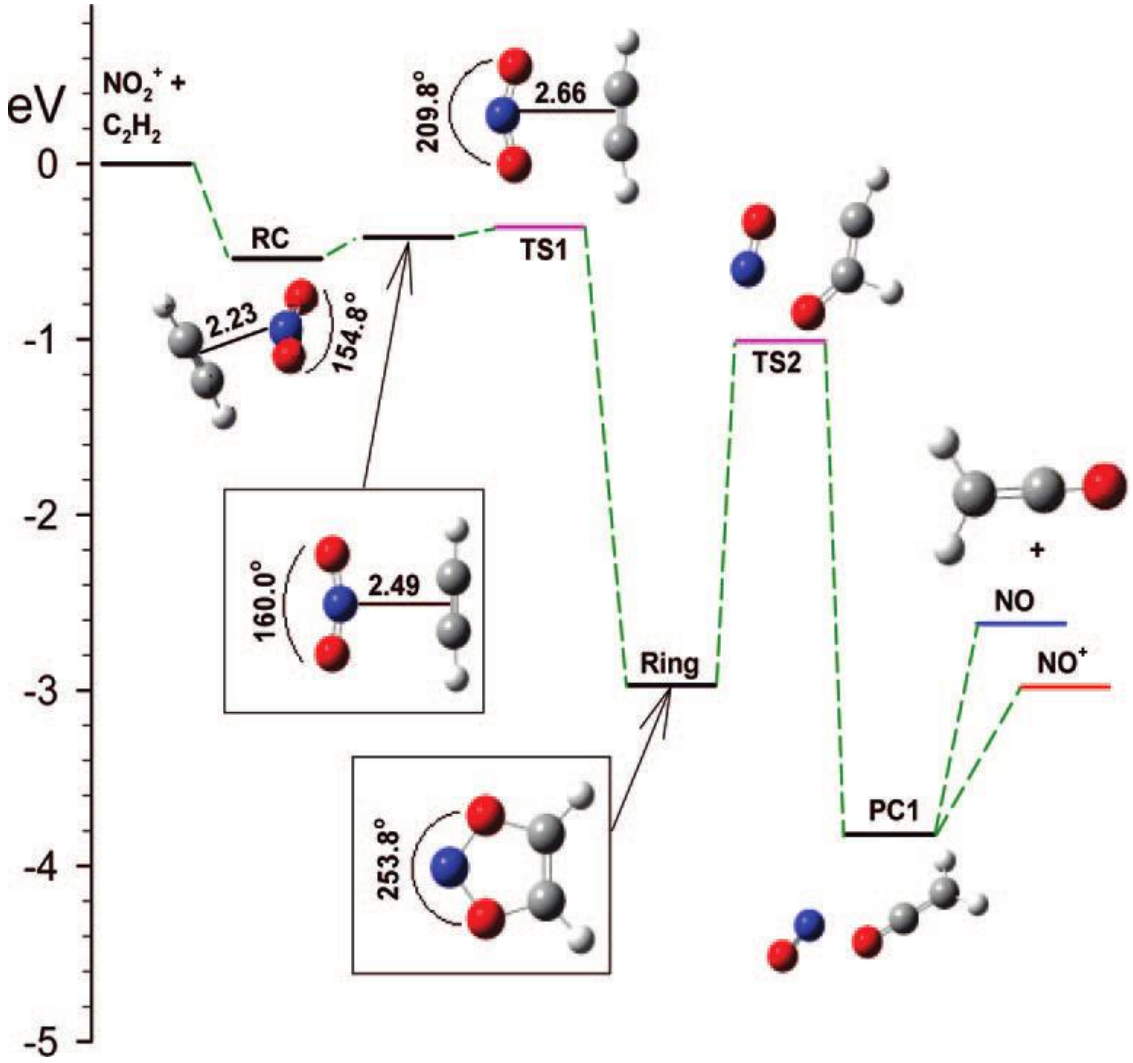

Figure 4.1. Reaction coordinate connecting NO_2^+ and C_2H_2 reactants to the two charge states of the [NO + ketene]$^+$ products. Distances labeled in inset images are in angstroms.

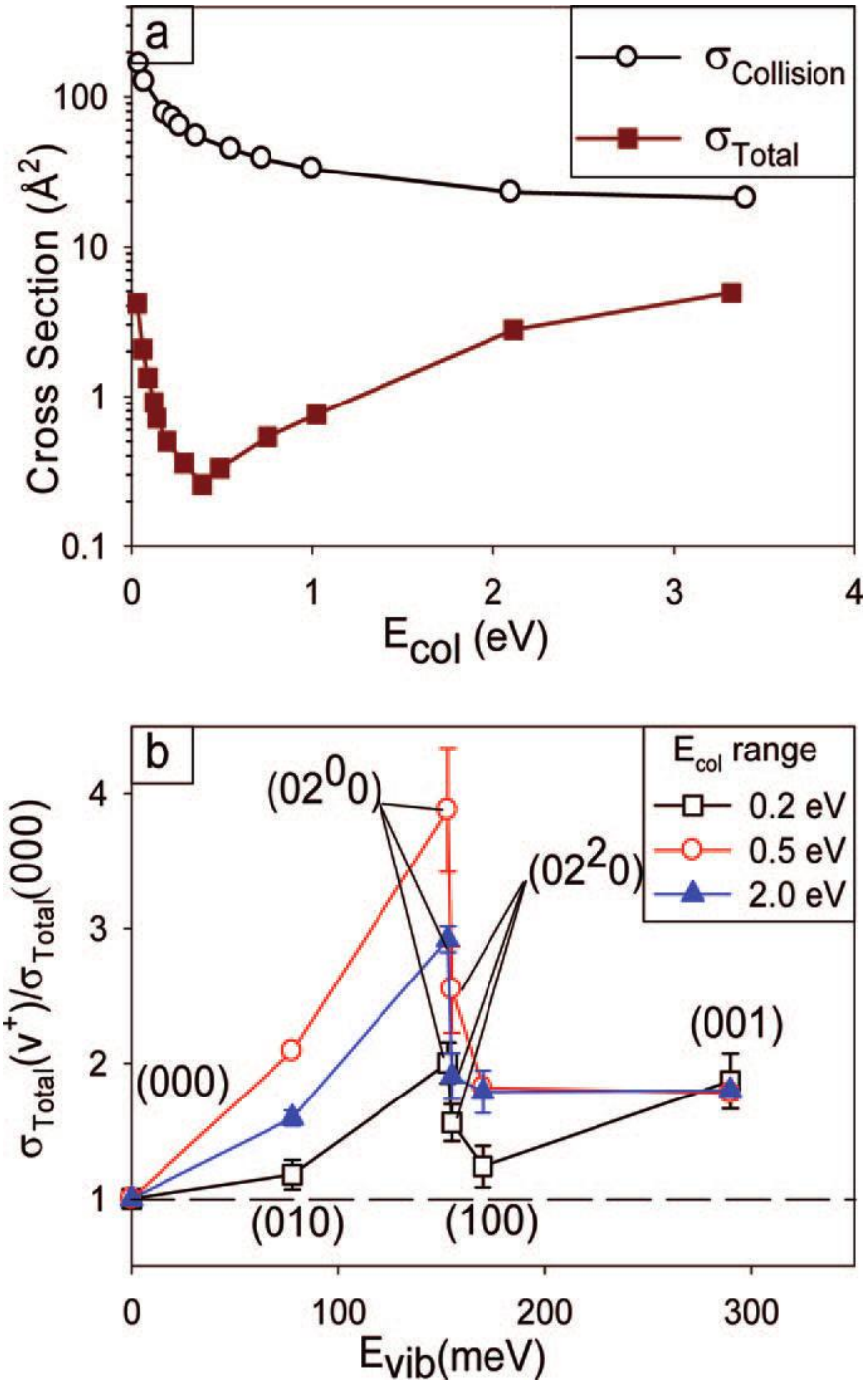

Figure 4.2. **(**a) Comparison of the collision cross section and the experimental total cross section for reaction of ground state NO_2^+ with C_2H_2 as a function of collision energy. (b) Vibrational enhancements factors, $\sigma(n_1n_2n_3)/\sigma(000)$ in three collision energy ranges. Error bars are the standard deviations of data taken on separate days.

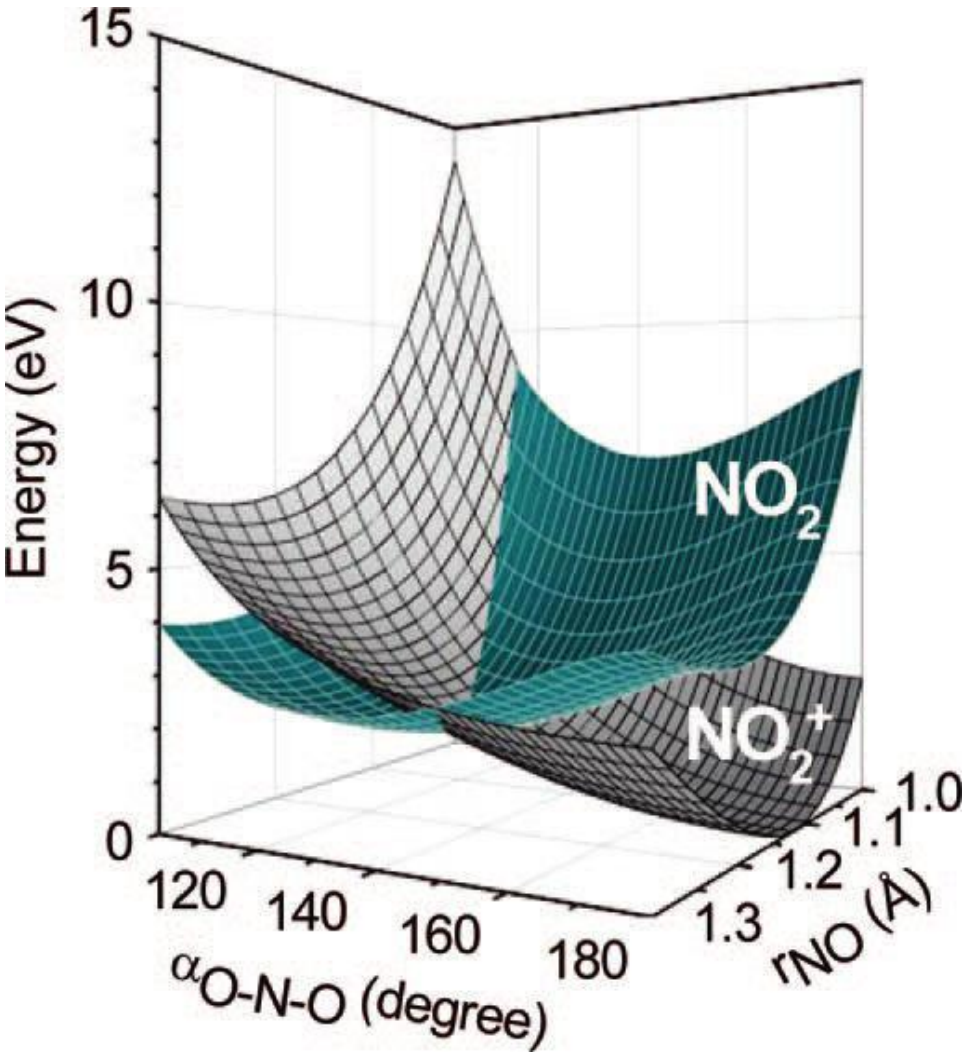

Figure 4.3. Cut through the potential energy surfaces for the $(NO_2 + C_2H_2)^+$ system along the NO_2 bend and symmetric stretch coordinates, at infinite reactant separation.

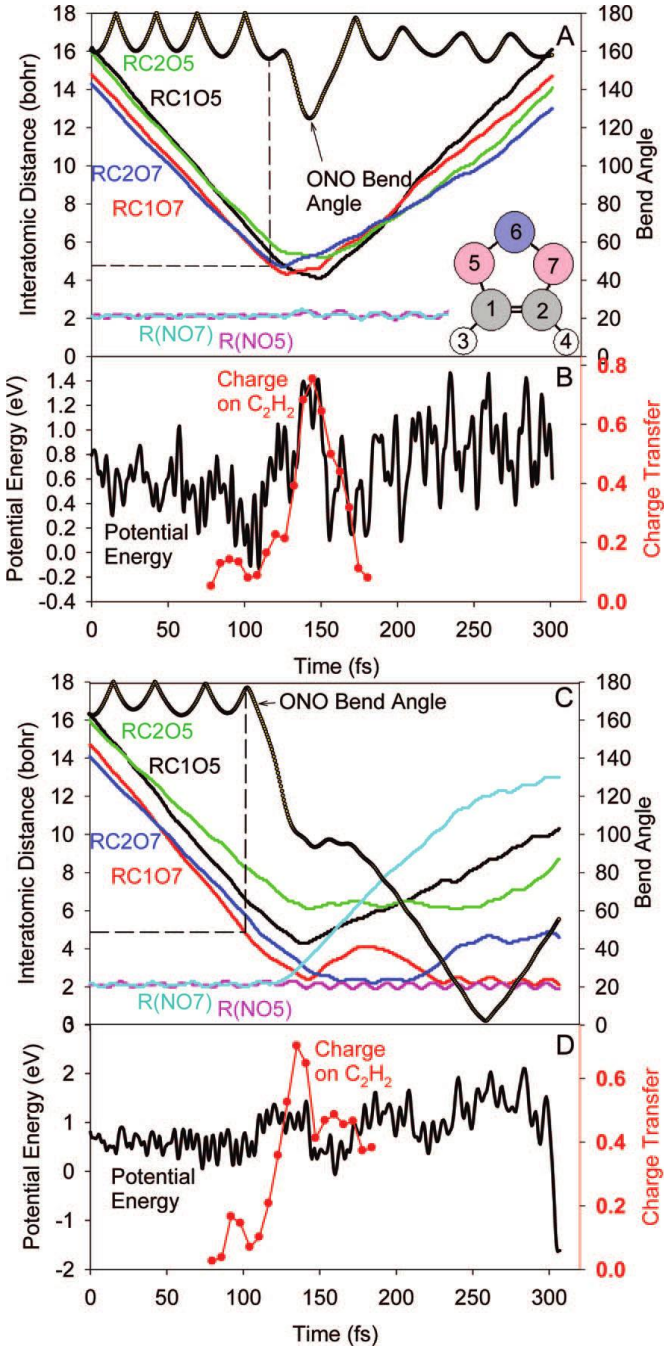

Figure 4.4. (A) Values of several geometric parameters as a function of trajectory time for a typical nonreactive (02^00) trajectory. The inset (5-membered ring structure) shows the atom numbering. The dashed lines indicate the trigger distance used in most of the analysis (2.5Å). (B) Potential energy (left scale) and Mulliken charge on the C_2H_2 moiety (right scale). (C and D) Same parameters recorded for a reactive (02^00) trajectory.

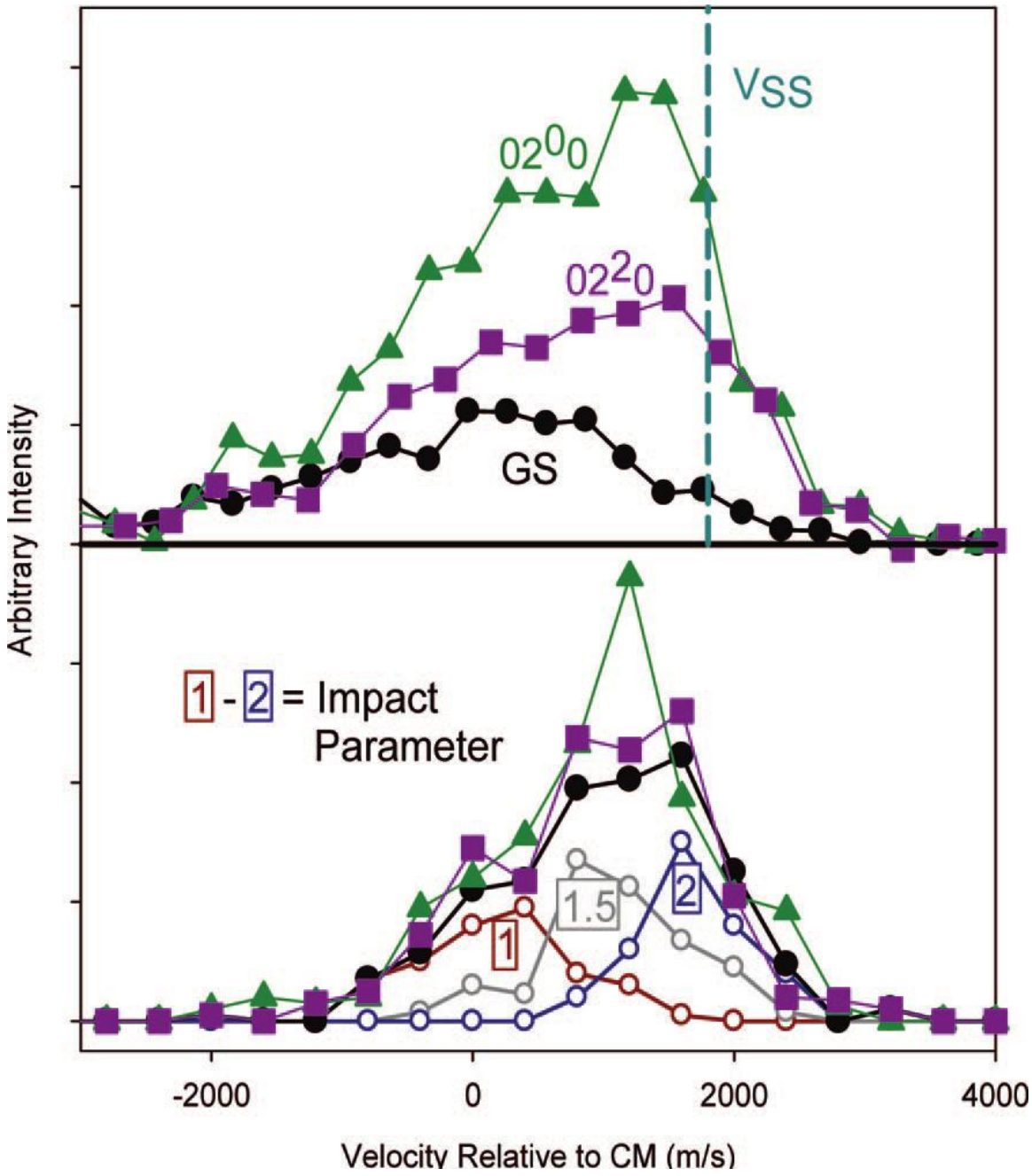

Figure 4.5. NO^+ product recoil axial velocity distributions at nominal collision energy of 2 eV: (top) experimental, with the spectator stripping velocity indicated as V_{SS}; (bottom) QCT distributions (filled symbols). Also shown are the contributions to the ground state distribution from different ranges of impact parameter (open symbols).

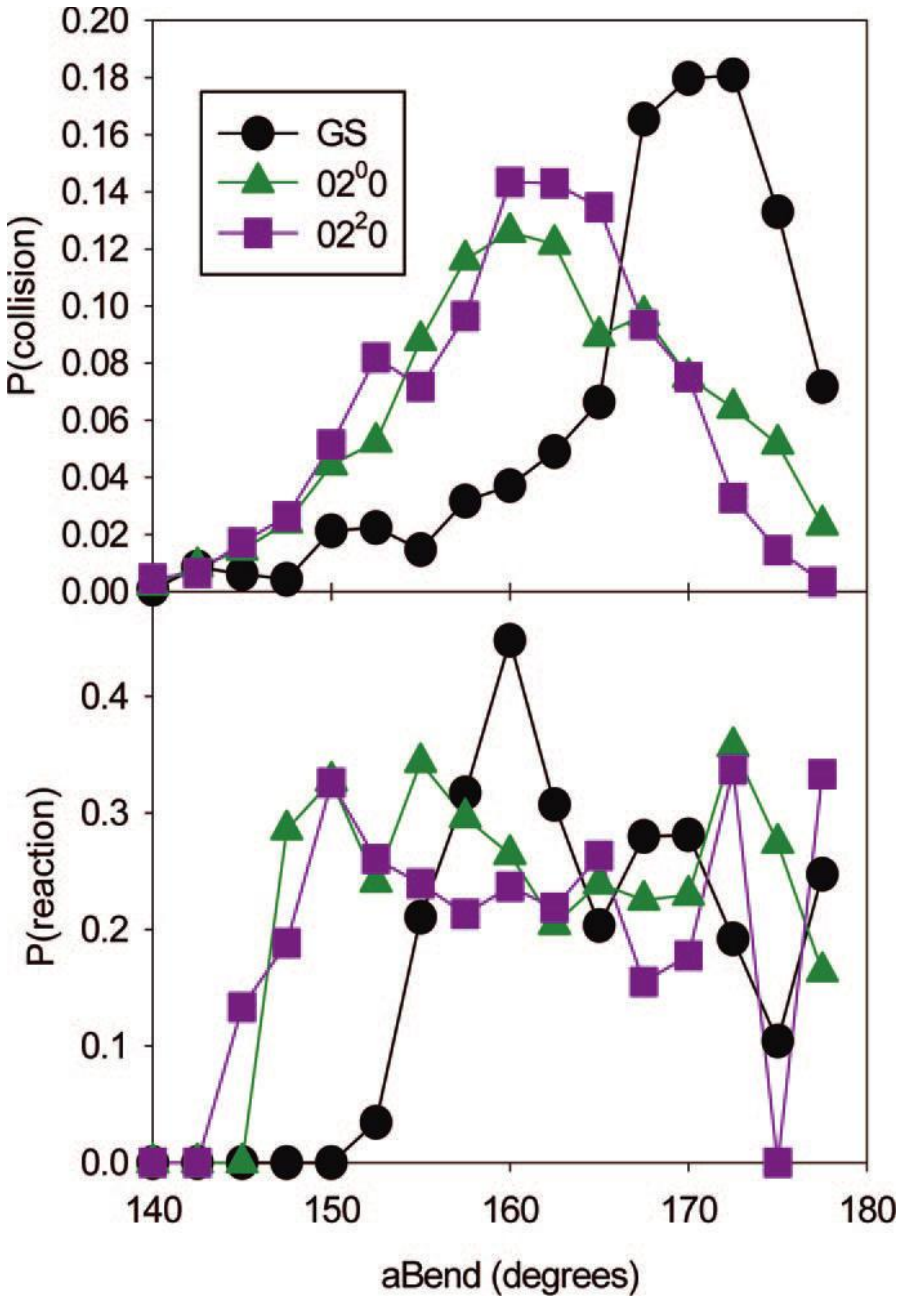

Figure 4.6. (Top) Distributions of the ONO bend angle (aBend) recorded at the trigger point for the ground, ($02^{0}0$), and ($02^{2}0$) states. (Bottom) Reaction probability for trajectories that have different values of aBend at the trigger point.

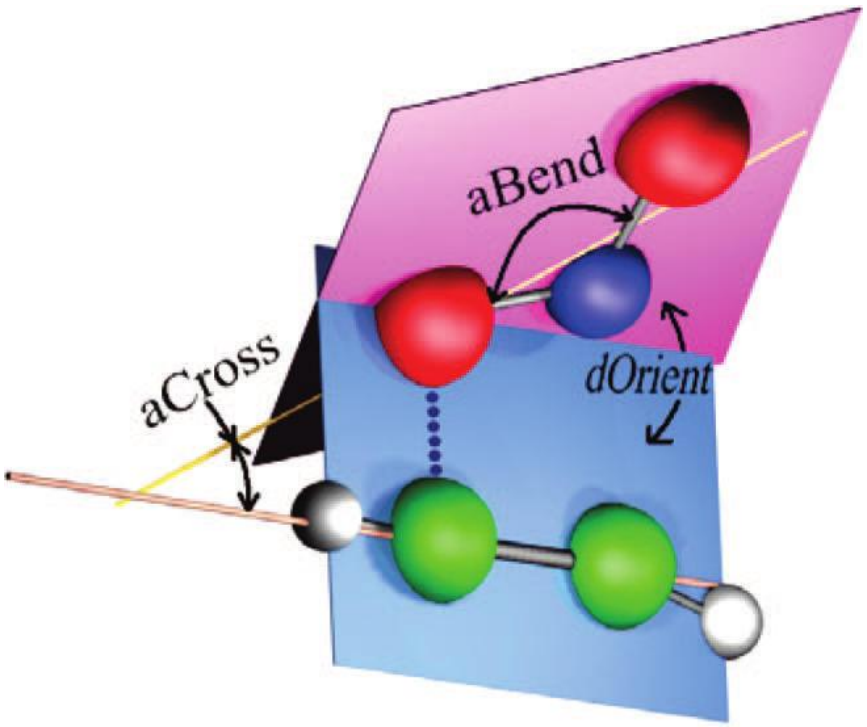

Figure 4.7. Definition of aCross and dOrient angles.

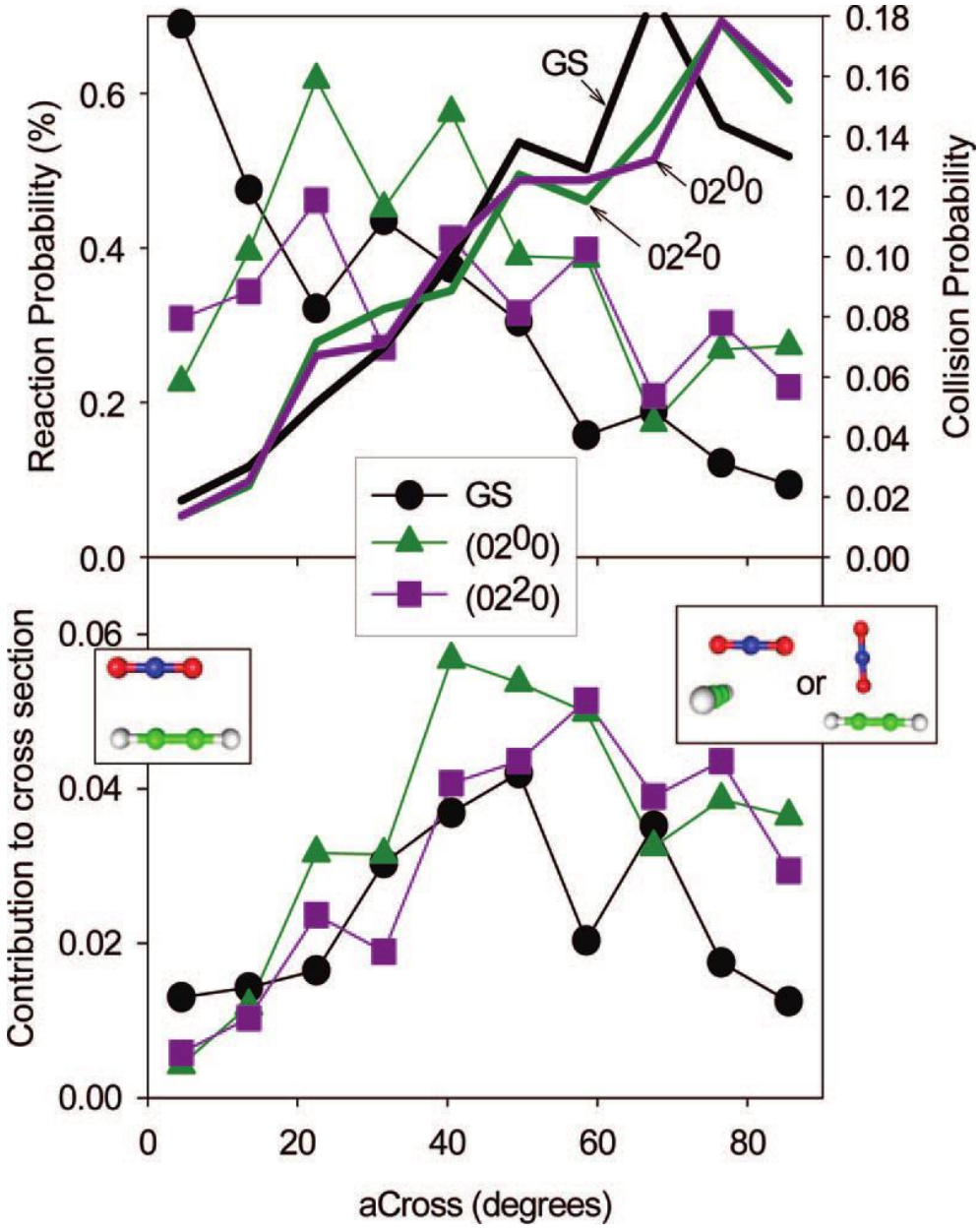

Figure 4.8. (Top) Curves with symbols (left scale) show reaction probabilities as a function of the aCross angle recorded at the trigger point. Curves without symbols show the probability of trajectories having different values of aCross at the trigger point. (Bottom) The contribution of trajectories in each range of aCross to the reaction cross section.

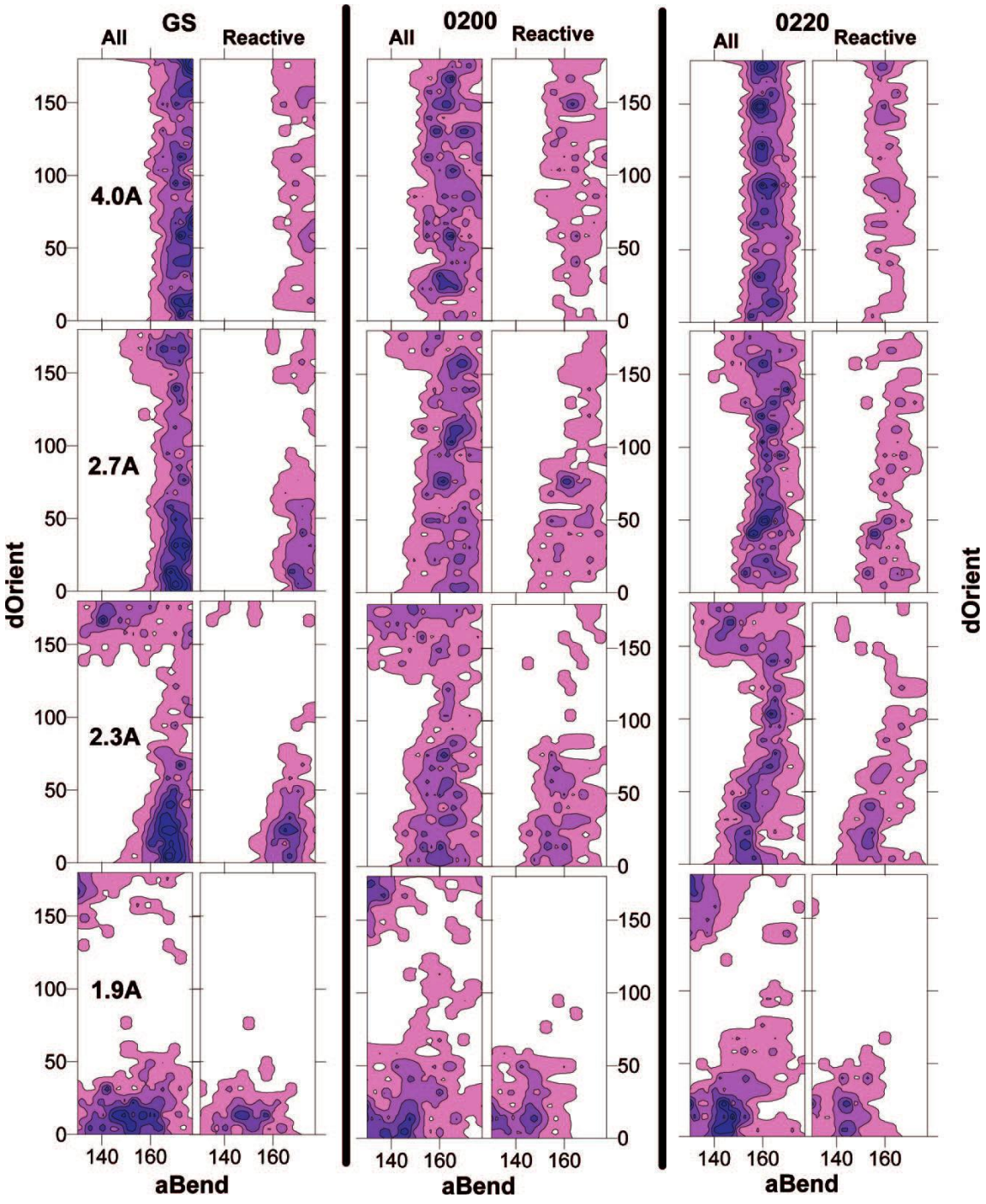

Figure 4.9. Reactivity vs dOrient (vertical axes) and aBend (horizontal axes) with geometries recorded at four different trigger points (4.0Å, 2.7Å, etc listed in the left column). Results are shown for all trajectories ("All") and for the reactive trajectories ("Reactive") for the ground (GS), $02^{2}0$ and $02^{0}0$ states.

CHAPTER 5

REACTION OF $C_2H_2^+$ ($n \cdot \nu_2$, $m \cdot \nu_5$) WITH NO_2: REACTION ON THE SINGLET AND TRIPLET SURFACES

Overview

Integral cross sections and product recoil velocity distributions were measured for reaction of $C_2H_2^+$ with NO_2, in which the $C_2H_2^+$ reactant was prepared in its ground state, and with mode-selective excitation in the cis-bend ($2\nu_5$) and CC stretch ($n\cdot\nu_2$, n = 1, 2). Because both reactants have one unpaired electron, collisions can occur with either singlet or triplet coupling of these unpaired electrons, and the contributions are separated based on distinct recoil dynamics. For singlet coupling, reaction efficiency is near unity, with significant branching to charge transfer (NO_2^+), O^- transfer (NO^+), and O transfer ($C_2H_2O^+$) products. For triplet coupling, reaction efficiency varies between 13% - 19%, depending on collision energy. The only significant triplet channel is NO^+ + triplet ketene, generated predominantly by O^- transfer, with a possible contribution from dissociative charge transfer at high collision energies. NO_2^+ formation (charge transfer) can only occur on the singlet surface, and appears to be mediated by a weakly bound complex at low energies. O transfer ($C_2H_2O^+$) also appears to be dominated by reaction on the singlet surface, but is quite inefficient, suggesting a bottleneck limiting coupling to this product from the singlet reaction coordinate. The dominant channel is O^- transfer, producing NO^+, with roughly equal contributions from reaction on singlet and triplet surfaces. The effects of $C_2H_2^+$ vibration are modest, but mode specific. For all three product channels (i.e., charge, O^-, and O transfer), excitation of the CC stretch fundamental (ν_2) has little effect, $2\cdot\nu_2$ excitation results in ~50% reduction in reactivity, and excitation of the cis-bend overtone ($2\cdot\nu_5$) results in ~50% enhancement. The fact that all channels have similar mode dependence suggests that the rate-limiting step, where

vibrational excitation has its effect, is early on the reaction coordinate, and branching to the individual product channels occurs later.

Introduction

Previous experimental[1,2] and trajectory[3] studies of the reaction of NO_2^+ with C_2H_2 revealed a number of interesting dynamical features. The reaction has two almost isoenergetic channels, O and O^+ transfer to form $NO^+ + C_2H_2O$, and $C_2H_2O^+ + NO$. In both cases, the most stable isomer of $C_2H_2O^{(+)}$ is ketene (H_2CCO). The two channels have nearly identical dependence on NO_2^+ vibrational mode and collision energy (E_{col}), and also very similar product recoil dynamics, indicating that branching (i.e. localization of the charge on one or the other product) occurs as the products separate, well after the rate-limiting step on the reaction coordinate. Despite being exoergic barrierless atom-transfer reactions, the efficiencies are low, suggesting a bottleneck. Reaction is strongly enhanced by NO_2^+ bending vibration, and while the symmetric and asymmetric NO_2^+ stretch modes also enhance reaction, their efficiency is low, despite their stretching of the N-O bond that must break during reaction. Instead, it appears that reaction requires charge transfer (CT) between the reactant moieties as they collide, converting NO_2^+-C_2H_2 (both closed shell singlets) to NO_2-$C_2H_2^+$ (both doublets), where C-O bond formation is facilitated by singlet-coupled unpaired electrons on both reactants.

Figure 5.1 shows a cut through the two lowest energy diabatic surfaces for $(NO_2$-$C_2H_2)^+$ at infinite reactant separation. The two coordinates shown are the NO_2 bend angle (α_{ONO}) and symmetric stretch (r_{NO}), i.e., the two coordinates for $(NO_2$-$C_2H_2)^+$ that change significantly when the charge transfers between the two reactant moieties. Note

that for geometries where the NO_2 moiety is near-linear, the lowest energy electronic configuration corresponds to NO_2^+-C_2H_2, but for geometries where NO_2 is strongly bent, the ground state electronic configuration corresponds to NO_2-$C_2H_2^+$. The NO_2 symmetric stretch has a smaller, but still significant effect on the relative stabilities of the two electronic configurations. As reactants approach, the surface crossing becomes avoided, and the system can adiabatically move between regions of the lowest Born-Oppenheimer surface where the electronic configuration corresponds to $NO_2^+ + C_2H_2$ and to $NO_2 + C_2H_2^+$. The strong reactivity enhancement from bend excitation reflects the fact that bending is the dominant motion driving the closed shell $NO_2^+ + C_2H_2$ reactants toward $NO_2 + C_2H_2^+$, where reactivity of the singlet-coupled biradicals is expected to be high. Another interesting observation was that for NO_2^+ excited with two quanta of bending excitation, the 02^20 state (255 meV) was only ~half as reactive as the 02^00 state (253 meV). Trajectory analysis suggested that reaction requires both transition to the $NO_2 + C_2H_2^+$ configuration, and orientation of the bent NO_2 such that CO bond formation is possible in the short time before NO_2 bending carries the system back into the unreactive $NO_2^+ + C_2H_2$ configuration. The 02^20 state, where the bent NO_2 is rapidly rotating about its long axis, impedes locking into the correct orientation, and thus reduces reactivity.

Here we report a study of the same system, but starting with $NO_2 + C_2H_2^+$ reactants, i.e., with the excited configuration that was identified as highly reactive in the previous work. We have not found any previous study of this reaction. The reaction coordinate is shown in Figure 5.2. In this figure, species and reaction coordinates that are singlets are indicated in blue, triplet species and reaction coordinates are shown in red, and doublet

species are shown in green. The reaction coordinate for the previously studied NO_2^+ + C_2H_2 reaction is the blue (singlet) portion in the lower part of the figure. For collisions of reactants such as NO_2 + $C_2H_2^+$, where each collision partner has one unpaired electron, 25% of collisions will occur with singlet coupling of the unpaired electrons, and 75% of collisions will occur with triplet coupling. In many systems, such triplet-coupled collisions are unreactive or even repulsive because the unpaired electrons are unable to form bonds.[4] One question of interest, therefore, is the extent to which reaction occurs on the triplet surface in this system. Note that for systems like this, lacking heavy atoms with large spin-orbit coupling constants, we expect that the probability for transitions between singlet and triplet surfaces during the collisions should be small. As an example, consider dissociation of NO_2^+ in collisions with rare gas atoms -- collisions which always start on a singlet surface. For Xe, the system is able to access the lowest energy NO^+ + $O(^3P)$ channel, but for Ne, Ar, and even Kr, the singlet-triplet coupling is so weak that only the higher energy NO^+ + O (^1D) channel is observed.[5]

A diagram like Figure 5.2 can only show stationary points and other gross features of the 15-dimensional potential energy surfaces. In particular, it does not show how the NO_2 bend angle affects the energetics of the different surfaces (see Figure 5.1), thus it should be kept in mind that transition of the singlet-coupled NO_2 + $C_2H_2^+$ reactants to the lower regions of the reaction coordinate, corresponding to NO_2^+ + C_2H_2, will be highly dependent on the NO_2 bend angle. Similarly, it is unclear whether or how the $C_2H_2O^+$ + NO (doublet-doublet) products correlate to the singlet and triplet surfaces. The results below answer some of these questions, and provide insight into the dynamics on both

surfaces, including effect of $C_2H_2^+$ bending and stretching excitation. It should also be noted that in addition to the ketene isomer of the $C_2H_2O^{(+)}$ products, there are HCCOH and three-membered ring (oxirene) isomers, which we discussed in studies of the NO_2^+ + C_2H_2 reaction.[1] The HCCOH isomer is considerably higher in energy than ketene, with correspondingly high transition states to reach it, and was not seen even as an intermediate in trajectories at high energies. The oxirene isomer was frequently formed in the trajectories as an intermediate; however, it rapidly rearranged to ketene. In the following, therefore, we focus on the ketene isomer.

Experimental and Computational Methods

$C_2H_2^+$ is produced in its ground state (GS) and with one or two quanta of CC-stretch (ν_2 = 225 meV) by 3+1 REMPI through the corresponding levels of the G $^1\Pi_u$ Rydberg state.[6] To generate ions with two quanta of the cis-bend excited ($2\nu_5$ = 155 meV) we used 2+1 REMPI through a vibronically mixed level of a $^1\Delta_g$ state.[7] State purity measured by photoelectron spectroscopy is essentially 100% for GS and ν_2-excited $C_2H_2^+$, however for $2\nu_5$ preparation, only ~56% of the ions are in the desired state, with 44% in the ground state. Because we measure cross sections for the GS reaction, the cross sections for $2\nu_5$ excitation can be obtained by subtraction, which has been done for all the results below.

The cross section measurements were made in a guided ion beam instrument described in detail previously,[8,9] along with our calibration and data analysis procedures. For these experiments, a 1:6 mixture of C_2H_2 in He was pulsed into the experiment with a piezoelectric pulsed valve, then collimated by a skimmer before passing into the

ionization region. Ionization occurred between a pair of planar electrodes, and the resulting ions were then injected into a quadrupole ion guide, which focused them into a quadrupole mass filter to remove any fragment ions produced in the REMPI process. At the end of the mass filter, a time-of-flight (TOF) gate was used to narrow the kinetic energy spread of the reactant ion beam. The state-, mass-, and energy-selected ions were injected into the first section of the ion guide and passed through a scattering cell containing 0.1 mTorr of NO_2. Product ions, together with unreacted $C_2H_2^+$, are contained within the ion guide and passed into the second, longer guide section for TOF velocity analysis, then are mass analyzed and detected. Products that are backscattered in the laboratory frame are reflected at the entrance of the guide by a positive potential on the injection lens, and are detected at long times, corresponding to apparent low velocities. Ions are counted using a P7882 FAST ComTec multichannel scalar, controlled by a LabView program that cycles through collision energies and masses of interest, and switches the target gas flow between the scattering cell and chamber background. Integral cross sections are calculated from the ratio of reactant and product ion intensities, corrected for ions formed outside the scattering cell, using the calibrated effective length of the scattering cell[8] and pressure measured with a capacitance manometer, which is checked against an ionization gauge.

TOF is used both to measure the energy distribution of the reactant ion beam, and the axial projection of the recoil velocity distribution for the product ions (v_{axial}). The reactant ion velocity distributions at each E_{col} can be fit within experimental error to Gaussians, defining the absolute energy and energy spread (< 150 meV for all E_{col}) of the

beam. TOF data were collected for product ions at a series of collision energies and for reaction of ground state, $2\nu_5$-, and $2\nu_2$-excited $C_2H_2^+$. Several complete sets of cross sections for the four reactant states and three product channels as a function of collision energy were recorded, each taking several days because the ion beam intensity obtainable by REMPI is relatively low (~1800 ions/sec). To avoid systematic errors comparing different vibrational states, the ground state cross sections were collected every day as a check on possible changes in instrument conditions. The cross sections presented below are averages of all the data, and based on the variations from set-to-set, we estimate that the relative error in comparing cross sections for different vibrational states or collision energies is <15%, including statistical and systematic errors. The exception is that for the weak $C_2H_2O^+$ channel, particularly at high E_{col}, the statistical error is larger, and can be judged from the scatter in the data, shown below. We estimate the uncertainty in the absolute cross section to be about 20% due to possible mass-dependent detection efficiency in the final mass spectrometer.

We considered the possibility that the NO_2 in the scattering cell might be contaminated by either NO, or by N_2O_4, which is in equilibrium with NO_2. If either contaminant were present at concentrations greater than a few percent, there would be significant contributions to the NO^+, and possibly NO_2^+ product signals. Mass analyzing the NO_2 is ambiguous because of extensive fragmentation which is quite sensitive to small changes in ionization conditions. The presence of significant NO was ruled out by running a gas-phase IR spectrum of the NO_2 at high enough pressure that the weak symmetric stretch transition for NO_2 was nearly saturated. No signal was seen for the

much stronger NO stretch transition. The equilibrium concentration of N_2O_4 at the 10^{-4} Torr pressure in our scattering cell is negligible[10], but we had some concern that the time constant for reaching equilibrium[11] might leave some undissociated N_2O_4. Our approach to generating a stable reactant flow into the scattering cell is to leak gas into the instrument from a small Tedlar gas sampling bag, such that the pressure feeding the leak valve is constant (barring thunderstorms) at the lab barometric pressure (N_2O_4 equilibrium concentration ~13%). We also measured cross sections at several E_{col} values switching between the bag reservoir, and a large volume, low pressure (~50 Torr) NO_2 reservoir, where the equilibrium N_2O_4 concentration is less than 1%. No significant changes in any of the product cross sections were observed, thus we conclude that the gas in the scattering cell has negligible concentrations of both NO and N_2O_4 contaminants.

To construct the reaction coordinate shown in Figure 5.2, we used experimental energies for reactants and products,[12-16] combined with published[1] *ab initio* results for the singlet complexes and transition states, and new results for the triplet intermediates, all calculated at the B3LYP/6-311++G** level of theory using GAUSSIAN 03.[17] The vibrational frequencies and zero point energies were scaled by 0.9613 and 0.9804 respectively,[18] and the computational energies were referenced to the experimental reactant energies. As a check on the computational accuracy, the product channel energies were also calculated at the B3LYP/6-311++G** level of theory, and were all within 0.29 eV (and mostly within 0.2 eV) of the experimental values shown in the figure.

Quasi-classical, direct dynamics trajectories were used to examine coupling of NO_2^+ vibrations to the dissociation coordinate of a $(C_2H_2\text{-}NO_2)^+$ complex. The quasi-classical initial vibrational state is simulated by giving the reactant atoms displacements from equilibrium and kinetic energies appropriate to the desired initial rovibrational state, with random phases for the different modes, and random initial orientations. The VENUS program of Hase and co-workers[19] was used to calculate the quasi-classical initial conditions, and direct dynamics trajectories were integrated using the updating Hessian method of Schlegel and co-workers,[20] implemented in GAUSSIAN03.[17]

Results and Discussion

Computational Results

The computational results are summarized in the reaction coordinate diagram in Figure 5.2. Note that we also optimized the structure of the triplet complex at the PBE1PBE/6-311++G** level, resulting in a similar geometry to that found using B3LYP/6-311++G**, but with a 0.3 Å shorter inter-moiety separation. The energies of both geometries were calculated at the QCISD/6-311++G** level, and the PBE1PBE structure was found to be ~0.6 eV more stable than that from the B3LYP optimization (shown in the figure). What is clear from this result is that there is at least one stable structure on the triplet surface that is ~1 eV below reactants. In this complex, one of the N-O bonds is stretched and directed towards a carbon center, which appears to be at least partly rehybridized (bent) suggesting incipient C-O bond formation. This conclusion is supported by analysis of the PBE1PBE/6-311++G** molecular orbitals, where the HOMO-3 orbital has significant sigma-like electron density between the closest C-O pair.

From the reactant-like structure of this complex, there is no reason to expect a barrier separating it from reactants. It is also not obvious why the transition state separating this complex from products (i.e., for O^-/O transfer) should be particularly tight or high in energy. In that case, we might expect that reaction on the triplet surface should be reasonably efficient, producing either NO^+ + triplet ketene or $C_2H_2O^+$ + NO. Unfortunately, we were unable to characterize this transition state computationally, because of SCF convergence problems.

Experimental Results

Product ions are observed at masses 30 (NO^+), 42 ($C_2H_2O^+$), and 46 (NO_2^+), with possible contributions from the following reactions:

$C_2H_2^+ + NO_2$

$\rightarrow NO^+ (^1\Sigma^+) +$ singlet C_2H_2O	(O^- transfer)	ΔH_{rxn} = -4.81 eV
$\rightarrow NO^+ (^1\Sigma^+) +$ triplet C_2H_2O	(O^- transfer)	ΔH_{rxn} = -1.23 eV[21,22]
$\rightarrow C_2H_2O^+ + NO$	(O transfer)	ΔH_{rxn} = -4.45 eV
$\rightarrow C_2H_2 + NO_2^+ (^1\Sigma_g^+)$	(charge transfer - CT)	ΔH_{rxn} = -1.81 eV
$\rightarrow C_2H_2 + NO_2^+ (a^3B_2)$	(charge transfer - CT)	ΔH_{rxn} = +1.74 eV
$\rightarrow C_2H_2 + O (^3P) + NO^+$	(dissociative CT)	ΔH_{rxn} = +1.04 eV
$\rightarrow C_2H_2 + O (^1D) + NO^+$	(dissociative CT)	ΔH_{rxn} = +3.01 eV

where the energies are experimental,[12-16] and refer to the most stable ketene structure of $C_2H_2O^{(+)}$. The integral cross sections for production of NO^+, $C_2H_2O^+$, and NO_2^+ in reaction of ground state $C_2H_2^+$ with NO_2 are shown in the top frame of Figure 5.3 over the center-of-mass collisions energy range from 0.16 to 3.10 eV. For comparison, the

lower frame of the figure gives the previously reported[1] cross sections for NO^+ and $C_2H_2O^+$ production in reaction of ground state NO_2^+ with C_2H_2. The insets to each frame of the figure compare the total reaction cross section (σ_{total}) with the collision cross section ($\sigma_{collision}$), taken as the rotationally averaged ion-dipole capture cross section (calculated as in Troe et al.[23]), except at our highest energy point, where the slightly larger orientation-averaged hard sphere cross section (calculated from the molecular geometries and tabulated atomic radii[10]) is used. In the top frame we also plot 0.25 times the collision cross section, to indicate the magnitude of the cross section for collision with singlet coupling.

Comparing the total reaction cross section for ground state $C_2H_2^+$ with the $\sigma_{collision}$, we see that the reaction efficiency ($\sigma_{total}/\sigma_{collision}$) ranges from ~38 % at low E_{col} to ~46% at high E_{col}. Because σ_{total} exceeds the singlet collision cross section, there clearly is significant reaction on the triplet surface. The magnitude of the total triplet reaction cross section, $\sigma_{triplet} = \sigma_{total} - 0.25 \cdot \sigma_{collision}$, ranges from ~10 $Å^2$ at E_{col} = 0.15 eV to ~3 $Å^2$ at E_{col} = 3 eV.

The situation for reaction in the $NO_2^+ + C_2H_2$ charge state, which can only access the singlet surface, is quite different (Figure 5.3, lower frame). Ground state reaction efficiency varies from 2% at low E_{col} to 27% at high E_{col}, with a minimum near 0.5 eV of only 0.5%. As noted in the Introduction, reaction in the $NO_2^+ + C_2H_2$ system appears to occur only if the charge transfers to the C_2H_2 moiety during collision in an orientation that allows CO bond formation. For the present work, the reactants start in the $C_2H_2^+ + NO_2$ charge state, thus substantially more efficient reaction is not surprising.

The O transfer reaction ($C_2H_2O^+$ production) is quite exoergic, and because it could potentially occur on both the singlet and triplet surfaces, one might expect it to be a major channel. The non-zero cross section for $C_2H_2O^+$ at low E_{col} implies that there is a barrierless route to this product; nonetheless, the efficiency ranges from only ~2% at low E_{col} to <1% at high E_{col}. Note that even if this channel went entirely by reaction on the triplet surface, it would account for no more than ~15% of $\sigma_{triplet}$.

The dominant channel over the entire E_{col} range is O^- transfer, producing NO^+ in conjunction with some combination of singlet and triplet ketene as the neutral product. Because this is the only exoergic triplet channel besides $C_2H_2O^+$ formation, the triplet component of O^- transfer must be significant, accounting for at least 85% of $\sigma_{triplet}$ at low E_{col}. Despite having quite similar energetics, the relative branching between O and O^- transfer (NO^+ and $C_2H_2O^+$ products) ranges from ~10:1 at low E_{col} to ~25:1 at high E_{col}. The branching to $C_2H_2O^+$ + NO products is also small for NO_2^+ + C_2H_2 reactants, with a similar E_{col} dependence to that seen here. Clearly, there is a severe bottleneck that inhibits this $C_2H_2O^+$ formation.

CT (NO_2^+ production) is a major channel at all energies, which must result entirely from singlet collisions below the opening of the NO_2^+ (a^3B_2) channel at 1.74 eV. Because this state predissociates (see below), singlet collisions must actually generate most, if not all, of the observed NO_2^+ signal even at high energies. CT is expected to be relatively insensitive to reactant orientation, presumably contributing to the high reaction efficiency for this system, compared to the NO_2^+ + C_2H_2 system where only strongly orientation-dependent atom transfer reactions are seen.[1]

At $E_{col} \geq 2$ eV, the cross section for the NO^+ channel increases slightly, which may indicate a small contribution from dissociative CT, generating $NO^+ + O\ (^3P)$ in this energy range. For reasons discussed in the Introduction, it is unlikely that singlet NO_2^+ could access this triplet dissociation channel, thus any dissociative CT would have to occur in triplet-coupled collisions. The process could be concerted, directly accessing the dissociation channel (threshold $E_0 = 1.04$ eV), or sequential, by pre-dissociation of NO_2^+ (a^3B_2) which lies[24] ~0.7 eV above the $O\ (^3P) + NO^+$ limit ($E_0 = 1.74$ eV). Shibuya *et al.*[16] measured the predissociation lifetime of NO_2^+ (a^3B_2), and found that for the (000) level, the lifetime is about 1.3 msec, decreasing into the sub-100 μsec range with even low levels of vibrational excitation. The flight time for any NO_2^+ (a^3B_2) produced in our experiment (see v_{axial} distributions below) would be in the 200 - 500 μsec range, thus we expect that nearly all of any NO_2^+ (a^3B_2) produced in high energy collisions would dissociate and be detected as NO^+. If we take the small increase in NO^+ at high E_{col} as an indicator of dissociative CT, this is a minor channel (2 - 3 $Å^2$) over our E_{col} range.

Charge Transfer Dynamics

At low E_{col}, CT can only happen on the singlet surface, and the cross section is small enough (~55% - 65% of the singlet $\sigma_{collision}$) that it is not obvious what the contributions from long-range and short-range mechanisms might be. Figure 5.4 shows the laboratory frame axial projections of the recoil velocity distributions for the NO_2^+ CT product, where each distribution is scaled so that its integral is proportional to the integral cross section at that energy. Experimental data is shown as points, and the smooth curves are simulations of the experiments, described below. The heavy vertical line in each frame

indicates the laboratory velocity of the center-of-mass frame ($<V_{cm}>$), averaged over the collision energy distribution. Axial velocity (v_{axial}) distributions are simply the projections of the full velocity distributions on the ion guide axis. Because the experiment has axial symmetry, the raw distributions directly reveal the qualitative dynamics. For example, ions that are faster (slower) than V_{cm} correspond to forward (backward) scattering, and reactions mediated by a long-lived complex must result in v_{axial} distributions that are symmetric about V_{cm}.

More quantitative interpretation relies on simulating the distributions,[1,25] in this case using a recoil velocity model combining angular distributions based on the osculating complex model,[26] with Gaussian recoil energy distributions defined in terms of the available energy. We do not attempt to fit the distributions below ~500 m/sec, because this velocity range is strongly perturbed by stray fields, and also by contributions from ions that are back-scattered in the lab frame, and detected after reflection from the ion lens at the entrance to the ion guide. The osculating complex model assumes that there is a preferred recoil angle (θ_{peak}), but that the angular distribution is broadened by rotation of the collision complex prior to breakup to products. The broadening is described by the parameter $\tau_{ratio} = \tau_{rotation}/\tau_{collision}$, where $\tau_{rotation}$ and $\tau_{collision}$ are the rotational period of the collision complex, and its lifetime, respectively. $\tau_{rotation}$ can be estimated from the moment of inertia of the complex and the collisional angular momentum. Table 5.1 summarizes the best fit parameters for the v_{axial} distributions from reaction of ground state $C_2H_2^+$, as well as the resulting average recoil energy, $<E_{recoil}>$, and collision times, $\tau_{collision}$. The table also gives $\tau_{fly\text{-}by}$, which is intended as a measure of the collision time

scale in the limit of no complex mediation ($\tau_{fly\text{-}by}$ = time for reactants to fly past each other, through a relative distance of 5 Å).

For CT at E_{col} = 0.16 eV, the recoil velocity distribution appears to be forward-backward symmetric about V_{cm}, which in this model would require that $\tau_{collision}$ exceed ~1 psec. In addition, the recoil energy distribution is broad and peaks at zero energy, with $\langle E_{recoil} \rangle \approx 0.08 \langle E_{avail} \rangle$, which is only ~20% more than would result from equipartitioning E_{avail} (~2 eV) into the energetically accessible degrees of freedom of the products (all but CC and CH stretch modes of C_2H_2). Both factors suggest a complex-mediated mechanism, and in this energy range, where only singlet CT is possible, there are two complexes (Figure 5.2) that might be involved. The 5-membered ring complex can be eliminated because RRKM analysis of its breakup shows that branching is almost entirely to $(NO + C_2H_2O)^+$ products, with essentially no branching back to $NO_2^+ + C_2H_2$.[1] The complex labeled "Singlet Precursor Complex" is essentially an electrostatic complex of the CT products, calculated to decay almost exclusively to CT products, however, its lifetime would be negligible if the available energy is assumed to be randomized.

Because of the large geometry change during ionization of NO_2, much of the 1.81 eV released by CT as the complex forms will tend to go initially into NO_2^+ bending and symmetric stretching vibration. In a loosely-bound complex like this, coupling of such high frequency molecular modes to the low frequency modes of the complex may be weak,[27-31] thus much of the available energy may be tied up in modes that are not coupled to the dissociation coordinate. For reference, the strong vibrational mode effects seen for

reaction of NO_2^+ with C_2H_2, which appears to be mediated by this same complex at low E_{col}, also suggests that NO_2^+ vibration is not strongly coupled in the complex.[1]

To test the possibility that such a weakly bound $(NO_2\text{-}C_2H_2)^+$ complex with ~1.8 eV of vibrational energy in NO_2^+ might form and survive long enough to be dynamically significant, we ran a small set of quasi-classical trajectory calculations with random reactant orientations. The method used,[19,20] runs trajectories on the lowest energy Born Oppenheimer surface, thus the trajectories were started as $C_2H_2 + NO_2^+$ with E_{col} = 0.16 eV, and 10 quanta in the NO_2^+ bend, and 2 quanta in the NO_2^+ symmetric stretch. In essence, this starting condition simulates what might happen if resonant long range CT (see below) converts $C_2H_2^+ + NO_2$ to $C_2H_2 + NO_2^+$ in the entrance channel. Forces were calculated at the PBE1PBE/6-311G** level of theory, previously shown[3] to be reasonably accurate for this system, and the trajectories were terminated when the C_2H_2 and NO_2 moieties separated, or after ~1.5 psec. Of the trajectories that formed complexes, the survival time ranged from ~500 fsec to 1.5 psec. During this survival time, the energy initially put in NO_2^+ vibration is approximately uncoupled, as judged by the range of angles explored by α_{ONO} (-140° to 140°). When the NO_2 vibrational energy finally couples, dissociation occurs immediately. Note that for this level of bending excitation, the system vibrates back and forth between regions on the surface corresponding to $C_2H_2^+\text{-}NO_2$ and $C_2H_2\text{-}NO_2^+$ (Figure 5.1). This simulation should not be taken as definitive, because vibration is treated classically. (One might also think that multi-reference wave functions would be needed, however, CASSCF calculations indicated[3] that the Hartree-Fock configuration is sufficient (coefficient >0.9) in all

geometries explored by the trajectories) Because classical vibrational energy is not quantized, we expect that quantization would result in slower vibrational randomization, suggesting that the trajectory calculations may underestimate the complex lifetime. We conclude, therefore, that it is at least plausible that a weakly coupled complex may mediate reaction at the lowest E_{col}.

When E_{col} increases to 0.44 eV, the distribution becomes markedly backward peaked, consistent with mediation by a weakly bound complex, such that $\tau_{collision}$ rapidly becomes short compared to $\tau_{rotation}$. This trend continues with increasing E_{col}, and in addition, the v_{axial} distributions narrow, indicating less energy randomization, also consistent with direct, shorter time scale collision. At E_{col} = 3.1 eV, the distribution is sharply backward peaked near zero lab velocity, and there is little intensity in the forward hemisphere (i.e., $v_{axial} > V_{cm}$). Near-zero product ion lab velocity is a signature expected for long-range CT, where the electron hops as the reactants fly past each other in large impact parameter (b) collisions, resulting in little momentum transfer.

Long range CT is essentially an electronic transition, where the orbitals involved happen to be on different molecules. Since forces are weak at long range, E_{recoil} must approximately equal E_{col}, thus the reactant and product states involved in the transition must be nearly resonant. In addition, for an electronic transition, we expect the probability to depend on the Franck-Condon (FC) factors, i.e., the product of the FC factors for $C_2H_2^+ \rightarrow C_2H_2$ and for $NO_2 \rightarrow NO_2^+$. The geometries of $C_2H_2^+$ and C_2H_2 are quite similar, thus the FC factors for $C_2H_2^+$ neutralization are expected to be nearly diagonal, i.e., favoring no change in vibrational state. For NO_2, the bend angle changes

from 134.1° to 180° upon ionization, and there is a ~0.08Å change in the NO bond length as well. Therefore, in ionization of ground state NO_2, the highest FC factors will be for final states combining low levels of symmetric stretch and high levels of bend excitation. This behavior is clearly shown in the high resolution photoelectron spectrum of NO_2.[32] The adiabatic ionization energy of NO_2 is estimated to be < 9.6 eV, however, the spectrum consists of a broad band peaking at 11.22 eV, corresponding to ~1.62 eV of NO_2^+ vibrational energy. High resolution spectra reveal that this broad band is composed of several overlapping progressions in the NO_2^+ bend mode built on a few levels of the symmetric stretch mode. The exoergicity of CT is 1.81 eV - well within the broad envelope of FC-active final states - thus this system satisfies the requirement for long range CT of having resonant final states with good FC factors.

One might also expect CT to occur in smaller impact parameter collisions, where there would be substantial momentum transfer to the NO_2^+ product, resulting in forward-scattered signal ($v_{axial} > V_{cm}$). There is some forward-scattered signal for low E_{col}, but by 3.1 eV there is essentially no signal outside the back-scattered peak, indicating that small b collisions do not contribute to the CT channel. Competition with singlet dissociative CT (E_0 = 3.01 eV) is probably not a major loss mechanism, because it would require partitioning essentially all the available energy into NO_2^+ internal excitation -- unlikely for collisions of two polyatomic species. As noted, there may be some triplet dissociative CT at high energies, however, opening a channel on the triplet surface cannot explain the absence of CT in small b singlet collisions. Instead, we propose that small b singlet

collisions result in O/O^- transfer ($C_2H_2O^+/NO^+$ production), or no reaction, and this idea is supported by the v_{axial} distributions for those channels.

CT on the triplet surface is 1.74 eV endoergic, thus this channel could potentially contribute to the v_{axial} distribution for NO_2^+ at E_{col}=3.1 eV, but only that fraction of the NO_2^+ (a^3B_2) produced with vibrational energy ≤ ~80 meV, where the predissociation lifetime would allow it to survive. For reference, equipartition among the accessible degrees of freedom (all but the CC and CH stretches of C_2H_2) would put ~0.46 eV of vibrational energy into NO_2^+ (a^3B_2).

O Transfer Dynamics: $C_2H_2O^+$ Production

O transfer is a minor channel, despite being only slightly less exoergic than the O^- transfer (NO^+) channel, which dominates at all collision energies. Consider formation of $C_2H_2O^+$ on the singlet surface (Figure 5.2). The O/O^- transfer channels differ only in the final location of the charge, which is delocalized during the intimate phase of the collision (e.g. in structures like the 5-membered ring complex or the TS separating it from products). Thus, one might expect that branching would be controlled by the density of states in the two product channels, and the $NO^+/C_2H_2O^+$ ratio would be close to 1. In principle, both NO^+ and $C_2H_2O^+$ can also form in triplet collisions, and in this case, production of $C_2H_2O^+$ + NO is considerably more exoergic than NO^+ + triplet ketene, thus we might expect the $NO^+/C_2H_2O^+$ ratio to be < 1. For the NO_2^+ + C_2H_2 reactants, which only explore the singlet surface, the $NO^+/C_2H_2O^+$ ratio is ~4. For $C_2H_2^+$ + NO_2, which can access both singlet and triplet reaction coordinates, the ratio is 10 to 25, depending on E_{col}. The implication is that at some point along the reaction

coordinate, there must be a significant bottleneck that inhibits $C_2H_2O^+$ formation. An important point in this regard is that the $NO^+ + C_2H_2O$ and $C_2H_2O^+ + NO$ channels for the $NO_2^+ + C_2H_2$ reaction, which accesses only the singlet surface, have essentially identical dependence on E_{col} and vibrational mode. This similarity implies that the branching between the two product charge states occurs late in the reaction, after the rate-limiting step that establishes the dependence on mode and E_{col}. Furthermore, the two channels also have essentially identical recoil dynamics (i.e., are fit using the same simulation parameters), providing additional evidence that they are coupled until late in the collision process.

Figure 5.5 shows v_{axial} distributions for the $C_2H_2O^+$ channel. The distributions at low E_{col} are forward-backward symmetric, changing to forward peaked at high E_{col}. Unlike CT, the transition from symmetric to asymmetric distributions occurs slowly, with the distribution at 0.44 eV remaining symmetric within experimental error (the apparent increase at low lab velocity reflects pileup of reflected back-scattered ions). This behavior suggests that O-transfer may be mediated by a collision complex that is more stable than the "singlet precursor complex" (Figure 5.2), and the logical candidate is the five-membered ring complex. Even though this complex is substantially more stable than the singlet precursor complex, the strong bonding also implies that all forms of energy are coupled, and thus the lifetime would still be expected to drop rapidly with increasing E_{col}, consistent with the transition to asymmetric v_{axial} distributions for $E_{col} \geq 1$ eV.

At high E_{col} the distributions are forward-peaked, but remain quite broad, extending well into the backward hemisphere. Reaction is clearly direct in this energy range, and

the angular distributions (and resulting v_{axial} distribution) probably depend mostly on the impact parameter, with the smallest impact parameters leading to backscattering, and larger impact parameters leading to forward-scattered $C_2H_2O^+$. For the highest E_{col} (Figure 5.5) the product ion velocity predicted by the spectator-stripping model is indicated by a vertical dark red line.[33] Clearly, while the experimental distribution is forward-peaked, it is far from the spectator limit, indicating that intimate collisions with substantial momentum transfer are required to drive the system through the rather severe bottleneck that makes this channel so inefficient.

Another interesting point is that the v_{axial} distributions for O transfer, and their E_{col} dependence, are nearly identical to those recorded for the $C_2H_2O^+$ channel from reaction of NO_2^+ + C_2H_2 (O^+ transfer in that case), with the exception that the definition of forward and backward are opposite for O and O^+ transfer. In that system, reaction occurs only on the singlet surface, thus the similarity tends to suggest that the O-transfer reaction here is also predominantly on the singlet surface. Note that this cross section is small enough that even if it went exclusively on the triplet surface, this would not account for the inferred triplet contribution to σ_{total}.

O^- Transfer Dynamics: NO^+ Production

NO^+ production is the dominant channel at all energies, and as noted above, must occur in both singlet and triplet collisions at low E_{col}, to account for the magnitude of σ_{total}. At low E_{col}, the triplet can only yield NO^+ + triplet ketene, but at high E_{col} there may also be a small contribution from dissociative triplet CT. The v_{axial} distributions for the NO^+ product, which are distinctly different from those for NO_2^+ and $C_2H_2O^+$, are

shown in Figure 5.6, along with simulation-based fits. They are dominated by a narrow spike at near-zero lab velocity, with a broad component or tail extending well into the forward direction.

To separate the contributions from triplet and singlet reactions, we begin by noting that the recoil behavior for the following reactions are very similar over the entire range of E_{col}:

$$C_2H_2^+ + NO_2 \rightarrow C_2H_2O^+ + NO$$

$$NO_2^+ + C_2H_2 \rightarrow C_2H_2O^+ + NO$$

$$\rightarrow NO^+ + C_2H_2O.$$

Since the latter two only involve the singlet surface, the similarity suggests that the singlet reaction probably dominates the former as well. Because the NO^+ and $C_2H_2O^+$ channels in the $NO_2^+ + C_2H_2$ reaction have identical dynamics, i.e., can be fit using a common set of simulation parameters, it is interesting to see if the NO^+ and $C_2H_2O^+$ channels in the $C_2H_2^+ + NO_2$ system also can be fit with a single set of parameters.

Accordingly, the fits to the NO^+ data shown in Figure 5.6 use the same simulation parameters as were used to fit the $C_2H_2O^+$ channel (Figure 5.5). Clearly the broad component of the NO^+ recoil behavior is fit well assuming recoil dynamics identical to those for the $C_2H_2O^+$ channel. Due to kinematics, a significant fraction of this broad simulated v_{axial} distribution is scattered to negative lab velocities. In the experiment, such ions would be reflected and detected at long times, and thus would contribute to the apparent low velocity spike. The intensity of the spike is, however, considerably greater than the negative portion of the broad component, indicating an additional component of

slow or back-scattered ions contributing to the spike. Given that the broad component is dynamically similar to the (singlet) reactions in $NO_2^+ + C_2H_2$, it is tempting to attribute the broad and spike components to singlet and triplet reaction, respectively.

To separate the total NO^+ intensity into broad and "spike" components, we make the following assumptions: Intensity of broad component = integral of the simulation/fit curve. Intensity of spike component = total integrated intensity - intensity of broad component. This separation into singlet and triplet contributions is more than a little *ad hoc*, nonetheless, the result is quite interesting. The top frame of Figure 5.7 compares the singlet collision cross section ($0.25 \times \sigma_{collision}$) with the sum of the cross sections for NO_2^+, $C_2H_2O^+$, and the broad NO^+ component, i.e., the signal we attribute to reactions on the singlet surface. The sum matches the singlet collision cross section almost perfectly, thus if this analysis is correct, reaction on the singlet surface occurs with near unit efficiency. Singlet collisions occurring in geometries allowing C-O bond formation presumably result in NO^+ or $C_2H_2O^+$ products, and the balance result in CT.

In this scenario, the NO^+ formed on the triplet surface must be scattered either at near zero lab velocity, or actually back-scattered in the lab, where it contributes to the low v_{axial} spike. The former would correspond to spectator stripping, and the latter would be a stripping-like process with repulsion between the recoiling products. In either case, the recoil behavior suggests that at all E_{col}, reaction on the triplet surface is direct (not involving any long-lived complex), and occurs primarily at large impact parameters. This conclusion is consistent with the reaction coordinate in Figure 5.2, which has no strongly bound triplet complexes. The bottom frame of Figure 5.7 compares the singlet

and triplet contributions to the NO^+ cross section (based on the above assumptions), and also the triplet collision cross section ($0.75 \times \sigma_{collision}$). The triplet reaction shows no sign of an energetic barrier to reaction at low E_{col}, however, it is only ~15% of the triplet collision cross section, suggesting that there is a bottleneck to reaction on the triplet surface. Low efficiency is, perhaps, unsurprising given that the triplet-coupled unpaired electrons on the two reactants are not able to directly form a C-O bond, which is required for either of the products that are energetically accessible over most of the E_{col} range. Furthermore, it is likely that the triplet reaction is strongly orientation-dependent, as was seen in the O/O^+ transfer reactions for $NO_2^+ + C_2H_2$.

Vibrational Effects

Figure 5.8 shows the dependence of each channel on the initially excited $C_2H_2^+$ vibrational mode. The vibrational effects on the three channels are qualitatively similar, and other than weakening at low energies, are not strongly dependent on E_{col}. For all channels, excitation of the CC stretch overtone, $2\nu_2$, results in a significant (~40-50%) reduction in reactivity, while one quantum of CC stretch excitation has little effect. In contrast, excitation of two quanta of bend, $2\nu_5$, results in significant (~50%) enhancements for all three channels. At low E_{col}, the suppressing effect of $2\nu_2$ excitation (~450 meV) is similar to the effect of adding the same amount of E_{col}, which might tend to suggest that this is just an energy effect. Note, however, that the suppression from E_{col} in this energy range is largely from the reduction in capture cross section, and additional vibrational energy would not affect capture. At high E_{col}, all three channels are only weakly dependent on E_{col}, but still suppressed by $2\nu_2$ excitation and enhanced by $2\nu_5$

excitation. Clearly, the effects of collision energy, bending, and CC stretching are all distinct.

One question is why the vibrational effects appear weaker at low E_{col}, even though this is the energy range where vibration makes its largest contribution to the available energy. This is also the range where the v_{axial} distributions suggest the possibility of mediation by a complex might be important, thus we suggest that the weakening in the vibrational effects may reflect a tendency to partially scramble the initial vibrational mode, prior to the rate-limiting step on the reaction coordinate. This could only occur in a weakly bound precursor complex of the type discussed above in conjunction with the CT channel. If there is some scrambling of $C_2H_2^+$ vibrations in such a complex, we would expect this to shorten the complex lifetime, and thereby hasten the transition from complex-mediated to direct scattering. The v_{axial} distributions are, therefore, also a sensitive test of such behavior, and Figure 5.9 compares the distributions for the CT channel from reaction of different $C_2H_2^+$ initial states, at our lowest E_{col} where such a weakly bound complex appears to have a significant lifetime. At this low energy V_{CM} is so slow that it would be difficult to observe a shift from symmetric to asymmetric distributions, however it does appear that $C_2H_2^+$ vibrational excitation narrows the distributions significantly. Given that the distributions narrow as reaction becomes direct at higher E_{col}, this narrowing is consistent with a transition to more direct dynamics.

The fact that all three channels have similar dependence on $C_2H_2^+$ vibrational mode suggests that they may be coupled, possibly via long range CT in the entrance channel to the collision. It is not clear why such entrance channel CT might enhance reaction, but

possibly the accompanying excitation of NO_2 bending is necessary to allow the reactants to access the ground state singlet reaction coordinate. As discussed above, long range CT requires a final state or states that are close in energy to, and have good FC factors connecting them to the initial state. In that case, the vibrational effects might be attributable to the fact that the vibrationally excited initial states will tend to couple withdifferent final states. It is difficult to access this scenario quantitatively for several reasons. While the geometry does not change much in the transition from $C_2H_2^+$ to C_2H_2, the vibrational frequencies are quite different (ν_2 stiffens by ~18 meV, while ν_5 softens by 28 meV).[34,35] When combined with the high density of final states that are FC active in ground state $NO_2 \rightarrow NO_2^+$, it becomes essentially impossible to sort the coupling of the various initial states to possible near-resonant final states.

Conclusions

By taking advantage of the distinct recoil behavior of reaction on the triplet and singlet surfaces, we have been able to separate the contributions of each to the observed products. The boxes in Figure 5.2 containing percentages show the contribution of each pathway to the total reaction cross section at E_{col} = 0.44 eV.

Singlet reaction efficiency is essentially unity, and all three singlet channels (CT, O^- and O transfer) are mediated by complexes at low energies, changing to direct mechanisms at high energies. The singlet CT reaction is facile, and at high E_{col} appears to result mostly from large impact parameter collisions in orientations where C-O bond formation is not possible. The CT efficiency reflects the fact that there is good Franck-Condon overlap between the initial states, and near-resonant final states in which NO_2^+

has ~1.8 eV of energy in its bend and symmetric stretch modes. O^- transfer is also efficient on the singlet surface, reflecting the presence of singlet coupled unpaired electrons on the two reactants, which readily form a new bond. Somewhat surprisingly, the O transfer reaction is quite inefficient, despite evidence suggesting that O^- and O transfer are coupled throughout most of the reaction, and diverge only as products separate. Though there is no energetic barrier to O transfer, there is apparently a bottleneck that severely inhibits separation to $C_2H_2O^+$ products. Similar behavior is seen for the analogous reactions starting in the $NO_2^+ + C_2H_2$ charge state.

The triplet reaction only has significant branching to NO^+ + triplet ketene, and the mechanism is direct at all energies, reflecting the absence of deep wells on the triplet potential surface. This reaction is only about 15% efficient, despite being exoergic, and having no energetic barriers in excess of the reactant energy, as shown by the collision energy dependence.

All three product channels (charge, O^-, and O transfer) are modestly inhibited by $C_2H_2^+$ CC stretch excitation, and enhanced by excitation of the cis-bend overtone. The fact that the three channels have identical dependence on vibrational mode suggests that they share a common rate-limiting step, which must come early on the reaction coordinate, before the initial vibrational excitation is scrambled by strong collisional interactions.

References

1. J. M. Boyle, B. W. Uselman, J. Liu, and S. L. Anderson, J. Chem. Phys 128, 114304 (2008).

2. F. Bernardi, F. Cacace, G. de Petris, F. Pepi, I. Rossi, and A. Troiani, Chemistry European Journal 6, 537 (2000).

3. J. M. Boyle, J. Liu, and S. L. Anderson, J. Phys. Chem. A 113, 3911 (2009).

4. P. B. Armentrout and J. Simons, J. Am. Chem. Soc. 114, 8627 (1992).

5. J. Liu, B. W. Uselman, J. M. Boyle, and S. L. Anderson, Journal of Chemical Physics 125, 133115/1 (2006).

6. T. M. Orlando, S. L. Anderson, J. R. Appling, and M. G. White, J. Chem. Phys. 87, 852 (1987).

7. M. N. Ashfold, B. Tutcher, B. Yang, Z. Jin, and S. L. Anderson, J. Chem. Phys. 87, 5105 (1987).

8. Y.-H. Chiu, H. Fu, J.-T. Huang, and S. L. Anderson, J. Chem. Phys. 102, 1188 (1995).

9. J. Liu, H.-T. Kim, and S. L. Anderson, J. Chem. Phys. 114, 9797 (2001).

10. *CRC Handbook of Chemistry and Physics*, edited by R. C. Weast, M. Astle, J., and W. H. Beyer (CRC Press, Boca Raton, 1985).

11. F. R. Ornellas, S. M. Resendeb, F. B. C. Machado, and O. Roberto-Neto, J. Chem. Phys 118, 6 (2002).

12. J. Malcolm W. Chase, *NIST-JANAF thermochemical tables*, 4th ed. (American Chemical Society, and American Institute of Physics for the National Institute of Standards and Technology, 1998).

13. K. P. Huber and G. Herzberg, *Molecular Spectra and Molecular Structure IV. Constants of Diatomic Molecules* (Van Nostrand Reinhold, New York, 1979).

14. H. Y. Afeefy, J. F. Liebman, and S. E. Stein, in *NIST Chemistry WebBook, NIST Standard Reference Database Number 69*, edited by W. G. Mallard and P. J. Linstrom (National Institute of Standards and Technology (http://webbook.nist.gov), Gaithersburg MD, 2000).

15. S. G. Lias, J. E. Bartmess, J. F. Liebman, J. L. Holmes, R. D. Levin, and W. G. Mallard, in *NIST Chemistry WebBook, NIST Standard Reference Database Number 69*, edited by W. G. Mallard and P. J. Linstrom (National Institute of Standards and Technology, Gaithersburg MD 20899 (http://webbook.nist.gov). 2000).

16. K. Shibuya, S. Suzuki, T. Imamura, and I. Koyano, J. Phys. Chem. A 101, 685 (1997).

17. M. J. Frisch, G. W. Trucks, H. B. Schlegel, G. E. Scuseria, M. A. Robb, J. R. Cheeseman, J. J. A. Montgomery, T. Vreven, K. N. Kudin, J. C. Burant, J. M. Millam, S. S. Iyengar, J. Tomasi, V. Barone, B. Mennucci, M. Cossi, G. Scalmani, N. Rega, G. A. Petersson, H. Nakatsuji, M. Hada, M. Ehara, K. Toyota, R. Fukuda, J. Hasegawa, M. Ishida, T. Nakajima, Y. Honda, O. Kitao, H. Nakai, M. Klene, X. Li, J. E. Knox, H. P. Hratchian, J. B. Cross, C. Adamo, J. Jaramillo, R. Gomperts, R. E. Stratmann, O. Yazyev, A. J. Austin, R. Cammi, C. Pomelli, J. W. Ochterski, P. Y. Ayala, K. Morokuma, G. A. Voth, P. Salvador, J. J. Dannenberg, V. G. Zakrzewski, S. Dapprich, A. D. Daniels, M. C. Strain, O. Farkas, D. K. Malick, A. D. Rabuck, K. Raghavachari, J. B. Foresman, J. V. Ortiz, Q. Cui, A. G. Baboul, S. Clifford, J. Cioslowski, B. B. Stefanov, G. Liu, A. Liashenko, P. Piskorz, I. Komaromi, R. L. Martin, D. J. Fox, T. Keith, M. A. Al-Laham, C. Y. Peng, A. Nanayakkara, M. Challacombe, P. M. W. Gill, B. Johnson, W. Chen, M. W. Wong, C. Gonzalez, and J. A. Pople, (Gaussian, Inc., Pittsburgh PA, 2003).

18. J. B. Foresman and A. Frisch, *Exploring Chemistry with Electronic Structure Methods*, 2 ed. (Gaussian, Pittsburgh, 1993).

19. W. L. Hase, K. Bolton, P. de Sainte Claire, R. J. Duchovic, X. Hu, A. Komornicki, G. Li, K. Lim, D. Lu, G. H. Peslherbe, K. Song, K. N. Swamy, S. R. Vande Linde, A. Varandas, H. Wang, and R. J. Wolf, VENUS99: A general chemical dynamics computer program (1999).

20. V. Bakken, J. M. Millam, and H. B. Schlegel, J. Chem. Phys. 111, 8773 (1999).

21. M. Ahmed, D. S. Peterka, and A. G. Suits, J. Chem. Phys 110, 6 (1998).

22. H. T. Le, M. Flock, and M. T. Nguyen, J. Chem. Phys. 112, 3 (2000).

23. J. Troe, Chem. Phys. Lett. 122, 425 (1985).

24. D. M. Hirst, J. Chem. Phys 115, 9320 (2001).

25. Y.-H. Chiu, H. Fu, J.-T. Huang, and S. L. Anderson, J. Chem. Phys. 102, 1199 (1995).

26. G. A. Fisk, J. D. McDonald, and D. R. Herschbach, Discuss. Faraday Soc. 44, 228 (1967).

27. Y.-H. Chiu, H. Fu, J.-T. Huang, and S. L. Anderson, J. Chem. Phys. 101, 5410 (1994).

28. R. J. Green, H.-T. Kim, J. Qian, and S. L. Anderson, J. Chem. Phys. 113, 4158 (2000).

29. R. J. Green and S. L. Anderson, Int. Rev. Phys. Chem. 20, 165 (2001).

30. J. Liu and S. L. Anderson, Int. J. Mass Spectrom. 241, 173 (2005).

31. U. Lourderaj and W. L. Hase, J. Phys. Chem. 113, 17 (2008).

32. P. Baltzer, L. Karlsson, B. Wannberg, D. M. P. Holland, M.A. MacDonald, M. A. Hayes, and J. H. D. Eland, Chemical Physics 237, 451 (1998).

33. R. D. Levine and R. B. Bernstein, *Molecular Reaction Dynamics and Chemical Reactivity*. (Oxford University Press, New York, 1987).

34. M. E. Jacox, J. Phys. Chem. Ref. Data 13, 945 (1984).

35. G. Herzberg, *Molecular Spectra and Molecular Structure III. Electronic Spectra and Electronic Structure of Polyatomic Molecules* (Van Nostrand Reinhold, New York, 1966).

Table 5.1.

Product velocity distribution simulations results

E_{col} (eV)	$< E_{avail} >$ [a] (eV)	$< E_{recoil} >$ (eV)	$< E_{recoil} > / < E_{avail} >$ (%)	$\tau_{collision}$ (psec)	$\tau_{fly\text{-}by}$ [b] (psec)
NO_2^+					
0.16	2.01	0.16	8	>0.9	0.36
0.44	2.27	0.32	14	0.2	0.22
1.03	2.86	0.66	23	0.08	0.15
3.10	4.93	2.80	57	0.04	0.0833
$C_2H_2O^+$					
0.16	4.67	0.20	4	>2.4	0.36
0.44	4.95	0.19	4	1.4	0.22
1.03	5.49	0.44	8	0.39	0.15
3.10	7.59	0.86	11	0.15	0.0833
NO^+					
0.16	5.01	0.22	4	>2.4	0.36
0.44	5.27	0.20	4	1.4	0.22
1.03	5.83	0.47	8	0.39	0.15
3.10	7.92	0.90	11	0.15	0.0833

[a] $< >$ =mean value

[b] $\tau_{fly\text{-}by}$ defined as time for undeflected reactants to travel a relative distance of 5Å.

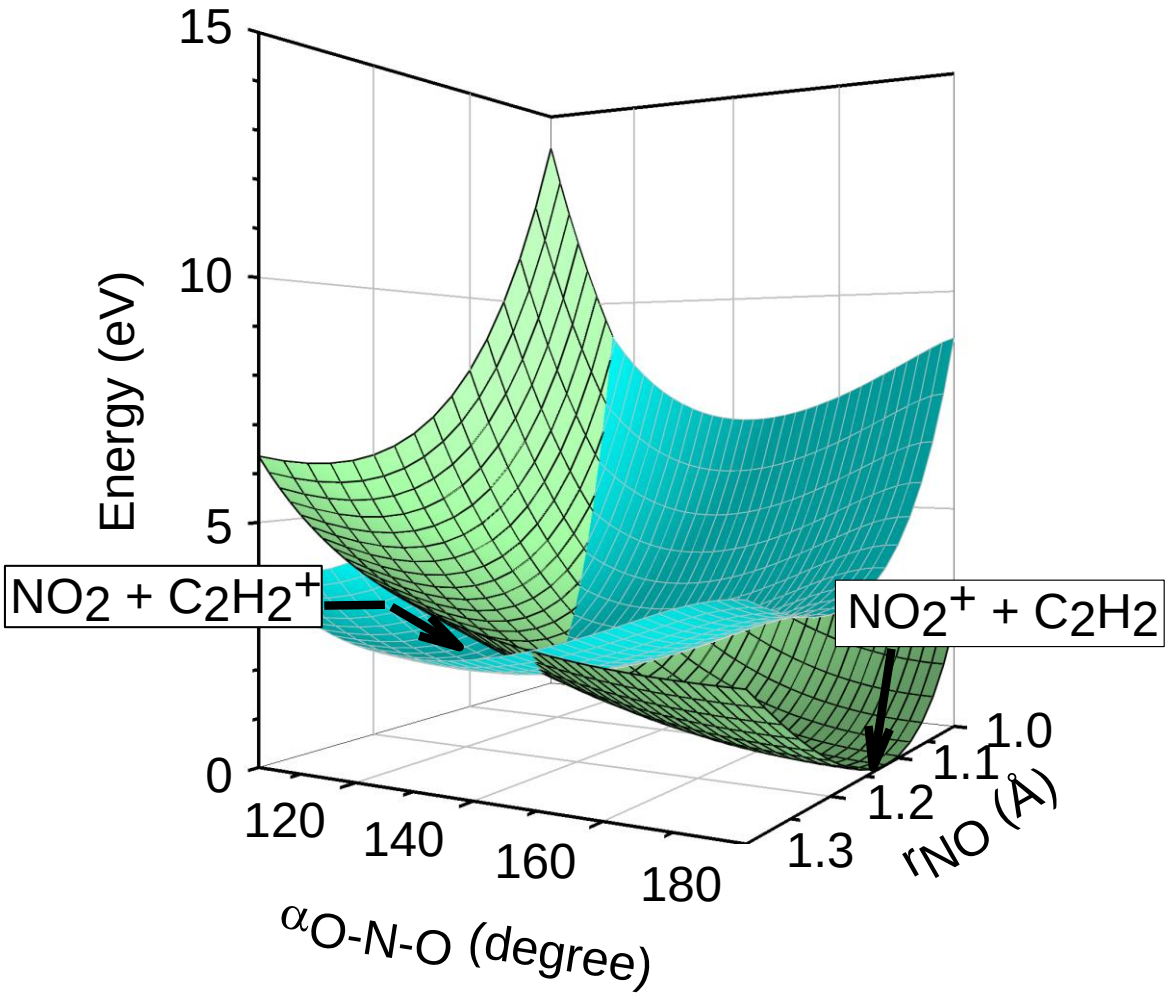

Figure 5.1. Cut through the two lowest energy potential surfaces for $(C_2H_2+NO_2)^+$ at infinite reactant separation (B3LYP/6-311+G**). The two coordinates shown are the NO_2 bend (α_{ONO}), and symmetric stretch (r_{NO}). The equilibrium geometries for NO_2^+ + C_2H_2 and for $C_2H_2^+$ + NO_2 are indicated by arrows (NO_2: α_{ONO} = 134.3°, r_{NO} = 1.193 Å; NO_2^+: α_{ONO} = 180°, r_{NO} = 1.118 Å)

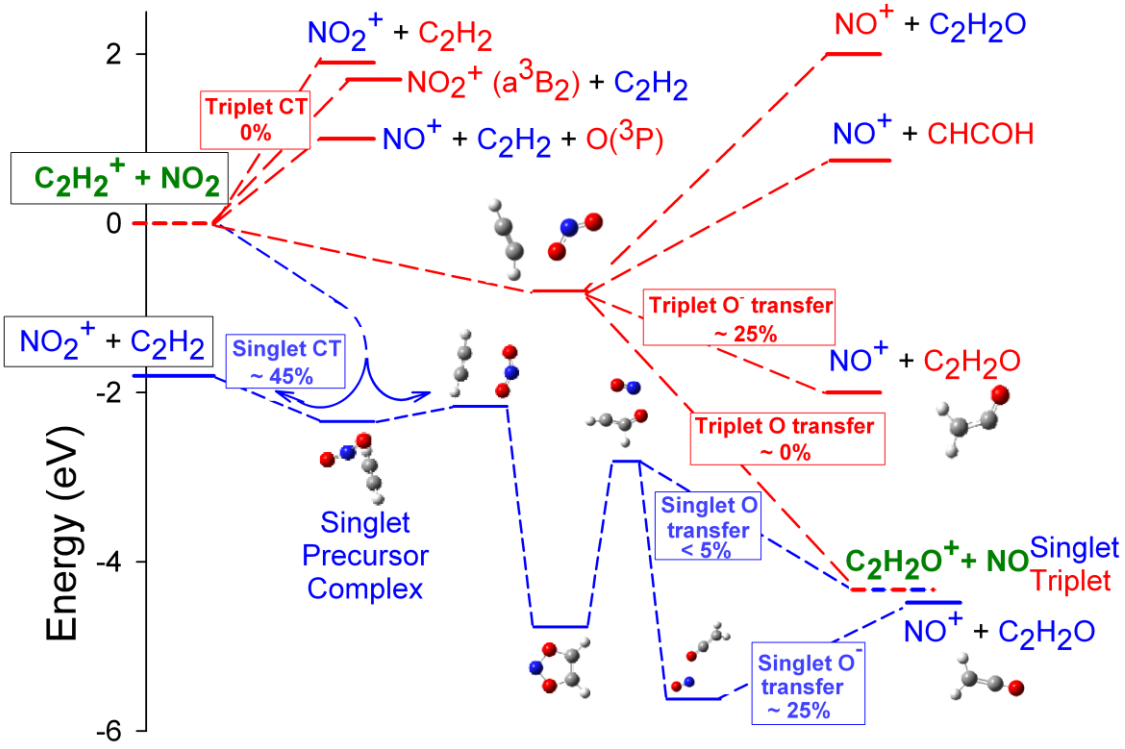

Figure 5.2. Reaction coordinate for the $(NO_2 + C_2H_2)^+$ system. Blue indicates species and reaction coordinates that are singlets, red indicates triplets, and green indicates doublets. The boxes giving percentages refer to the contribution of each channel to the total reactivity at a typical mid-range collision energy (0.44 eV).

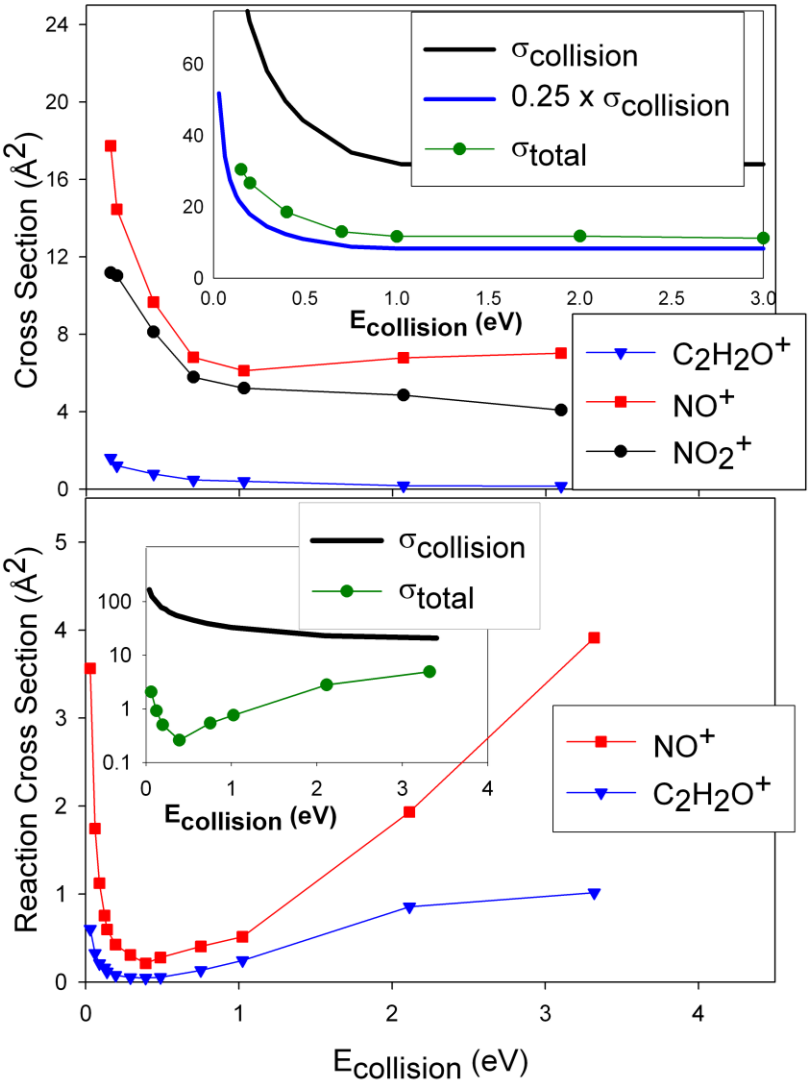

Figure 5.3. Top Frame: Integral cross sections for production of NO^+, $C_2H_2O^+$, and NO_2^+ in reaction of ground state $C_2H_2^+$ with NO_2. Bottom Frame: Cross sections for NO^+ and $C_2H_2O^+$ production in reaction of ground state NO_2^+ with C_2H_2. The insets to each frame compare the total reaction cross section (σ_{total}) with the collision cross section ($\sigma_{collision}$).

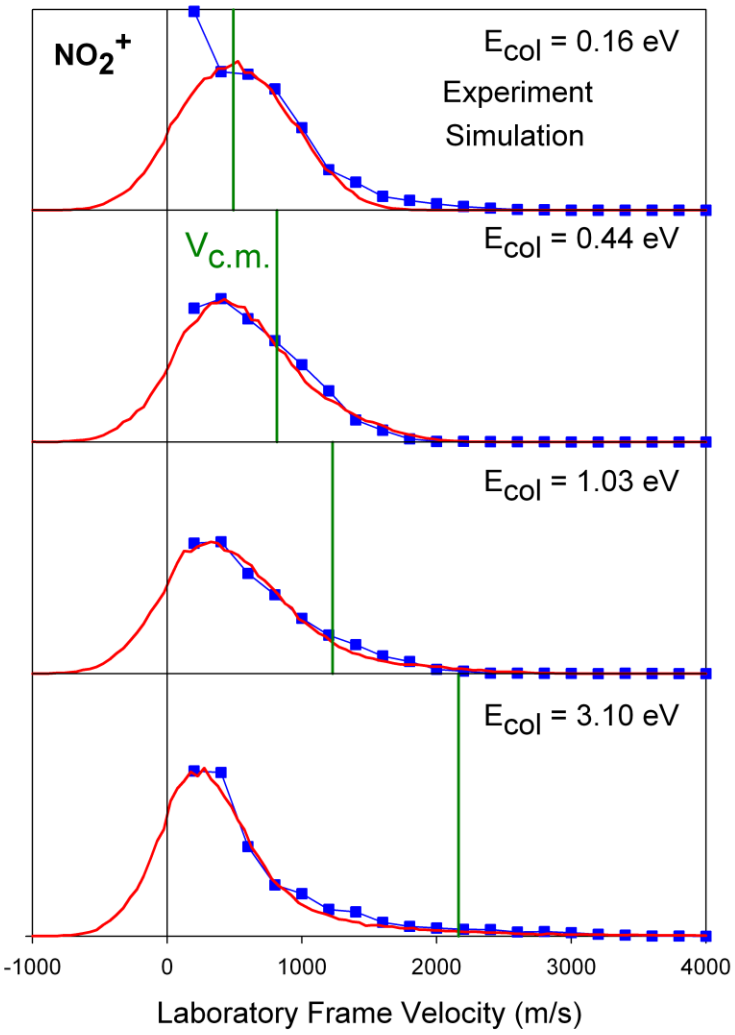

Figure 5.4. Lab frame v_{axial} distributions for the NO_2^+ product scaled to be proportional to the integral cross section at each energy. Points are experimental, and smooth curves are from simulations. The heavy vertical line in each frame indicates the lab velocity of the center-of-mass frame ($<V_{cm}>$).

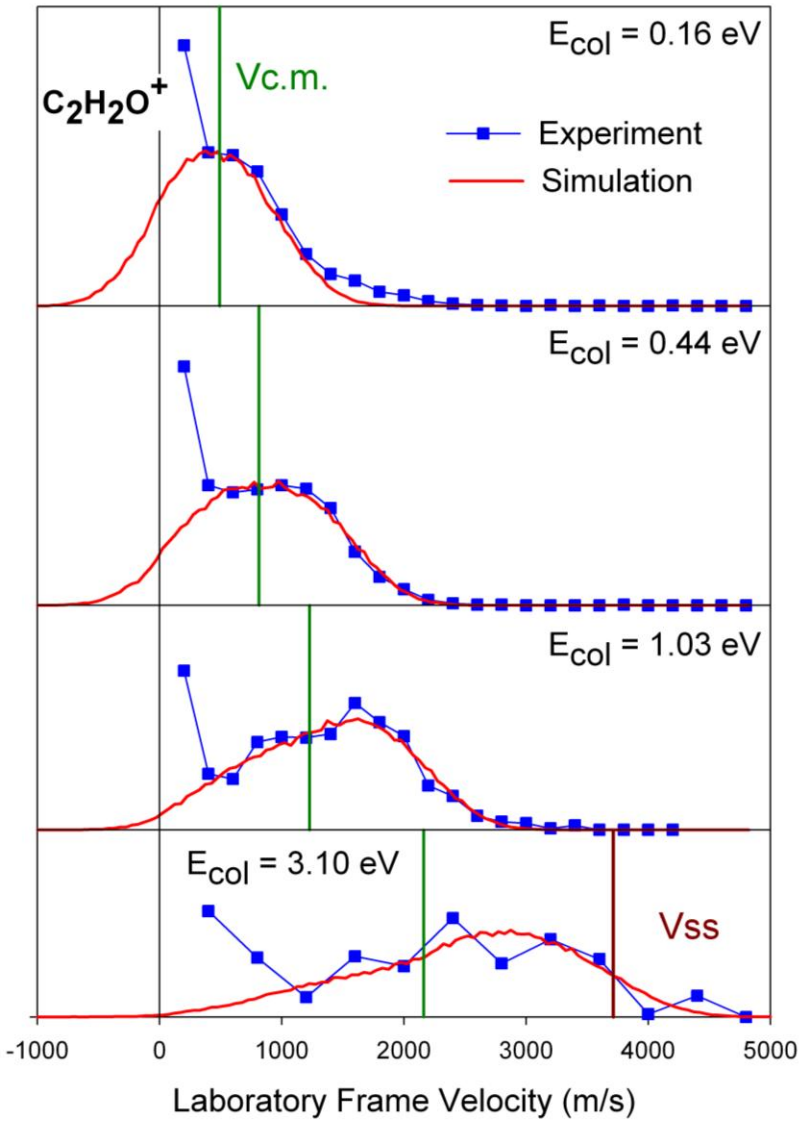

Figure 5.5. Lab frame v_{axial} distributions for the $C_2H_2O^+$ product, scaled to be proportional to the integral cross section at each energy. Points are experimental, and smooth curves are from simulations. The heavy vertical line in each frame indicates the lab velocity of the center-of-mass frame ($<V_{cm}>$), and the line labeled V_{SS} shows the spectator-stripping limit.

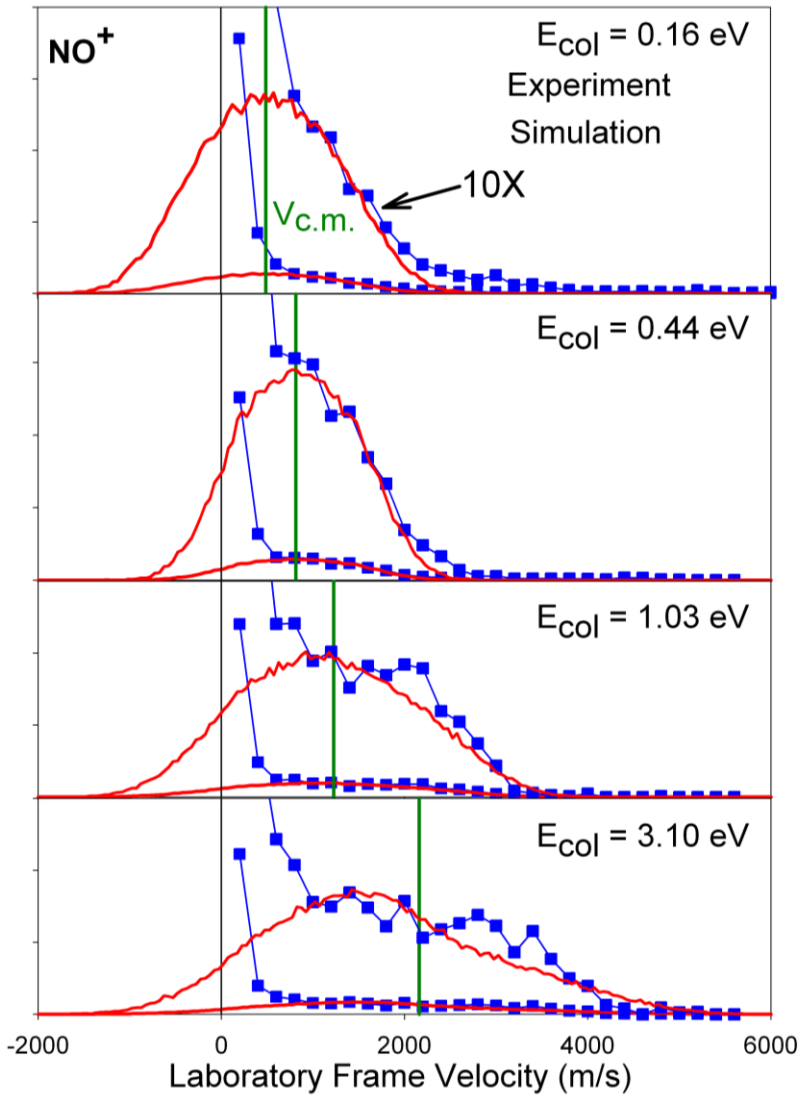

Figure 5.6. Lab frame v_{axial} distributions for the NO^+ product, scaled to be proportional to the integral cross section at each energy. Distributions are shown at both 1x and 10x scaling so that both the low velocity spike and broad components can be seen. Points are experimental, and smooth curves are from simulations. The heavy vertical line in each frame indicates the lab velocity of the center-of-mass frame ($<V_{cm}>$).

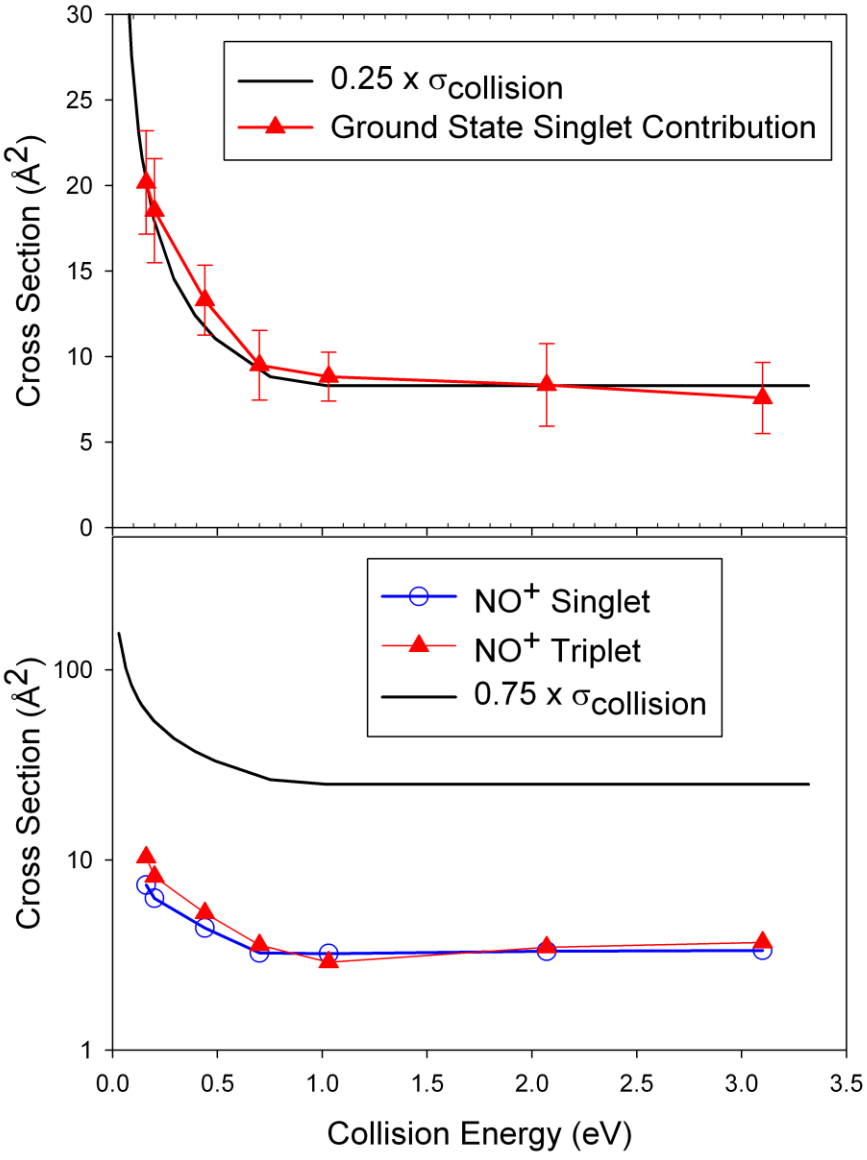

Figure 5.7. Top Frame: Comparison of the singlet collision cross section (0.25 x $\sigma_{collision}$) with the sum of the cross sections for NO_2^+, $C_2H_2O^+$, and the broad NO^+ component. Bottom Frame: Comparison of the extracted singlet and triplet contributions to the NO^+ cross section, with the triplet collision cross section (0.75 x $\sigma_{collision}$).

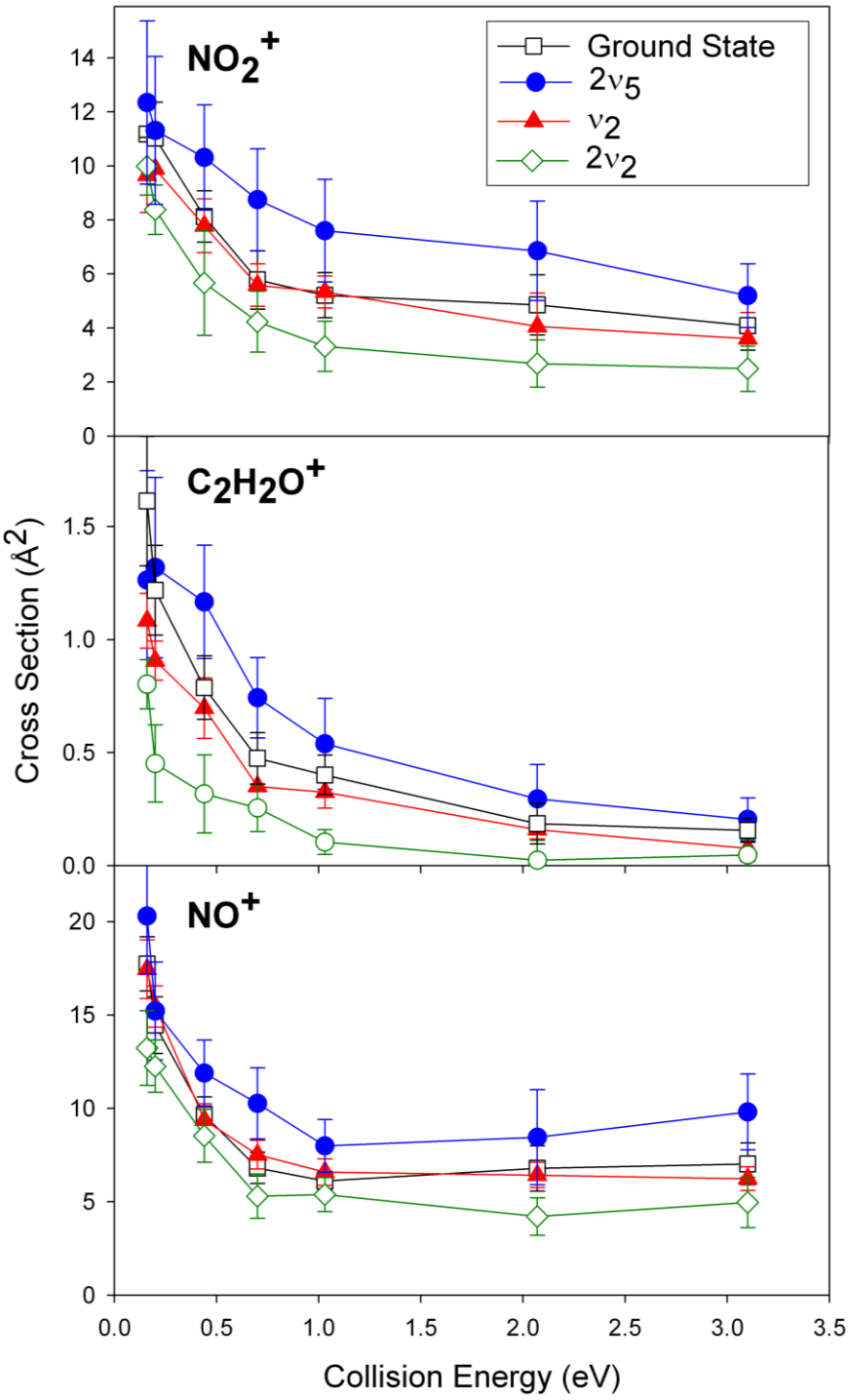

Figure 5.8. Effects of different $C_2H_2^+$ vibrational levels on the cross sections. Top Frame: NO_2^+ production. Middle Frame: $C_2H_2O^+$ production. Bottom Frame: NO^+ production.

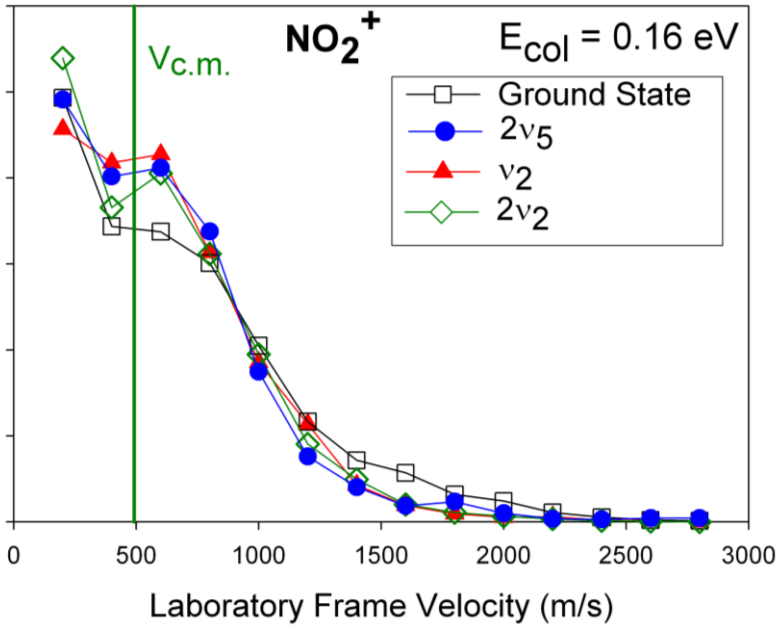

Figure 5.9. Effects of different $C_2H_2^+$ vibrational levels on the v_{axial} distributions for CT at E_{col} = 0.16 eV

CHAPTER 6

REACTION OF HOD^+ WITH NO_2: EFFECTS OF OD AND OH STRETCHING, BENDING, AND COLLISION ENERGY ON REACTIONS ON THE SINGLET AND TRIPLET POTENTIAL SURFACES

Overview

Integral cross sections and product recoil velocity distributions were measured for reaction of HOD^+ with NO_2, in which the HOD^+ reactant was prepared in its ground state, and with mode-selective excitation in the 001 (OH stretch), 100 (OD stretch) and bend (010) modes. In addition, we measured the 300 K thermal kinetics in a selected ion flow tube reactor and report product branching ratios different from previous measurements. Reaction is found to occur on both the singlet and triplet surfaces with near unit efficiency. At 300 K, the product branching indicates that triplet→singlet transitions occur in about 60% of triplet-coupled collisions, which we attribute to long interaction times mediated by complexes on the triplet surface. Because the collision times are much shorter in the beam experiments, the product distributions show no signs of such transitions. The dominant product on the singlet surface is charge transfer. Reactions on the triplet surface lead to NO^+, NO_2H^+ and NO_2D^+. There is also charge transfer, producing NO_2^+ (a^3B_2), however, this triplet NO_2^+ mostly predissociates. The NO_2H^+/NO_2D^+ cross sections peak at low collision energies and are insignificant above ~1 eV, due to OH/OD loss from the nascent product ions. The effects of HOD^+ vibration are mode specific. Vibration inhibits charge transfer, with the largest effect from the bend. The NO_2H^+/NO_2D^+ channels are also vibrationally inhibited, and the mode dependence reveals how energy in different reactant modes couples to internal energy of the product ions.

Introduction

Water with a single deuterium label, HOD, is interesting from a vibrational dynamics perspective because the 100 mode has primarily OD stretching character, the 001 mode is primarily an OH stretch, and the 010 mode (the bend) involves yet another distinct type of motion. This fact was exploited in studies of H vs. D transfer reactions of HOD with hot H atoms[1-6] and with Cl atoms.[7] Reaction of HOD excited to the 4th overtone of the OH stretch or to the nearly isoenergetic 5th overtone of the OD stretch showed a strong propensity to break the excited bond.[8] Zare and coworkers showed that even for excitation of the fundamental of these modes, there were dramatic shifts in the OH vs. OD product branching, again strongly favoring breaking the excited bond.[3] Vibrational energy was found to be ~120 times more effective at driving reaction than equal amounts of collision energy. Furthermore, the initial mode of excitation had a strong effect on how energy was partitioned to internal states of the product. For example, in the Zare experiments on HOD + Cl, fundamental OH stretch excitation lead 73% of the available energy partitioned to the HCl stretch, leaving the OD spectator bond in its vibrational ground state.[5] Similarly, in the study of OD stretch-excited HOD reacting with hot H atoms, the OH products were exclusively produced in v=0, while OD products were formed in v=1, i.e., the reaction preserved the excitation level in the spectator bonds.

The effects of bond-specific excitation in neutral-neutral collisions mostly result from the effects of the excitation on crossing the rather substantial barriers to reaction. In most ion-molecule reactions, attractive electrostatic interactions and the stabilization that results from charge delocalization in the collision complex, tends to reduce the energy in

the region of the potential surface where bonds are being broken and made, and therefore tends to reduce or eliminate barriers to reaction. As a result, it is not obvious what to expect in the way of mode or bond-specific vibrational effects. Here we present a study of the reaction of HOD^+ with NO_2, chosen because in this system, H^+ and D^+ transfer are essentially thermoneutral. Furthermore, the resulting NO_2H^+ and NO_2D^+ products have low energy OH or OD loss channels, and this secondary dissociation process provides a built-in "thermometer" that allows us to monitor how energy initially in the bond that breaks, vs. the spectator bond, is partitioned to internal energy of the products.

When a pair of doublet spin molecules like HOD^+ and NO_2 collide, one quarter of collisions will occur with singlet coupling of the unpaired electrons on the two reactants, and three quarters of collisions will occur with triplet coupling. In many systems, such triplet-coupled collisions are unreactive or even repulsive because the unpaired electrons are unable to form bonds.[9] One question of interest for this system, therefore, is the extent to which reaction occurs on the triplet surface. Another point of interest is the possibility for singlet ↔ triplet transitions during collisions. Because there are no heavy atoms with large spin-orbit coupling constants, the singlet ↔ triplet transition rate should be slow, however, if the collision times are long enough, transitions may be significant. This issue is addressed below by comparing product branching in thermal kinetic and beam measurements, probing collisions over timescales that vary by orders of magnitude, and therefore providing insight into the time scale for such spin forbidden processes.

The thermal energy kinetics of H_2O^+ with NO_2 were previously studied in both flow-drift tube (FDT)[10] and selected ion flow tube (SIFT)[11] configurations at 300 K, and both

studies reported a rate constant of 1.2 x 10^{-9} cm^3/mol·sec, corresponding to essentially unit reaction efficiency. The reported branching was 100% to the NO_2^+ product of charge transfer (CT). There are several surprising aspects of this result. CT can only produce singlet products at thermal energies, because the triplet CT channel is endoergic. Therefore, the 100% NO_2^+ branching implies that all collisions starting with triplet coupling, end up on the singlet surface, even though there are exothermic triplet reactions producing NO^+ and $NO^+(H_2O)$ that should be quite efficient. The absence of signal for these triplet product channels would seem to imply that they have significant barriers, as well as requiring unusually strong singlet-triplet coupling.

To provide further insight into these issues, we present a combined thermal energy and beam study of this system. We report integral cross sections and product recoil velocity distributions for reaction of HOD^+ with NO_2, in which the HOD^+ reactant was prepared in its ground state, and with mode-selective excitation in the 001 (predominantly OH stretch), 100 (predominantly OD stretch) and bend (010) modes. In addition, we re-measured the 300 K kinetics in a SIFT apparatus, with careful attention to extracting branching ratios.

Experimental and Computational Methods

State-Selected Beam Experiments

The cross section measurements were made in a guided ion beam instrument at the University of Utah, described in detail previously,[12,13] along with our calibration and data analysis procedures. HOD^+ is produced in its ground state or with one quantum of bend (010 = 153 meV), OD stretch (100 = 293 meV), or OH stretch (001 = 397 meV)

excitation, by 2+1 REMPI through the C $^1B_1$ state.[14] State purity measured by photoelectron spectroscopy is essentially 100% for HOD^+ in its ground state and with one quantum of either OD or OH stretch excitation, however, when preparing bend-excited HOD^+, ~56% of the ions are in the desired state, with 44% in the ground state. Because we measure cross sections for the ground state reaction, the cross sections for bend excitation can be obtained by subtraction, which has been done for all the results below.

For these experiments, Helium was bubbled through a room temperature $H_2O/HOD/D_2O$ mixture, producing ~4% water/He that was pulsed into the experiment as a supersonic beam, and then collimated by a skimmer before passing into the ionization region. Ionization occurred between a pair of planar electrodes, and the resulting ions were then injected into a quadrupole ion guide, which focused them into a quadrupole mass filter to remove any fragment and unwanted isotope ions produced in the REMPI process. At the end of the mass filter, a time-of-flight (TOF) gate was used to narrow the kinetic energy spread of the reactant ion beam. The state-, mass-, and energy-selected ions were injected into the first section of an 8-pole ion guide, and passed through a scattering cell containing 0.1 mTorr of NO_2. Product ions, together with unreacted H_2O^+, are contained within the guide and passed into a second, longer guide section for time-of-flight (TOF) velocity analysis. Product ions that are backscattered in the laboratory frame are reflected at the entrance of the guide by a positive potential on the injection lens, so that they can be detected. Finally, the ions are mass analyzed, and counted using a P7882 FAST ComTec multichannel scalar. The experiment is controlled by a LabView program that cycles through collision energies and masses of interest, and switches the

target gas flow between the scattering cell and chamber background, and accumulates TOF data for reactant and product ions at each energy. Integral cross sections are calculated from the ratio of reactant and product ion intensities, corrected for ions formed outside the scattering cell, using the calibrated effective length of the scattering cell[12] and the pressure, measured with a capacitance manometer, which is checked against an ionization gauge.

TOF is used both to measure the energy distribution of the reactant ion beam, and the axial projection of the recoil velocity distribution for the product ions (v_{axial}). The reactant ion velocity distributions at each E_{col} can be fit within experimental error to Gaussians, defining the absolute energy and energy spread (< 150 meV for all E_{col}) of the beam. TOF data were collected for product ions at a series of collision energies and for each vibrational state. Several complete sets of cross sections for the four reactant states and three product channels were recorded as a function of collision energy (E_{col}), each taking several days because the ion beam intensity obtainable by REMPI is relatively low (~1200 ions/sec). To avoid systematic errors comparing different vibrational states, the ground state cross sections were collected every day as a check on possible changes in instrument conditions. If the ground state cross section was found to differ from the average by more than 10%, the entire day's data was discarded. Based on the variations from set-to-set, we estimate that the relative error in comparing cross sections for different vibrational states or collision energies is <15%, including statistical and systematic errors. The exception is that for the weak NO_2H^+ and NO_2D^+ channels, particularly at high E_{col}, the statistical error is larger, and can be judged from the scatter

in the data. We estimate the uncertainty in the absolute cross section to be about 20% due to possible mass dependent detection efficiency in the final mass spectrometer.

We considered the possibility that the NO_2 in the scattering cell might be contaminated by either NO, or by N_2O_4, which is in equilibrium with NO_2. If either contaminant were present at concentrations greater than a few percent, there would be significant contributions to the NO^+, and possibly NO_2^+ product signals. Mass analysis of $NO/NO_2/N_2O_4$ mixtures is ambiguous because of fragmentation that is quite sensitive to small changes in ionization conditions. The presence of significant NO was ruled out by running a gas-phase IR spectrum of the NO_2 at high enough pressure that the weak symmetric stretch transition for NO_2 was nearly saturated. No signal was seen for the much stronger NO stretch transition. The equilibrium concentration of N_2O_4 at the 10^{-4} Torr pressure in our scattering cell is negligible,[15] but we had some concern that the time constant for reaching equilibrium[16] might leave some undissociated N_2O_4. This possibility was tested by measuring cross sections using NO_2 supplied from reservoirs at atmospheric pressure and at ~50 Torr, where the equilibrium N_2O_4 concentration is 13% and 1%, respectively. No change in product cross sections was observed, thus we conclude that both NO and N_2O_4 contaminants are negligible under our conditions.

Selected Ion Flow Tube (SIFT) Measurements

The measurements of the 300 K kinetics were performed using the Air Force Research Laboratory's selected ion flow tube (SIFT). The details of the instrument have been described previously[17] and only information important to the specific experiments is reported here. H_2O^+ is generated by electron impact from water vapor. While we can

selectively inject the desired ion into the flow tube, H_2O and O_2 impurities in the helium buffer gas created H_3O^+ (~30%) and O_2^+(~10%) in the flow. Therefore, we studied these reactions under the same conditions and subtracted their influence from the product distributions. H_3O^+ was essentially nonreactive. The O_2^+ experiment showed that the NO_2 (1% in Helium) had a small NO impurity (2-4%). This was easy to correct for, because H_2O^+ reacting with NO produces only NO^+. Product branching was measured under low depletion conditions so that little secondary reaction occurred. The net effect of the corrections was small, well within our reported uncertainty, a few percent.

Computational Methods

To construct the reaction coordinate shown in Figure 6. 6.1, *ab initio* structure optimization calculations were performed at the PBE1PBE/6-311++G** level of theory using GAUSSIAN 03.[18] For all stable singlet structures and for the triplet products, the calculations were repeated at the G3 level, and for the singlet complexes and transition states, we also did single point calculations at the QCISD(T)/cc-pVTZ level at the geometries optimized at the PBE1PBE/6-311++G** level. The energetic trends were consistent for the levels of theory and are reported in Table 6.1.

We also calculated a small set of quasi-classical trajectories to examine breakup of a covalently bound complex on the singlet reaction coordinate. The VENUS program of Hase and co-workers[19] was used to calculate the quasi-classical initial conditions, and direct dynamics trajectories were integrated at the B3LYP/6-31G* level using the updating Hessian method of Schlegel and co-workers,[20] implemented in GAUSSIAN03.[18]

Results and Discussion

Reactions and Reaction Coordinate

Product ions are observed in the beam experiments at masses 46 (NO_2^+), 47 (NO_2H^+), 48 (NO_2D^+), and 30 (NO^+), with the corresponding energetics listed in Table I. The experimental[21,22] energetics for all primary reactions that might lead to the observed product ions are:

$H_2O^+ + NO_2$

$\rightarrow NO_2H^+ + OH$	(H^+ transfer)	$\Delta H_{rxn}(0K) = +0.012$ eV
$\downarrow$		
$NO^+ + 2\ OH$	(2^{nd}'ry dissoc.)	$\Delta H_{rxn}(0K) = +0.54$ eV
$\rightarrow NO_2^+ (^1\Sigma_g) + H_2O$	(singlet CT)	$\Delta H_{rxn}(0K) = -3.03$ eV
$\rightarrow NO_2^+ (a^3B_2) + H_2O$	(triplet CT)	$\Delta H_{rxn}(0K) = +0.17$ eV
$\downarrow$		
$NO^+ + O\ (^3P) + H_2O$	(sequential triplet dissoc. CT)	
$\rightarrow NO^+ + O\ (^3P) + H_2O$	(concerted dissoc.)	$\Delta H_{rxn}(0K) = -0.18$ eV
$\rightarrow NO^+ + O\ (^1D) + H_2O$	(singlet dissoc. CT)	$\Delta H_{rxn}(0K) = +1.78$ eV
$\rightarrow NO^+ + HOOH$	(O^- abstraction)	$\Delta H_{rxn}(0K) = -1.67$ eV
$\rightarrow NO^+(H_2O) + O\ (^3P)$	(triplet O elimination)	$\Delta H_{rxn}(0K) = -0.82$ eV

The value given for H^+ transfer is an average of that calculated from 0 K heats of formation (0.014 eV), and that gotten by correcting the difference in proton affinities for NO_2 and OH to 0 K (0.010 eV). The "sequential triplet dissociative CT" channel corresponds to CT to form NO_2^+ (a^3B_2), followed by predissociation to $NO^+ + O\ (^3P)$, thus the effective barrier is the 0.17 eV endoergicity associated with forming NO_2^+ (a^3B_2). The value given for the final reaction listed was determined from a PBE1PBE/6-

311++G** calculation (BSSE-corrected) for the stabilization energy of the $NO^+(H_2O)$ complex, referenced to the experimental energy for $NO^+ + O\ (^3P) + H_2O$.

For reaction of HOD^+ the energetics are slightly different due to zero point energy (ZPE). The only channel where ZPE has a significant effect is H^+ vs. D^+ transfer. Using the experimental endoergicity for H^+ from H_2O, and taking the reactant and product ZPEs from calculations at the B3LYP/6-311G(df,p) level, scaled by 1.0167,[23] we find:

$HOD^+ + NO_2 \rightarrow NO_2H^+ + OD$ (H^+ transfer) $\Delta H(0K) = +0.017$ eV

$\rightarrow NO_2D^+ + OH$ (D^+ transfer) $\Delta H(0K) = -0.010$ eV

i.e., H^+ transfer from HOD^+ is slightly more endoergic than from H_2O^+, but D^+ transfer from HOD^+ is actually slightly exoergic. It is not clear how important this ~27 meV difference in energetics for H^+ vs. D^+ transfer might be, given that at our lowest E_{col}, the available energy is an order of magnitude greater (E_{col} + NO_2 rotation ≈ 0.3 eV). We also calculated the density of states (DOS) in the two product channels in the low E_{col} range where they are significant. The density of states is ~10% higher in the NO_2H^+ + OD channel, compared to NO_2D^+ + OH, thus this factor might tend to compensate for the small difference in energetics.

Figure 6.1 shows the reaction coordinate assembled using experimental energetics[21,24,25] for reactants and products, and energies calculated at the PBE1PBE/6-311++G** level for complexes and transition states, referenced to the calculated reactant energy. To simplify the diagram, the reaction coordinate is shown for H_2O, rather than HOD. Species and reaction coordinates that are singlets are shown in blue, triplet species and reaction coordinates are in red, and doublet species are in green. The H_2O^+ and NO_2

reactants are both doublets, therefore collisions will occur in both singlet and triplet coupling, with a 1 : 3 ratio. A flowing afterglow study[26] was reported for the termolecular reaction:

$$NO_2^+ + H_2O + N_2 \rightarrow H_2NO_3^+ + N_2 \quad k = 2 \times 10^{-27}\ cm^6mol^{-2}sec^{-1}.$$

This result implies that, not surprisingly, there is no barrier separating $NO_2^+ + H_2O$ (the CT products of the reaction here) from the complex labeled SC1 in Figure 6.1. Because of the high energy of TS1, it would not have been possible to produce the complex labeled "$NO_3H_2^+$" under the thermal conditions of this study.

Singlet Reactions

The reaction expected to dominate in singlet collisions is charge transfer (CT), producing $NO_2^+ + H_2O$. Unlike atom transfer reactions, where the collision geometry must allow bond formation, the highly exoergic CT reaction can occur in any orientation, and density of states considerations suggest that it should be highly efficient. The singlet complex labeled "SC1", about 0.8 eV below the CT product energy, is essentially an electrostatically bound complex of the CT products, and statistical breakup of SC1 should go to CT products with essentially unit probability. The fact that the charge is localized on the NO_2 moiety in SC1 is obvious from the ONO bond angle (173°), which is much closer to that for NO_2^+ (180°) than for NO_2 (134.1°). This raises the point that NO_2 bending is intimately coupled to any reaction coordinate that involves charge transfer.

The covalently bound "$NO_3H_2^+$" complex, connected to SC1 by a four-center TS1, might provide a route to other product channels on the singlet surface. Formation of $NO_3H_2^+$ by statistical isomerization from SC1 would be negligible, because TS1 is both

higher in energy, and much tighter than the orbiting TS that controls separation to CT products. On the other hand, it is possible that $NO_3H_2^+$ might form directly in a small fraction of collisions that happens to occur with geometries allowing concerted N-O and O-H bond formation. If formed, this complex can decay via TS1 to CT products, by OH elimination to NO_2H^+, or to NO^+ + HOOH by a three centered TS that we were unable to locate computationally. To obtain an estimate of the branching for decay of this complex, and to obtain insight into the nature of the TS governing decay to NO^+ + HOOH, we calculated quasi-classical trajectories for unimolecular decay of highly excited $NO_3H_2^+$. A few 4000 step trajectories were examined for internal temperatures of 4000, 6000, 8000, 10000, 12000 and 14000 K, and based on those results, a larger set of 35 trajectories were run at 8000 K, chosen as a reasonable compromise between dissociating within the 1.5 psec trajectory time, while avoiding the sometimes bizarre initial conditions that result at higher temperatures. It should be noted that the average total internal energy in the complex at 8000 K corresponds to $E_{col} \approx 7$ eV, i.e., about double the maximum studied experimentally. Of the 8000 K trajectories that dissociated to products during the integration period, the branching between the three decomposition channels was: $(NO_2^+ + H_2O)$: $(NO^+ + HOOH)$: $(NO_2H^+ + OH) = 5 : 1 : 1$, i.e., decomposition is dominated by decay over TS1 to CT products. Because TS1 is a tight four centered TS, the small branching to NO^+ + HOOH suggests that this TS (a tight three center TS) must be rather high in energy, as indicated in Figure 6.1.

H^+ transfer should be possible by a direct scattering mechanism on either the singlet or triplet surfaces. H^+ transfer often proceeds near the collision rate in systems where is

it exoergic.[27] Here, it is endoergic, but only by ~12 meV, which is far less than the available energy even at our lowest E_{col}. H^+ transfer products also were a minor channel in the 8000 K $NO_3H_2^+$ trajectories, however, at the lower energies probed in the experiments, this high energy decay channel would probably be negligible. Thus, we expect that any H^+ transfer that happens on the singlet surface, will go by a direct mechanism.

NO^+ can also form on the singlet surface. The NO^+ + HOOH channel probably requires mediation by the $NO_3H_2^+$ complex, but the trajectories together with inefficient formation of $NO_3H_2^+$, suggest that this mechanism should be minor. Note, however, that the NO_2H^+ product from H^+ transfer is only stable by ~0.53 eV with respect to OH elimination, producing NO^+ + 2 OH. To the extent that H^+ transfer occurs on the singlet surface, dissociation of the nascent NO_2H^+ product provides another singlet route to NO^+ production except at low E_{col}.

Triplet Reactions

On the triplet reaction coordinate, there is no facile exoergic process like CT competing with the atom transfer reactions. There is a reactant-like triplet complex (TC1) where the charge is roughly equally distributed between the H_2O and NO_2 moieties. This complex can decay back to reactants, or via TS2 or TS3 toward products. TS2 and the resulting TC2 mediate proton transfer to the NO_2, generating NO_2H^+ + OH products. These H^+ products can presumably also form on the triplet surface by a direct mechanism. As discussed above, the nascent NO_2H^+ will dissociate to NO^+ + OH if its internal energy is greater than 0.53 eV.

There are several channels that involve CT or dissociative CT on the triplet surface. CT to produce $NO_2^+(a^3B_2)$ + H_2O is endoergic by 0.17 eV. This lowest energy triplet state of NO_2^+ predissociates to NO^+ + O (^3P),[21] and would survive to be detected as NO_2^+, only if its internal energy is below ~80 meV. For higher $NO_2^+(a^3B_2)$ internal energies, the sequence of triplet CT followed by predissociation provides a route to NO^+ on the triplet surface, which we are calling "sequential triplet dissociative CT". In addition to this endoergic sequential process, NO^+ can also be generated by a "concerted triplet dissociative CT" process. This reaction is concerted in the sense that the O-elimination step is concerted, going by TS3. The product of this transition is TC3, which is actually a bi-molecular product consisting of an electrostatically bound $NO^+(H_2O)$ complex plus the free O (^3P) atom. This $NO^+(H_2O)$ complex dissociates to NO^+ + H_2O under beam conditions, but in the 300 K kinetics experiment, this complex is sometimes collisionally stabilized.

300 K Kinetics

The 300 K rate constant is $1.3x10^{-9}$ cm^3 s^{-1} (unit reaction efficiency), in good agreement with past measurements,[10,11] however, we observe three reaction products, in contrast to the earlier work were only NO_2^+ was observed. NO_2^+ is the primary product, accounting for 70% (+8%/-11%) of the reaction. The remaining 30% is divided between two related products, NO^+, 20% (+7%/-4%) and $NO^+(H_2O)$, 10% (± 4%). The asymmetric uncertainty limits reflect corrections for contributions from reactions of contaminant ions, discussed below.

The observation of both NO^+ and $NO^+(H_2O)$ clearly shows reaction on the triplet surface, and both are consistent with the concerted triplet dissociative CT channel shown in Figure 6.1. After passing over TS3, the stationary point labeled TC3 is $NO^+(H_2O)$ plus a free O (^3P) atom. If the nascent $NO^+(H_2O)$ has high internal energy and is not collisionally stabilized, then it dissociates to $NO^+ + H_2O$. Otherwise it is detected as $NO^+(H_2O)$. The fact that the $NO^+(H_2O)$: NO^+ branching is 1 : 2, suggests that the nascent $NO^+(H_2O)$ is quite hot, such that it mostly dissociates before it can be stabilized by collisions with the He buffer gas (time between collisions ≈ 0.1 μsec). This conclusion is consistent with the beam experiments, where no $NO^+(H_2O)$ is observed. We did not observe the H^+ transfer product NO_2H^+, even though the endoergicity is small compared to the energy available from translation and rotation at 300 K. It could be that this channel is suppressed by competition with the more energetically favorable NO^+ and $NO^+(H_2O)$ channels. We note however, that NO_2H^+ is only bound by 0.53 eV with respect to $NO^+ + OH$, raising the possibility that it was destroyed by He buffer gas collisions in the flow tube. Dissociation is possible because there are enough collisions in the flow tube that dissociation processes requiring up to ~0.5 eV can be driven, albeit slowly, by the high energy tail of the Boltzmann distribution.[28]

Unlike the previous flow tube studies, we observe NO^+ and $NO^+(H_2O)$ products that clearly result from reactions on the triplet surface. Nonetheless, the 70% branching to NO_2^+ is still considerably larger than the 25% that would be expected from singlet CT, and the endoergicity of triplet CT (0.17 eV) is too large for it to make up the difference. It appears, therefore, that ~60% of the collisions starting on the triplet surface must be

transferring to the singlet surface during thermal energy collisions, leading to CT products. Such efficient triplet → singlet conversion is not surprising in light of the triplet reaction coordinate in Figure 6.1, which has several deep wells and no low energy exit channels. TC1 and TC2 presumably interconvert rapidly via TS2 under thermal conditions, thus the rate-limiting TS must be TS3. We estimated the lifetime of complex TC1 with respect to decay over TS3, using an RRKM calculation[29] based on the theoretical energies and vibrational frequencies for TC1 and TS3. For $E_{col} \approx 0$, corresponding to thermal energy collisions, the RRKM lifetime is ~ 110 picoseconds, assuming angular momentum from the average capture collision. As shown below, the beam experiments can be explained without invoking triplet → singlet conversion, reflecting the fact that the minimum E_{col} in the beam work is an order of magnitude higher, which increases the rate of passage over TS3 by an order of magnitude. Furthermore, two additional triplet product channels are open even at the lowest E_{col} probed in the beam experiments, decreasing the TC1 lifetime into the < 5 picosecond range. Assuming that the triplet→ singlet conversion rate is independent of E_{col}, the shorter collision time would result in < ~4% of triplet collisions converting to the singlet surface.

In the previous flow tube experiments, contaminant primary ions almost certainly played a role. In the Dotan et al. paper,[10] the H_2O^+ was made in the flow tube by CT between He^+ and water, and the paper notes that "H_2O^+ ions were among the abundant species". He^+ CT with water produces ~83% OH^+, which therefore must have been a major reactant ion in this flow drift tube experiment. Since it is known that OH^+

produces both NO^+ and NO_2^+,[11] it is probable that the reactions leading to NO^+ and NO_2^+ were not correctly identified. While the Shul et al.[11] work was done in a SIFT, they state that it was not possible to separate OH^+, H_2O^+, and H_3O^+ in the reactant ion selection quadruple, thus again, all three ions were present in the flow tube simultaneously.

Integral Cross Sections and Product Branching

The integral cross sections for production of NO^+, NO_2^+, NO_2H^+, and NO_2D^+ in reaction of ground state HOD^+ with NO_2 are shown in Figure 6.2 over the center-of-mass collision energy range from 0.27 to 2.94 eV. The inset of the figure compares the total reaction cross section (σ_{total}), with the collision cross section (σ_{col}), which is calculated as the capture cross section ($\sigma_{capture}$), including ion-induced dipole, and rotationally averaged ion-dipole forces, using the method of Troe.[30] The hard sphere cross section (calculated from orientation-averaged contact distances for HOD^+ and NO_2 assuming covalent radii) is not shown because it exceeds $\sigma_{capture}$ only for $E_{col} > 3.4$ eV. Note that σ_{total} is essentially equal to σ_{col}, indicating that both singlet and triplet reactions proceed at near-unit efficiency. For comparison the main frame of the figure also shows the singlet collision cross section, i.e., 25% of σ_{col}.

While both the thermal kinetics and beam experiments indicate essentially unit reaction efficiency, the product branching is quite different. In the beam experiment NO^+, primarily resulting from triplet reactions, is the dominant channel over most of the energy range, out-competed by NO_2^+ only at low E_{col}. The NO_2H^+ and NO_2D^+ channels have similar magnitudes and together amount to ~20% of the σ_{total} at low E_{col}, but drop to negligible values above 1 eV. Despite being ~17 meV endoergic, H^+ transfer is slightly

more efficient than the ~10 meV exoergic D^+ transfer process. If the mechanism were complex mediated, the branching might reflect the ~10% higher density of states for the H^+ transfer products. In a direct mechanism, the collision dynamics might favor NO_2H^+ + OD.

The difference in branching between the SIFT and beam experiments is attributable to two factors. The much longer collision times at thermal energies allow substantially more triplet → singlet conversion, which results mostly in production of NO_2^+. Furthermore, there are several moderately endoergic channels that are reasonably efficient at the energies probed in the beam study, but which are either energetically inaccessible, or depleted by competition in the thermal measurements. When these factors are considered, the two data sets are consistent with each other, and also with the reaction coordinate in Figure 6.1.

One obvious point is that, in the beam experiments, the cross sections for NO_2^+ and NO^+ are both significantly larger than $0.25 \cdot \sigma_{col}$, implying both these reactions have significant contributions from collisions on the triplet surface. For NO^+, this is no surprise because most of the processes that could potentially contribute are on the triplet surface (concerted and sequential dissociative CT, secondary dissociation of NO_2H^+). The magnitude of the NO_2^+ cross section is more surprising, however, because we expect that the dominant contribution to NO_2^+ should be singlet CT. Under beam conditions, endoergic triplet CT is also possible, however, the NO_2^+ (a^3B_2) product would predissociate[21] and be detected as $NO^+ + O\ (^3P)$ unless it is produced with internal energy

below ~80 meV. Such collisions are certainly possible, particularly at low E_{col}, but it seems unlikely that triplet CT could account for such a large contribution to NO_2^+.

Instead, we attribute most of the "excess" NO_2^+ to a secondary reaction. Our normal scattering cell pressure (0.1 mTorr) is as low as practical, given the low mode-selected primary ion intensities. The probability that reactant ions make a single collisions with NO_2 at this pressure is ~3.5%, but for product ions that are generated with near-zero lab velocity, there is a high probability of being hit by thermal NO_2 as they slowly exit the scattering cell. This is one reason why we never attempt to interpret product recoil velocity distributions for slow ions (see below). In this case, the slow products can react:

$$NO_2H^+ + NO_2 \rightarrow NO_2^+ + NO_2H \qquad \Delta H = -1.28 \text{ eV}.$$

We tested the effect of this reaction on the NO_2H^+, NO_2D^+, and NO_2^+ channels by measuring the cross sections for reaction of ground state H_2O^+ at a scattering cell pressure one order of magnitude lower than normal, and the resulting cross sections are indicated by dashed lines in Figure 6.2. The low pressure cross sections for NO_2H^+ and NO_2D^+ were identical within the rather large uncertainty, thus only a single low pressure curve is shown, which is the average of the two cross sections. The signal/noise is poor, but it is clear that for low E_{col}, the NO_2H^+ and NO_2D^+ cross sections increase with decreasing NO_2 pressure, and the NO_2^+ cross section decreases, as would be expected if this secondary reaction were significant. Additional insight into the effect of this secondary reaction is obtained from the recoil velocity data.

Recoil Velocity Distributions and Reaction Mechanisms

Considerable insight into the reaction mechanisms is provided by measurements of the product ion recoil dynamics, which also allow a more quantitative analysis of issues such as secondary reactions. Figures. 6.3 – 6.6 give the laboratory frame axial projections of the recoil velocity distributions for the NO_2D^+, NO_2H^+, NO_2^+, and NO^+ product ions measured at select collision energies. The data series with points are experimental, and the smooth curves shown in some frames are simulations, discussed below. The black vertical line in each frame indicates the laboratory frame velocity of the center-of-mass ($<V_{cm}>$), averaged over the collision energy distribution. Axial velocity (v_{axial}) distributions are simply the projections of the full velocity distributions on the ion guide axis. Because the experiment has axial symmetry, the raw distributions directly reveal the qualitative dynamics. For example, ions that are faster (slower) than V_{cm} correspond to forward (backward) scattering of the product ion with respect to the reactant ion beam direction. Reactions mediated by a long-lived complex must result in v_{axial} distributions that are forward-backward symmetric about V_{cm}. Ions that are backscattered in the lab frame are reflected by the injection electrode at the entrance of the ion guide, and detected at long times, corresponding to apparently low velocities. The low velocity region (below ~500 m/sec) also has the worst perturbations from stray fields, and as discussed above, is most likely to be affected by secondary collisions. For these reasons, the portion of the velocity distribution below ~500 m/sec must be interpreted with these factors in mind. Because this system has a light projectile and

heavy target, V_{cm} is at low lab velocity, particularly at low E_{col}, with the result that a substantial fraction of the product ions appear below 500 m/sec.

The H^+/D^+ Transfer Reaction

NO_2H^+ and NO_2D^+ together account for about 20% of σ_{total} at low energies (38 % in the low pressure measurement), falling to <3% at the highest energies. This channel produces two doublet species, therefore it correlates to both the triplet and singlet surfaces. The singlet reaction could go by a direct mechanism, or could involve formation of the $NO_3H_2^+$ complex, followed by OH (OD) elimination. As argued above, the $NO_3H_2^+$ complex probably does not form very efficiently, and once formed trajectory analysis suggests that it would decompose mostly back to SC1 and CT products. The available energy is much lower as the system traverses the triplet reaction coordinate, thus for low E_{col}, the triplet complexes TC1 and TC2 have significant lifetimes (~5 psec at our lowest E_{col}). H^+/D^+ transfer can probably also occur in direct triplet collisions, without significant mediation by the complexes.

Direct and complex mediated H^+/D^+ transfer should result in very different v_{axial} distributions. Direct H^+ or D^+ transfer might be expected to give NO_2H^+ or NO_2D^+ that is strongly backscattered in the CM frame, because the light H^+ or D^+ carries little momentum. (Note: because the charge transfers in this reaction, small angle scattering corresponds to backward scattering). In the limit of spectator stripping,[31] the product ions would appear near zero lab velocity. In contrast, H^+/D^+ transfer mediated by a long-lived complex must generate products that are forward-backward symmetric with respect to V_{cm}.

The v_{axial} distributions for the NO_2D^+ + OH channel are shown in Figure 6.3, and the analogous distributions for the NO_2H^+ + OD channel are in Figure 6.4. Distributions at higher E_{col} are not plotted, because the cross sections for these channels are too low to give useful distributions. Consider the top frame of Figure 6.3, which gives the v_{axial} distribution for reaction of ground state HOD^+ at E_{col} = 0.32 eV. The experimental distribution looks reasonably forward-backward symmetric, which would tend to suggest that complex-mediated D^+ transfer is dominant. The rough forward-backward symmetry also appears at higher E_{col}, and for the NO_2H^+ distributions in Figure 6.4. It is important, however, to consider the effects of secondary reactions, which were shown (Figure 6.2) to be reacting away almost half the nascent NO_2D^+ and NO_2H^+ products formed at low $E_{col.}$

The probability that a NO_2H^+ or NO_2D^+ product ion will survive passage out of the scattering cell is highly dependent on its velocity because decreasing velocity increases the capture cross section, and also increases the residence time in the cell. The effects of thermal target motion on collision probability in a beam-gas configuration were discussed by Ramsey, and we follow the development given there.[32] The probability of passing *without* collision through a gas cloud of length, *l*, at velocity, *v*, is:

$$P_{survive}(v) = e^{\frac{-l}{\lambda_v}}$$

where λ_v is the mean free path, including the effects of thermal target motion:

$$\lambda_v = \pi^{1/2} \frac{(v/\alpha_G)^2}{n_G \sigma_{BG} \psi(v/\alpha_G)}$$

where α_G is the average thermal speed of the neutral target molecules, n_G is the number density of the neutral target, σ_{BG} is the collision cross section, and $\psi(v/\alpha_G)$ is.

$$\psi(x) = xe^{-x^2} + (2x^2 + 1)\int_0^x e^{-y^2}\,dy$$

Here σ_{BG} is assumed to be the velocity-dependent capture cross section, and l is the distance from the center of the scattering cell to its end, which is a lower limit on the average distance a scattered ion might have to travel to exit the gas cloud. Large lab scattering angles will, of course, increase the path length, and therefore decrease the survival probability.

The top frame of Figure 6.3 shows the results. The black curve, plotted against the right hand axis, shows the probability that NO_2D^+ survives without conversion to NO_2^+, assuming the limit that every capture collision leads to reaction. Note that for lab velocities greater than ~500 m/sec, the secondary collision probability is low, and therefore the survival probability is high. At lower velocities, $P_{survive}$ drops rapidly to zero, indicating that the portion of the v_{axial} distribution that is backward-scattered with respect to V_{cm} should be significantly attenuated by conversion to NO_2^+. We can use $P_{survive}$ to reconstruct what the v_{axial} distribution would look like if there were no secondary collisions. The green dashed curve, which is a reasonable fit to the experimental data, was gotten by multiplying the red dashed curve by $P_{survive}$, i.e., the "true" v_{axial} distribution must look something like the red dashed curve. This red curve was generated from a dynamical model, and was convoluted with the velocity distributions of the ion beam and target gas, to allow direct comparison with experiment.[33,34]

The dynamical model used assumed a stripping-like process, wherein NO_2D^+ recoils with a velocity distribution peaking at 180° with an angular distribution symmetric about 180° with half width of 40°. The recoil energy distribution was assumed to be a Gaussian peaking at 70% · E_{avail} with width of ~20% · E_{avail}, where E_{avail} is the total energy available in the product channel. For comparison, the spectator stripping limit would give products at 180° with velocity corresponding to 77% of E_{avail} in recoil (83% for NO_2H^+). In contrast, reaction mediated by a long-lived complex would give an isotropic angular distribution, and would tend to partition a statistical fraction (~13%) of E_{avail} into recoil.

We certainly do not claim to be able to quantitatively extract the "true" v_{axial} distributions by this process, however, two points are clear. The true distributions are significantly backward peaked, implying domination by a direct stripping-like D^+ transfer mechanism. There may also be a small component of complex-mediated D^+ transfer producing products near V_{cm}, but this cannot account for more than ~30 % of the total reaction, even for this low E_{col}.

As a check on the model, it is useful to estimate the increase in D^+ transfer integral cross section that would result if there were no secondary reactions. This increase is simply the ratio of the area under the red and green dashed curves, and this "corrected" value of the integral cross section has been plotted as a single data point in Figure 6.2, which is in gratifyingly good agreement with the cross section curve extracted from the low pressure measurements (dashed curve - Figure 6.2).

In principle, such corrections could be made for all the v_{axial} distributions, however, given the ambiguity inherent in guessing the correct form of the model distributions, we do not feel that this level of interpretation is warranted. It is clear, however, that all of the v_{axial} distributions for both NO_2D^+ and NO_2H^+ must be significantly backward peaked, and therefore that D^+ or H^+ transfer goes predominantly by a direct mechanism, at all energies where these channels are significant.

Another interesting feature of the NO_2H^+ and NO_2D^+ channels is that their cross sections drop rapidly with increasing energy, to essentially zero by 2 eV. More typically, proton transfer cross sections tend to have E_{col} dependence that tracks that of σ_{col},[35-38] unless some other process is in competition. In this case, the competing process is secondary decomposition of the nascent NO_2H^+ and NO_2D^+ product ions, if they are produced with too much internal energy:

$$NO_2D^+ \rightarrow NO^+ + OD \qquad \Delta H_{rxn}(0K) = +0.58 \text{ eV}$$

$$NO_2H^+ \rightarrow NO^+ + OH \qquad \Delta H_{rxn}(0K) = +0.53 \text{ eV}.$$

The fact that the NO_2H^+ and NO_2D^+ signals essentially disappear as E_{col} is raised between 1 and 2 eV, is consistent with the model recoil dynamics used to fit the v_{axial} distribution at low E_{col} in Figure 6.3, where we assumed that an average of ~70% of E_{avail} is partitioned to recoil energy, leaving ~30% in internal energy. Given the high frequency of the OH or OD stretches, it is expected that most of this internal energy should go into the NO_2D^+ or NO_2H^+ products, and in that case, it is not surprising that these products have largely disappeared by $E_{col} \approx 1$ eV. The effect of this dissociation can also be seen directly in the v_{axial} distributions in Figures. 6.3 and 6.4. For $E_{col} \leq 0.5$

eV, the available energy is too low for there to be any dissociation of the NO_2H^+ or NO_2D^+ product ions, at least for the ground state reaction. At higher E_{col}, however, those product ions with low center-of-mass recoil velocities, and therefore high internal energies, should start to dissociate. This effect is clearly seen in the v_{axial} distributions for NO_2H^+ and NO_2D^+ at E_{col} = 0.76 eV. The dashed vertical blue lines near 500 and 1425 m/s lab velocity indicate the limits of this process - ions with higher center-of-mass recoil velocities (i.e., outside the two lines) cannot decompose, while those inside will decompose if most or all of the internal energy is partitioned to the NO_2H^+ or NO_2D^+ product. The odd, flat-topped v_{axial} distributions reflect the fact that much of the NO_2D^+ or NO_2H^+ within the limit lines is missing due to dissociation. The issue of energy partitioning in the products as probed by this dissociation process, is discussed in more detail in the section on vibrational effects.

Charge Transfer

Singlet CT is quite exoergic in this system, and triplet CT is only slightly endoergic. For exoergic CT, a long range electron hopping mechanism is sometimes active, and one signature of this mechanism is product ions created at near-zero laboratory velocities, because the electron carries little momentum. When long-range transfer is efficient, the CT cross section can significantly exceed the hard sphere or capture collision cross sections.[36] Figure 6.5 shows the v_{axial} distributions for the NO_2^+ signal for select E_{col} values. Note the apparent peak at velocities near zero, which ordinarily might be evidence of a long range mechanism. In this case, however, we know that secondary reactions convert slow NO_2H^+ and NO_2D^+ to NO_2^+, which is also expected to be slow.

As a result, some fraction of the near-zero v_{axial} peak is certainly due to this artifact. The contribution of the secondary reaction can easily be tested using the same approach used above to simulate its effect on the NO_2D^+ v_{axial} distribution, and the result is shown in the top frame of the figure. The red curve is a model of the "true" v_{axial} distribution, based on assuming isotropic scattering and adjusting the distribution of recoil velocities to fit the forward-scattered half of the distribution, which is essentially unaffected by the secondary reaction artifact. We then added the contribution from NO_2D^+ and NO_2H^+ products that underwent secondary reaction to generate NO_2^+ (i.e., twice the difference between the red and green curves in Figure 6.3). For this purpose, we also assumed that the resulting NO_2^+ velocity was, on average, identical to that of the NO_2D^+ or NO_2H^+ from which it came. The result is the green curve that fits the experimental data down to ~200 m/sec. Note that the simulation predicts significant intensity of products that are scattered to negative lab velocities, which appear at small but positive velocities in the experiment. If this negative component of the simulation is assumed to contribute to the near-zero peak in the experiment, then the simulation fits the experimental data reasonably well. Furthermore, if we use this process to estimate the value of the "true" integral cross section, the result is in excellent agreement with the experiments done at low pressures (see single data point in Figure 6.2).

The nature of the model used for the "true" distribution in this simulation suggests that CT occurs predominantly in intimate collisions. Because the SC1 complex is weakly bound with respect to products, it is doubtful that it could have a long enough lifetime (> ~1 picosecond) to account for a forward-backward symmetric NO_2^+ v_{axial} distribution.

Note, however, that while complex mediation must result in forward-backward symmetry, the converse is not true (cf. hard sphere scattering). We suggest that CT probably goes by a direct mechanism involving intimate collisions over a range of impact parameters, resulting in a recoil velocity distribution that just happens to look forward-backward symmetric in a measurement of only the axial component, as in our experiment.

The absence of long range CT in this system is not surprising. Long range CT is essentially an electronic transition where the initial and final orbitals happen to be on different centers, thus one requirement is reasonable Franck-Condon (FC) factors connecting the initial state with near-resonant final states. The requirement for near-resonant final states is because there cannot be significant translational ↔ internal energy transfer at long range, because the intermolecular forces are too weak. In this system, HOD bond angle changes by < 4°, and the OH/OD bond lengths change by only ~0.03Å in going from H_2O^+ to H_2O, thus its part of the FC distribution is dominated by the diagonal (vibrational state preserving) transition.[39] In contrast, the ONO bond angle changes from 134.1° in NO_2 to linear in NO_2^+, and the NO bond lengths also decrease by 0.075 Å. For this reason, the NO_2 bend is FC active, as is the symmetric stretch to a lesser extent. Judging from the photoelectron spectrum,[40] the states with good FC factors in the $NO_2 \rightarrow NO_2^+$ transition lie in the range between ~1 and ~2.4 eV above the ground state. The CT exoergicity in this system is 3.03 eV, and as a result, there is poor FC overlap between $HOD^+ + NO_2$ and the near-resonant $HOD + NO_2^+$ states, thus rendering the long range mechanism inefficient.

As E_{col} is increased, the CT v_{axial} distributions shift gradually into the backward hemisphere. This trend is obvious at 1.93 eV, where rapid dissociation of the NO_2H^+ and NO_2D^+ products means that their contribution to the NO_2^+ signal can be neglected. Here, the NO_2^+ peaks near zero lab velocity, but in a very broad distribution extending well forward of V_{cm}. This pattern suggests that CT occurs at the full range of impact parameters ranging from head-on (giving $v_{axial} > V_{cm}$) to grazing (v_{axial} near zero). The fact that the grazing collisions dominate, simply reflects the fact that the probability for colliding at impact parameter b is proprortional to b.

Note that at 2.94 eV, the distribution is narrower (more backward peaked) than at lower energies, even though the energy available to drive recoil is higher. This disappearance of NO_2^+ with v_{axial} near V_{cm} almost certainly indicates the onset of singlet dissociative CT ($NO^+ + O(^1D) + H_2O$), which becomes possible for $E_{col} > 1.78$ eV. This process can only occur for collisions where most of the available energy is partitioned to internal energy of the nascent NO_2^+, i.e., collisions producing NO_2^+ with v_{axial} near V_{cm}.

The remaining question is to what extent the exoergic singlet and endoergic triplet channels contribute to the total CT cross section. From the fact that the NO_2^+ cross section is larger than the singlet collision cross section (Figure 6. 2), even after correction for secondary reaction of NO_2H^+ and NO_2D^+, it is clear that there must be some contribution from triplet CT. At low collision energies, we might expect that triplet CT should be a minor channel on the triplet surface, because it is competing with three lower energy channels (dissociative CT, H^+ and D^+ transfer, and dissociation back to reactants). Because $\sigma_{total} \approx \sigma_{col}$ (Figure 6.2, inset), dissociation back to reactants can be neglected,

but the other competing channels have low energy transition states, and are major channels at low E_{col}. At high E_{col}, triplet CT probably is a reasonably efficient process. As noted above, however, the NO_2^+ (a^3B_2) product ion would predissociate to be detected as NO^+ (+ O (^3P)) unless produced with vibrational excitation <~80 meV.[21] Because relatively hard collisions are required to drive endoergic triplet CT, it seems likely that most of the triplet NO_2^+ produced at high E_{col} would dissociate, and contribute to the NO^+ signal.

In summary, the corrected NO_2^+ production cross section is only ~20% greater than the singlet collision cross section. On the singlet surface, CT is likely to be highly efficient, because it is a facile process that can occur in any collision geometry, and the competing atom transfer channels are either much higher in energy (H^+/D^+ transfer) or likely to occur only in very restricted collision geometries (NO^+ + HOOH). Therefore, the amount of "excess" NO_2^+, that can't be attributed to singlet reactions is small, and likely to be accounted for by the fraction of triplet CT products that produced with low levels of vibrational excitation. There is no compelling need to invoke triplet → singlet transitions during the collisions, presumably because the collision times are much shorter than in the 300 K kinetics experiments.

NO^+ Production

There are five processes that appear to contribute to the NO^+ signal in different energy ranges. Because the NO^+ cross section is roughly double the single collision cross section, it is clear that at least half the NO^+ signal must result from triplet reactions. One process that can only occur on the singlet surface, is O^- abstraction, producing NO^+ +

HOOH. One pathway to this product channel would be formation of the $NO_3H_2^+$ complex, followed by HOOH elimination, and this channel is seen in trajectories starting with highly excited $NO_3H_2^+$. This complex is not likely to form in a statistical mechanism, because it is in competition with a much lower energy, and more facile process - dissociation to CT products. This channel is not likely to be efficient in direct collisions either, because it is likely to occur only in a narrow range of collision geometries, whereas CT has not geometry requirements. To the extent that it does occur, the complex-mediated route would give NO^+ near V_{cm}, and the direct route probably would give NO^+ in a broader distribution about V_{cm} because intimate collisions would be required.

Another minor singlet route to NO^+ is dissociative CT to $NO^+ + O(^1D) + H_2O$, which does appear to occur at high E_{col}, as discussed above. On the other hand, because the CT cross section shows no sign of a significant drop above the threshold for this process (1.78 eV), we conclude that it is too inefficient to enough to make a significant contribution to the NO^+ channel. It would produce NO^+ with recoil velocities near V_{cm}.

The final possible singlet (or triplet) reaction would be H^+ or D^+ transfer, followed by OH or OD elimination from the NO_2H^+ or NO_2D^+ product. This process clearly happens, as discussed above, however, because singlet CT is much more energetically favorable than singlet H^+ or D^+ transfer, we expect that most NO_2H^+ or NO_2D^+ production occurs by triplet reactions. In either case, NO^+ cannot form this way at $E_{col} < \sim 0.55$ eV, but at higher energies there should be NO^+ with v_{axial} in a broad distribution around V_{cm},

because parent NO_2H^+ or NO_2D^+ must have high internal energy, corresponding to low recoil velocity.

On the triplet surface, there are other two reactions that we believe to be responsible for most of the NO^+. The major triplet channel, and the only one open below E_{col} = ~0.55 eV, is almost certainly concerted dissociative CT, mediated by TC1 and controlled by TS3, and as shown by the flow tube results, definitely involving the product-like complex TC3, at least for low collision energies. This process should contribute NO^+ with forward-backward symmetric v_{axial}, however, it is probable that the mechanism becomes direct at high energies, and in that case it is likely that the product ion is backscattered (slow in the lab), because it should be possible in grazing collisions. The sequential triplet dissociative CT mechanism should also be significant, particularly at higher energies. We expect the nascent NO_2^+ (a^3B_2) to be backscattered in the center-of-mass frame (low lab velocity), thus the resulting NO^+ should also be slow in the lab frame.

Based on these dynamical considerations, it is possible to at least partly unravel the contributions from the five possible channels to the NO^+ v_{axial} distributions shown for reaction of ground state HOD^+ in Figure 6.6. At collision energies up to ~0.5 eV, where only concerted triplet dissociative CT, and singlet HOOH elimination are likely to be significant, the distributions show a broad, forward-backward symmetric component. The spike at low lab velocity can be attributed, at least in part, to ions in the main velocity component that scattered at negative lab velocities, and were detected after reflection at the ion guide entrance. For reasons discussed above, we believe that singlet NO^+ + HOOH production is probably not particularly efficient, and therefore the large

NO^+ signal at low E_{col} is mostly attributed to concerted triplet dissociative CT. This channel should produce NO^+ in a forward-backward symmetric velocity distribution, as observed. With increasing E_{col}, the v_{axial} distributions become backward-peaked, although at all energies there is substantial intensity in a broad component near, but not symmetric about V_{cm}. The broad component near V_{cm} is attributed to NO^+ from decomposition of nascent NO_2H^+ and NO_2D^+ products, with a small contribution from singlet dissociative CT. The backscattered NO^+ peak at low lab velocities, is attributed to the combined contributions from concerted and sequential triplet dissociative CT.

Vibrational Effects

Figures 6.7 and 6.8 show the cross sections for the individual channels in reaction of HOD^+ in its 000, 001, 010, and 100 vibrational states. The 001 level has mostly OH stretch character and is the highest energy mode at 397 meV. The 010 level is the bend at 153 meV, and the 100 level has mostly OD stretch character at 293 meV. The effects of vibration are mode specific, quite distinct from the effects of collision energy, and qualitatively different for the different product channels. The NO^+ channel is enhanced by all three modes of excitation, with the largest enhancement from the OH stretch, and intermediate but similar effects from the OD and bend excitations, despite the factor of ~2 difference in energy. The CT channel is inhibited by all modes, but with the largest effect from the lowest energy bend mode. The NO_2H^+ and NO_2D^+ channels are also inhibited by all modes, but the OH and OD stretch modes have different effects for the two channels, giving insight into how reactant vibration couples to product internal energy, as outlined below.

Within experimental error, there is no vibrational effect on σ_{total} at low energies, which is not surprising because $\sigma_{total} \approx \sigma_{col}$. Therefore, the vibrational effects reflect changes in the competition between the various product channels. Above 1 eV, the other modes continue to have negligible effects on total reactivity, however, excitation of the OH stretch results in a ~10 % increase in total cross section.

One might expect that the branching between NO_2D^+ and NO_2H^+ should be mode-dependent, and particularly that excitation of the OH stretch would enhance NO_2H^+, while OD stretch excitation would enhance NO_2D^+. As discussed in the Introduction, such effects were seen for HOD with both overtone and fundamental excitations. In those systems, there are significant barriers to H/D transfer, associated with the need to partially break the OH or OD bond before significant energy is recovered by making the new HH or HCl bonds. Therefore, stretching an OH or OD bond effectively reduces the barrier height for transfer of H or D, respectively. In contrast, H^+/D^+ transfer in this system is essentially thermoneutral, and more importantly, is a barrierless process. The competition between H^+ and D^+ transfer, and of those channels with CT, etc., probably depends to a large extent on the orientation during collision, and whether the reactants come together in singlet or triplet coupling. If the orientation is optimal for H^+ transfer (i.e., ONO-H-OD), then H^+ transfers, collision in ONO-D-OH geometries leads D^+ transfer, and orientations where neither H nor D impact on an O atom in NO_2, presumably lead to CT or NO^+ products.

As discussed above, the strong suppressing effect of E_{col} on the NO_2H^+/NO_2D^+ channels results from dissociation of the nascent product ion, if its internal energy is

greater than the energy required to eliminate OH/OD (~0.53 eV/0.58 eV). HOD^+ vibrational excitation also suppresses the NO_2H^+/NO_2D^+ channels (Figures 6.7 and 6.8), presumably for the same reason, and the mode dependence of this suppression provides insight into how different HOD^+ modes couple to internal energy of the two product moieties. We first consider how vibrational excitation affects the v_{axial} distributions, as shown in the lower frames of Figs. 3 and 4. Results are shown only for the OH and OD stretch modes, both because they have the largest effects on the cross sections, and because they have different effects on the two channels.

Consider the data for NO_2D^+ in the bottom two frames of Figure 6.3. At E_{col} = 0.45 eV there is not enough available energy in the ground state reaction to allow dissociation of the NO_2D^+ product, however, addition of one quantum of either the OH (397 meV) or OD (293 meV) stretch opens this dissociation channel, but only for those collisions where most of E_{avail} is partitioned to internal energy. These correspond to collisions with v_{axial} near V_{cm}, and the two vertical lines symmetrically displaced from V_{cm} enclose the region where dissociation is possible for OH excitation. Clearly, over this region of the recoil velocity distribution, the intensities from OH or OD excited reactions are significantly reduced. It is interesting to note that the attenuation from OD stretch excitation is actually larger than that from the OH stretch, even though the OH stretch corresponds to ~13% higher E_{avail} (35% higher vibrational energy) than the OD stretch. In contrast, the analogous result for the NO_2H^+ channel (Figure 6.4, 3rd frame) shows that the OH stretch causes larger attenuation than the OD stretch. At E_{col} = 0.76 eV, the products from the ground state reaction can dissociate for v_{axial} inside the pair of blue vertical lines, and the

brown lines show the limits for the OH stretch excited reaction. The same mode dependent attenuations are observed here.

It is useful to think about the OH vs. OD stretch effects in terms of stretching the bond that breaks, vs. the spectator bond, i.e., the bond in the OH or OD product. One might expect that energy initially deposited in the bond that breaks should be more efficiently channeled into internal energy of the NO_2D^+ or NO_2H^+ product, while excitation in the spectator bond might tend to remain as vibrational excitation of the OH or OD product. The mode effects on the v_{axial} distributions show just this effect, as do the data in Figure 6.7. Note that for several E_{col} points, where E_{col} is well below the energy required for dissociation of the NO_2D^+ or NO_2H^+ products, the largest attenuation comes from OH stretch excitation, presumably because it can make the largest contribution to destabilizing the products. With increasing E_{col}, the attenuations become quite mode-dependent. For NO_2D^+, excitation of the OD stretch (bond that breaks) gives the largest attenuation, and excitation of the "spectator" OH stretch has a smaller effect, even though its energy is 35% greater. For NO_2H^+, the OD bond is the spectator, and as expected exciting this stretch has a much smaller effect than exciting the OH stretch. In fact, at 1 eV and above, exciting the spectator stretch has no effect at all, whereas the stretch of the bond that breaks continues to destabilize the product.

The effect of bend excitation, is less clear, partly because this is a significantly lower energy excitation, and thus does not have a large effect on the energy available to destabilize the NO_2D^+ and NO_2H^+ products. In general, the bend causes a small

suppression of the product signals, roughly in line with the effect that results from adding an equivalent amount of collision energy.

All HOD^+ modes inhibit CT (Figure 6.8, top) for $E_{col} < 1$ eV, with the largest effect from the bend - the lowest frequency mode by a large margin. The large inhibition at low energies is partly due to the fact that survival of NO_2H^+ and NO_2D^+ is reduced by vibrational excitation, and secondary reaction of these product ions is a significant contributor to the NO_2^+ signal. As shown in Figure 6.7, the OH and OD stretch modes have the largest effect on NO_2H^+ and NO_2D^+ survival, and this secondary reaction probably explains the small inhibitory effect on the NO_2^+ cross section at low E_{col}. Note, however, that bend excitation, because its energy is low, has relatively little effect on NO_2H^+ and NO_2D^+ survival, but has the largest effect on the NO_2^+ signal, thus we conclude that bend excitation really does inhibit CT in this system. This conclusion is supported by the fact that at high E_{col}, where the secondary reaction contribution is negligible, the OH and OD stretch effects become negligible, but the bend continues to inhibit CT.

It is not clear why HOD^+ bend excitation might inhibit CT, because there is little geometry change in the $HOD^+ \rightarrow HOD$ process, and thus no reason to expect that the efficiency should depend on the bend angle. As noted, however, the total cross section is neither enhanced nor inhibited by bend excitation, thus the effect may simply result from a bend enhancement of a competing channel. The only possibility for this role is the NO^+ production cross section, which is enhanced by bend excitation.

As discussed above, the NO^+ channel has potential contributions from up to five processes occurring on both singlet and triplet surfaces. It is inhibited by E_{col} and is the only channel enhanced by vibration. All three modes enhance NO^+ production, with the largest effect from the OH stretch, and similar smaller effects from the bend and OD stretch modes. It is clear that a significant fraction of the enhancement, particularly that from OH and OD stretch excitation, results from the effects of stretching the "bond that breaks" on the dissociation of NO_2H^+ and NO_2D^+ products:

$$NO_2H^+ \rightarrow NO^+ + OH \qquad \text{and} \qquad NO_2D^+ \rightarrow NO^+ + OD.$$

The effects at low E_{col}, where enough NO_2H^+ and NO_2D^+ survive to be detected, can be seen in Figure 6.7. Note that in the low E_{col} range, the bend has a smaller effect on NO_2H^+ and NO_2D^+ dissociation than either stretch, yet the enhancement in the NO^+ signal is comparable to that from the OD stretch. That indicates that there is a real enhancement in NO^+ production from HOD^+ bend excitation, beyond that from enhancing dissociation of NO_2H^+ and NO_2D^+. In this low energy range, we believe that the other significant NO^+ production processes include triplet dissociative CT, and possibly singlet HOOH elimination. It is not clear why bend excitation might enhance either of these reactions.

At high E_{col}, any NO_2H^+ or NO_2D^+ that is still formed is all dissociated to $NO^+ + OH$, regardless of HOD^+ vibrational excitation, thus this NO^+ enhancement mechanism is no longer active. The fact that the effect of OD stretch excitation also dies out at high E_{col} suggests that this may have been the only enhancement mechanism for this mode. It is interesting that the OH stretch continues to enhance NO^+ production in the high E_{col}

range, and this is also the only case where there is an enhancement of σ_{total}. We speculate that OH stretch excitation somehow enhances the probability of NO^+ production in grazing impact parameter collisions, such that the total cross section increases. The NO^+ production channels most likely to be enhanced at high E_{col} are dissociative CT on the singlet and triplet surfaces or formation, and subsequent predissociation of triplet NO_2^+. The fact that the enhancement in σ_{total} appears starting at ~1 eV, suggests that singlet dissociative CT is probably not responsible (threshold energy = 1.78 eV). The conclusion, then, is that some form of triplet dissociative CT is enhanced by OH stretch excitation.

Conclusions

This is a complex reaction, with nine channels on singlet and triplet surfaces resulting in five distinguishable products masses. Nonetheless, by comparing cross section magnitudes with the singlet and triplet collision cross sections, examining the recoil dynamics, and comparing to thermal energy kinetic measurements, we are able to largely sort out the branching between all the pathways.

Because NO^+ + HOOH production involves tight and high energy transition states, we infer that it is probably a minor singlet channel. The dominant singlet channel is clearly CT, which may, in fact, account for nearly 100% of the branching on the singlet surface. There also may be some H^+ and D^+ transfer on the singlet surface, however, the reaction coordinate in Figure 6.1 suggests that these reactions probably mostly result from triplet coupled reactions. On the triplet surface, the dominant product channel is clearly NO^+ production, appears to have significant contributions from dissociative CT,

predissociation of the triplet CT product ion, and from dissociation of NO_2H^+ and NO_2D^+ products that have internal excitation above the threshold for OH/OD elimination.

HOD^+ vibrational excitation affects branching between the channels, but has little effect on the overall reactivity, which is near the collision limit at the energies probed in the beam experiments. Vibrational energy put into the bond that breaks in H^+ or D^+ transfer, is shown to end up as internal energy of the NO_2H^+ or NO_2D^+ product, whereas energy in the spectator bond does not, presumably indicating that energy remains in the OH or OD product.

Motivated by apparent problems with previous thermal kinetic measurements in the literature, we remeasured the thermal energy rates for this system. The results are consistent with the reaction coordinate in Figure 6.1. The main differences between the thermal and beam measurements are that long complex lifetimes on the triplet surface allow significant triplet →singlet conversion in the thermal measurements, and that $NO^+(H_2O)$ is seen as a product in the thermal measurement, resulting from collisional stabilization of this complex in TC3. In the beam experiment, the internal energy of this complex is apparently always too high for it to survive without stabilizing collisions, and the product detected is NO^+. In addition, the thermal measurements do not see NO_2H^+ or NO_2D^+, presumably because collisions on the triplet surface that trap into the TC1 complex, instead result in production of $NO^+(H_2O)$, while for the higher available energy range probed in the beam experiments, the higher energy, but more facile H^+/D^+ transfer reaction is significant.

References

1. M. J. Bronikowski, W. R. Simpson, B. Girard, R. N. Zare, J. Chem. Phys. 95, 8647 (1991).

2. Bronikowski, M. J.; Simpson, W. R.; Zare, R. N. J. Phys. Chem. 97, 2204 (1993).

3. Bronikowski, M. J.; Simpson, W. R.; Zare, R. N. J. Phys. Chem. 97, 2194 (1993).

4. A. Sinha, M. C. Hsiao, F. F. Crim, J. Chem. Phys. 92, 6333 (1990).

5. A. Sinha, J. D. Thoemke, F. F. Crim, J. Chem. Phys. 96, 372 (1992).

6. R. B. Metz, J. D. Thoemke, J. M. Pfeiffer, F. F. Crim, J. Chem. Phys. 99, 1744 (1993).

7. J. D. Thoemke, J. M. Pfeiffer, R. B. Metz, F. F. Crim, J. Phys. Chem. 99, 13748 (1995).

8. A. Sinha, M. C. Hsiao, F. F. Crim, J. Chem. Phys. 92, 6333 (1990).

9. P. B. Armentrout, J. J. Simons, Am. Chem. Soc. 114, 8627 (1992).

10. I. Dotan, W. Lindinger, B. Rowe, D. W. Fahey, F. C. Fehsenfeld, D. L. Albritton, Chem. Phys. Lett. 72(1), 67 (1980).

11. R. J. Shul, R. Passarella, L. T. DiFazio Jr., R. G. Keesee, A. W.Castleman, Jr. J. Phys. Chem. 92, 4947 (1988).

12. Y.-H. Chiu, H. Fu, J.-T. Huang, S. L. Anderson, J. Chem. Phys. 102, 1188 (1995).

13. J. Liu, H.-T. Kim, S. L. Anderson, J. Chem. Phys. 114, 9797 (2001).

14. B. W. Uselman, J. M. Boyle, S. L. Anderson, Chemical Physics Letters 440, 171 (2007).

15. *CRC Handbook of Chemistry and Physics*, edited by R. C. Weast, M. Astle, J., and W. H. Beyer (CRC Press, Boca Raton, 1985).

16. F. R. Ornellas, S. M. Resendeb, F. B. C. Machado, O. J. Roberto-Neto, Chem. Phys 118, 6 (2002).

17. A. A. Viggiano, R. A. Morris, F. Dale, J. F. Paulson, K. Giles, D. Smith, T. J. Su, Chem. Phys 93, 1149 (1990).

18. M. J. Frisch, G. W. Trucks, H. B. Schlegel, G. E. Scuseria, M. A. Robb, J. R. Cheeseman, J. J. A. Montgomery, T. Vreven, K. N. Kudin, J. C. Burant, J. M. Millam, S. S. Iyengar, J. Tomasi, V. Barone, B. Mennucci, M. Cossi, G. Scalmani, N. Rega, G. A. Petersson, H. Nakatsuji, M. Hada, M. Ehara, K. Toyota, R. Fukuda, J. Hasegawa, M. Ishida, T. Nakajima, Y. Honda, O. Kitao, H. Nakai, M. Klene, X. Li, J. E. Knox, H. P. Hratchian, J. B. Cross, C. Adamo, J. Jaramillo, R. Gomperts, R. E. Stratmann, O. Yazyev, A. J. Austin, R. Cammi, C. Pomelli, J. W. Ochterski, P. Y. Ayala, K. Morokuma, G. A. Voth, P. Salvador, J. J. Dannenberg, V. G. Zakrzewski, S. Dapprich, A. D. Daniels, M. C. Strain, O. Farkas, D. K. Malick, A. D. Rabuck, K. Raghavachari, J. B. Foresman, J. V. Ortiz, Q. Cui, A. G. Baboul, S. Clifford, J. Cioslowski, B. B. Stefanov, G. Liu, A. Liashenko, P. Piskorz, I. Komaromi, R. L. Martin, D. J. Fox, T. Keith, M. A. Al-Laham, C. Y. Peng, A. Nanayakkara, M. Challacombe, P. M. W. Gill, B. Johnson, W. Chen, M. W. Wong, C. Gonzalez, and J. A. Pople, (Gaussian, Inc., Pittsburgh PA, 2003).

19. W. L. Hase, K. Bolton, P. de Sainte Claire, R. J. Duchovic, X. Hu, A. Komornicki, G. Li, K. Lim, D. Lu, G. H. Peslherbe, K. Song, K. N. Swamy, S. R. Vande Linde, A. Varandas, H. Wang, and R. J. Wolf, VENUS99: A general chemical dynamics computer program (1999).

20. V. Bakken, J. M. Millam, H. B. Schlegel, J. Chem. Phys. 111, 8773 (1999).

21. K. Shibuya, S. Suzuki, T. Imamura, I. J. Koyano, Phys. Chem. A 101, 685 (1997).

22. E. P. Hunter, S. G. Lias, J. Phys. Chem. Ref. Data (1998).

23. A. P. Scott, L. J. Radom, Phys. Chem. 100, 16502 (1996).

24. H. Y. Afeefy, J. F. Liebman, and S. E. Stein, in *NIST Chemistry WebBook, NIST Standard Reference Database Number 69*, edited by W. G. Mallard and P. J. Linstrom (National Institute of Standards and Technology (http://webbook.nist.gov), Gaithersburg MD, 2000).

25. S. G. Lias, J. E. Bartmess, J. F. Liebman, J. L. Holmes, R. D. Levin, and W. G. Mallard, in *NIST Chemistry WebBook, NIST Standard Reference Database Number 69*, edited by W. G. Mallard and P. J. Linstrom (National Institute of Standards and Technology, Gaithersburg MD 20899 (http://webbook.nist.gov). 2000).

26. F. C. Fehsenfeld, C. J. Howard, A. L. Schmeltekopf, J. Chem. Phys. 63, 2835 (1975).

27. Anicich, V. G. *An Index of the Literature for Bimolecular Gas Phase Cation-Molecule Reaction Kinetics* (National Aeronautics and Space Administration, and Jet Propulsion Laboratory,California Institute of Technology: Pasadena, California, 2003).

28. A. A. Viggiano, S. T. Arnold, R. A. Morris, Int. Rev. in Phys. Chem. 17, 147 (1998).

29. L. Zhu, W. L. Hase, A general RRKM program; Quant. Chem. Prog. Exchange, QCPE 644.

30. J. Troe, Chem. Phys. Lett. 122, 425 (1985).

31. R. D. Levine, Bernstein, R. B. *Molecular Reaction Dynamics and Chemical Reactivity* (Oxford University Press: New York, 1987).

32. N. F. Ramsey, *Molecular Beams* (Oxford University Press: New York, 1956).

33. Y.-H. Chiu, H. Fu, J.-T. Huang, S. L. Anderson, J. Chem. Phys. 102, 1199 (1995).

34. Y.-H. Chiu, H. Fu, J.-T. Huang, S. L. Anderson, J. Chem. Phys. 105, 3089 (1996).

35. J. Qian, H. Fu, S. L. Anderson, J. Phys. Chem. 101, 6504 (1997).

36. J. Liu, B. Van Devener, S. L. Anderson, Journal of Chemical Physics 121, 11746 (2004).

37. J. Liu, B. Uselman, B. Van Devener, S. L. Anderson, Journal of Physical Chemistry A 108, 9945 (2004).

38. K. Honma, P. B. Armentrout, J. Chem. Phys. 121, 8307 (2004).

39. K. Kimura, S. Katsumata, Y. Achiba, T. Yamazaki, Iwata, S. *Handbook of HeI Photoelectron Spectra of Fundamental Organic Molecules* (Japan Scientific Societies Press: Tokyo, 1981).

40. P. Baltzer, L. Karlsson, B. Wannberg, D. M. Holland, M. A. MacDonald, M. A. Hayes, J. H. D. Eland, Chemical Physics, 237, 451 (1998).

Table 6.1. Experimental and *ab initio* energies (eV) relative to reactants ($H_2O^+ + NO_2$)

	PBE1PBE/6-311++g**	G3 (0 K)	QCISD(T)/cc-pvtz	Experimental
$NO_2^+(X^1\Sigma_g^+) + H_2O$	-2.59	-2.87	-3.11	-3.03
$NO_2^+(a^3B_2) + H_2O$	0.40	0.36		0.17
$NO_2H^+ + OH$	0.13	0.09	0.01	0.012
$NO^+ + HOOH$	-0.81	-1.47	-1.70	-1.67
$NO^+ + 2OH$	1.05	0.52	0.51	0.55
$NO^+ + O(^3P) + H_2O$	0.47	-0.01	0.65	-0.18
SC1	-3.44	-3.75	-3.97	
TC1	-1.40			
TS1	-1.11		-1.38	
TS2	-0.95			
TS3	-0.48			
TC2	-1.12			
TC3	-0.82			

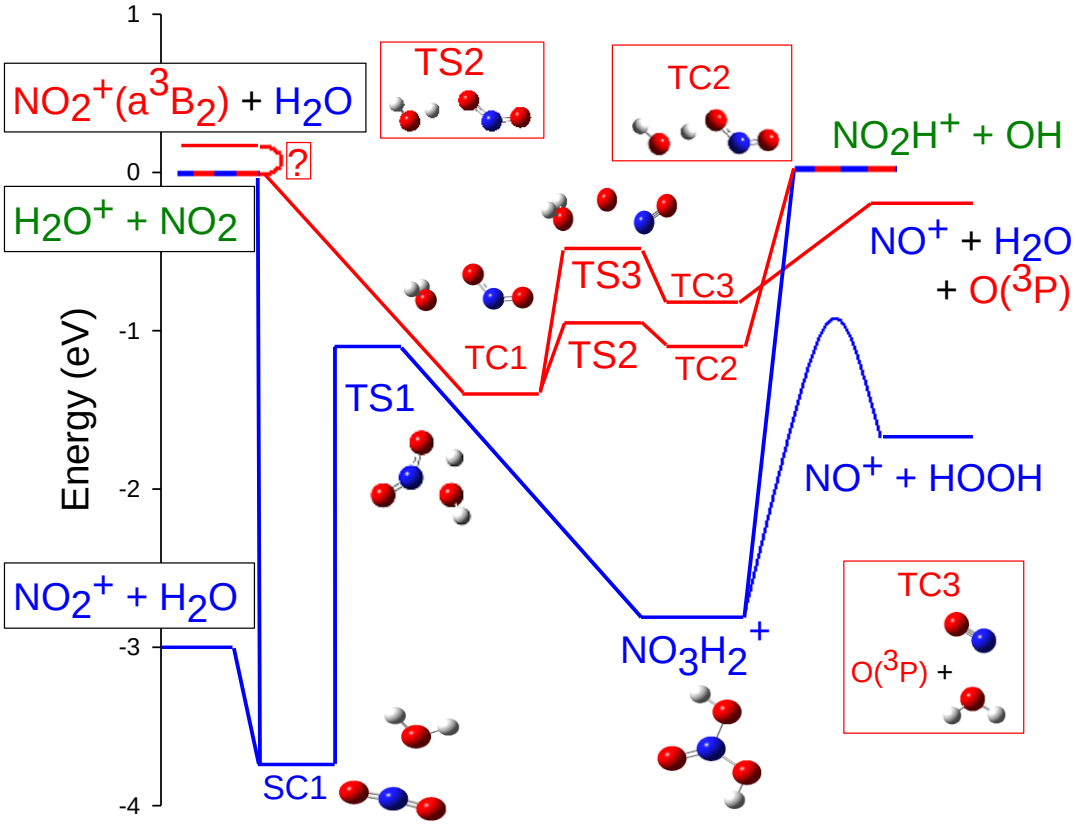

Figure 6.1. Reaction coordinate for the $H_2O^+ + NO_2$ system. Blue indicates species and reaction coordinates that are singlets, red indicates triplets, and green indicates doublets.

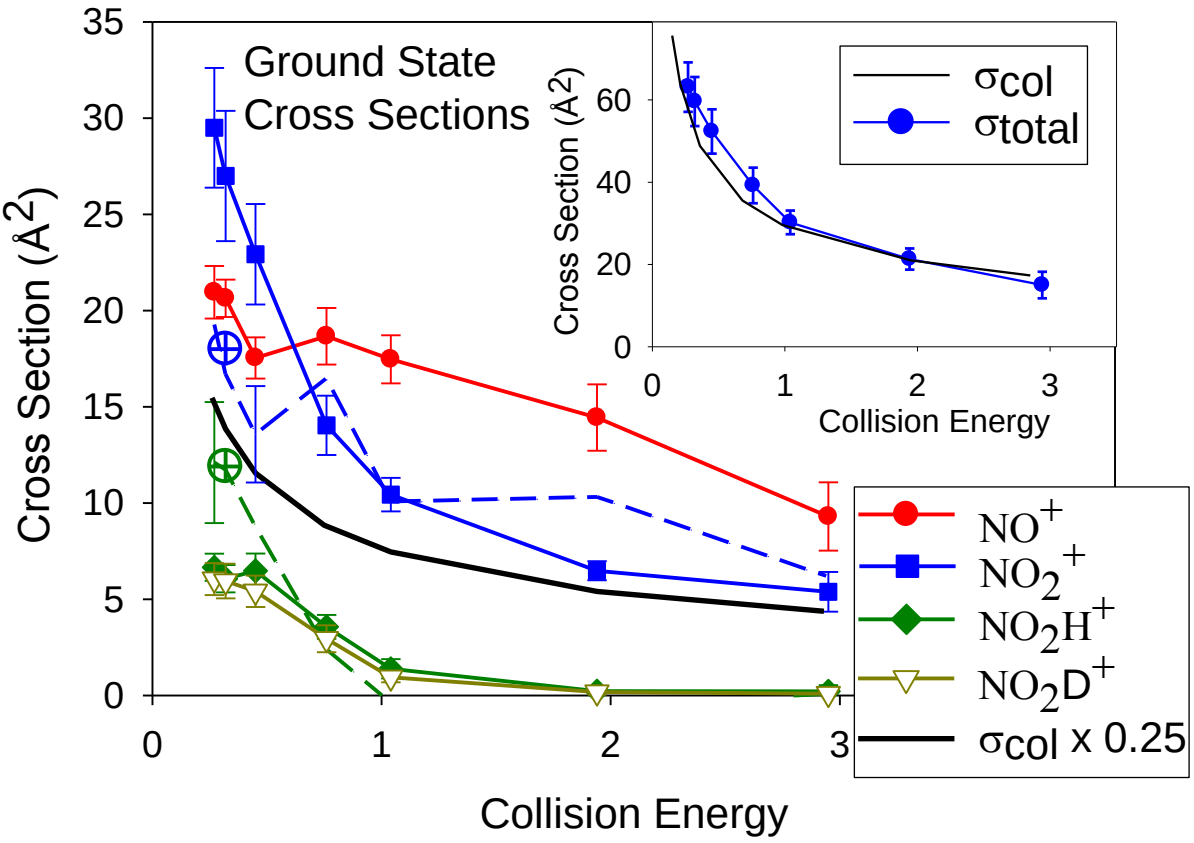

Figure 6.2. Integral cross sections for production of NO_2^+, NO^+, NO_2H^+ and NO_2D^+ in reaction of ground state H_2O^+ with NO_2. The dashed lines are low pressure measurements and the circled cross data points are integral cross sections extracted from simulation accounting for ion survival. The inset compares the total reaction cross section (σ_{total}) with the collision cross section (σ_{col}).

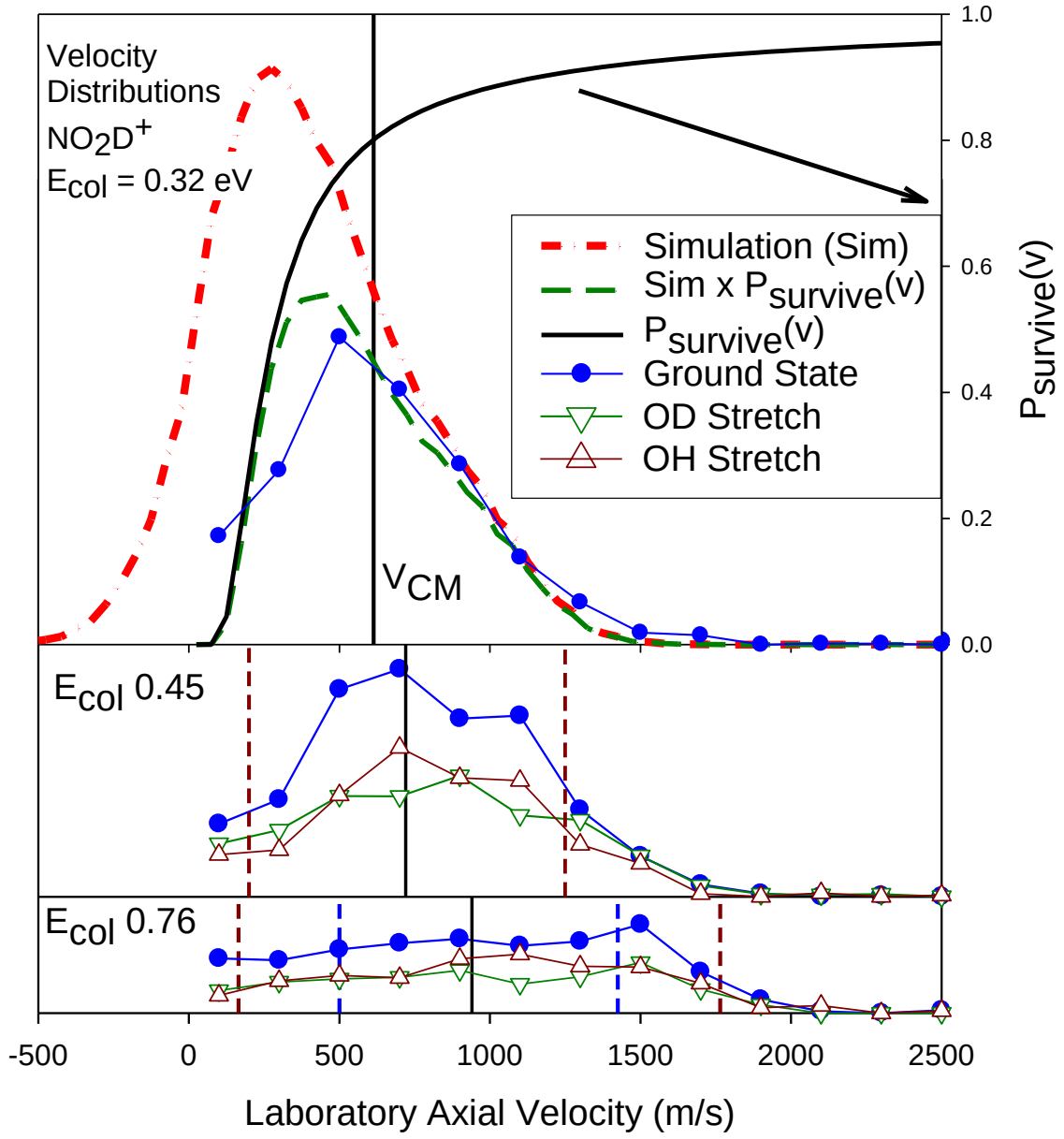

Figure 6.3. Lab frame v_{axial} distributions for the NO_2D^+ product, scaled to be proportional to the integral cross section for each energy and vibrational state. Points are experimental, the smooth red dash-dot curve is from simulations, and the green dashed line is the simulation multiplied by the survival probability ($P_{survive}$). The heavy vertical line in each frame indicates the lab velocity of the center-of-mass frame ($<V_{cm}>$), and the dashed vertical lines give the recoil velocity limits for NO_2D^+ dissociation for ground state and OH stretch-excited HOD^+.

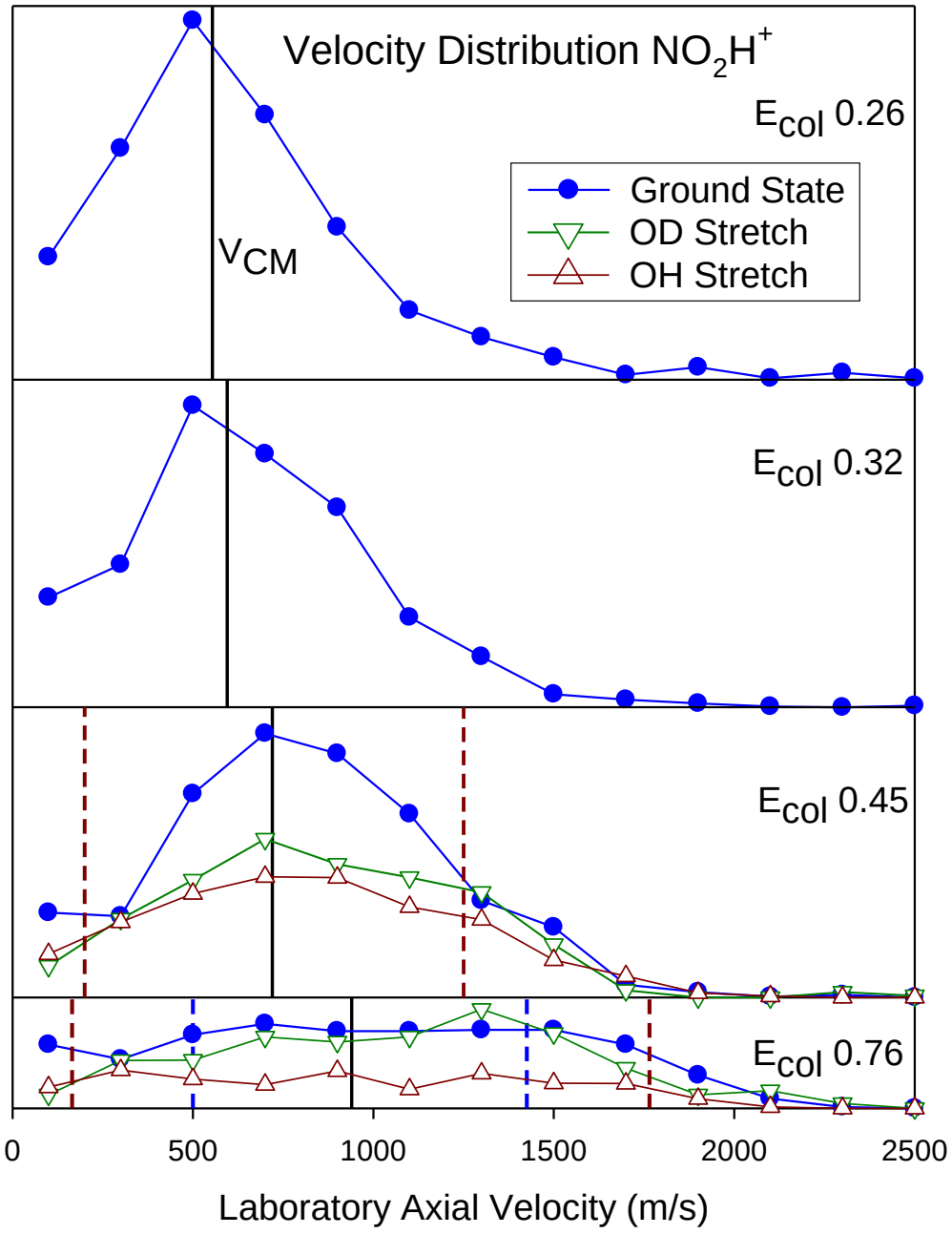

Figure 6.4. Lab frame v_{axial} distributions for the NO_2H^+ product, scaled to be proportional to the integral cross section for each energy and vibrational state. The heavy vertical line in each frame indicates the lab velocity of the center-of-mass frame ($<V_{cm}>$), and the dashed vertical lines give the recoil velocity limits for NO_2H^+ dissociation for ground state and OH stretch-excited HOD^+.

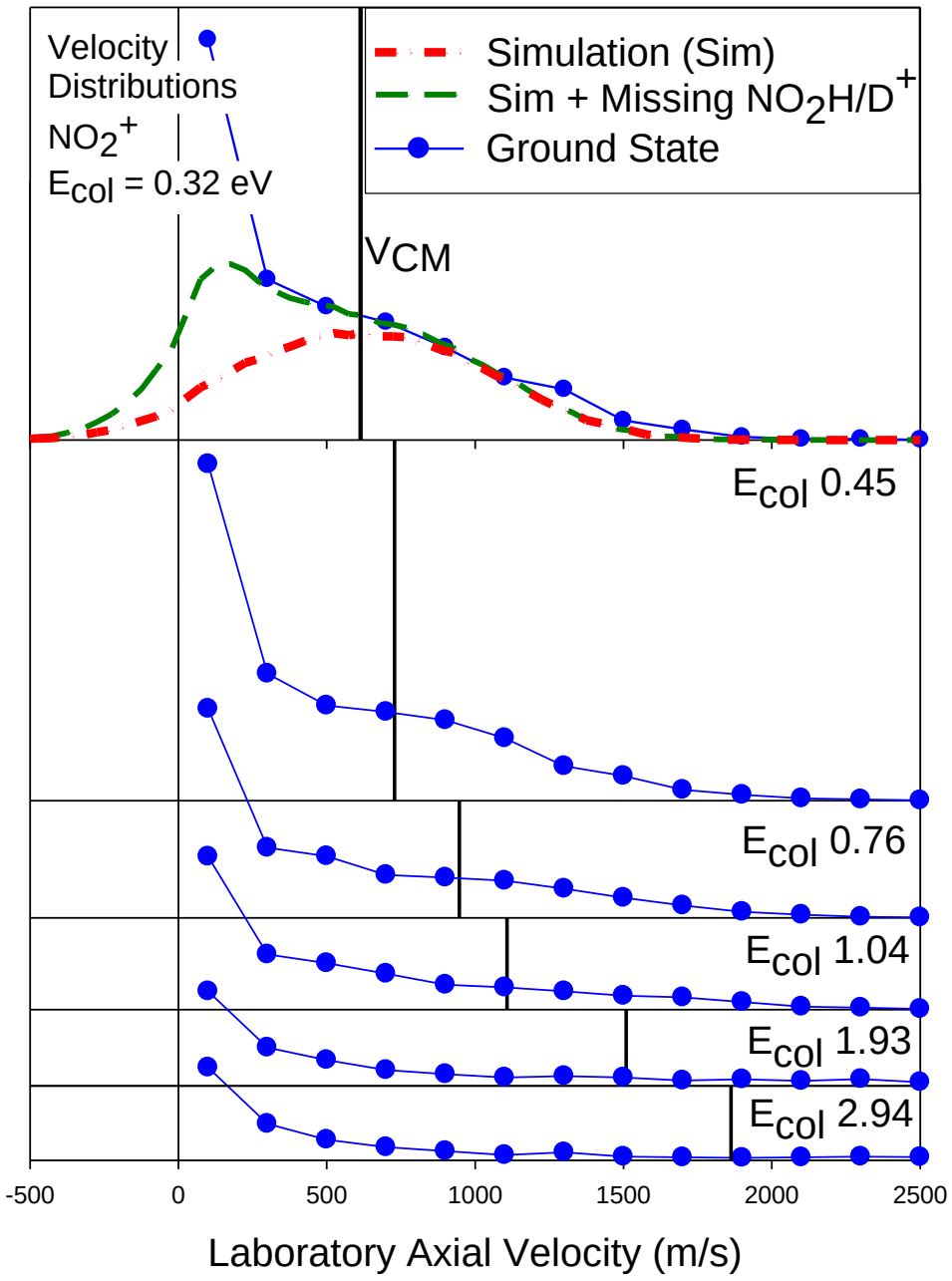

Figure 6.5. Lab frame v_{axial} distributions for the NO_2^+ product, scaled to be proportional to the integral cross section for each energy and vibrational state. Points are experimental, the smooth red dash-dot curve is from simulations, and the green dashed line is the simulation plus the fraction of the NO_2D^+ and NO_2H^+ products that are converted to NO_2^+ by secondary reactions. The heavy vertical line in each frame indicates the lab velocity of the center-of-mass frame ($<V_{cm}>$).

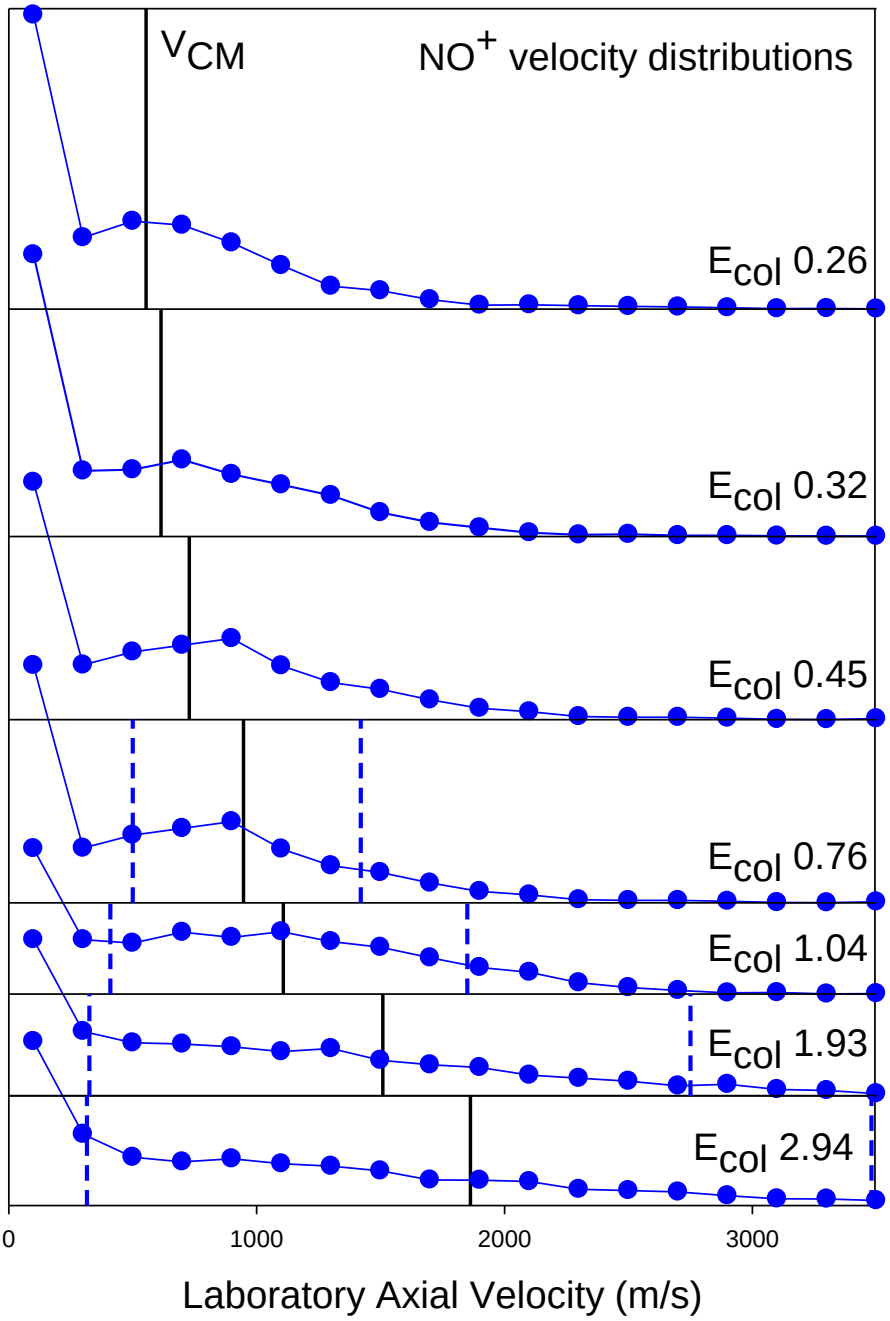

Figure 6.6. Lab frame v_{axial} distributions for the NO^+ product, scaled to be proportional to the integral cross section for each energy and vibrational state. The heavy vertical line in each frame indicates the lab velocity of the center-of-mass frame ($<V_{cm}>$), and the dashed vertical lines give the recoil velocity limits for NO_2H^+ dissociation for ground state HOD^+.

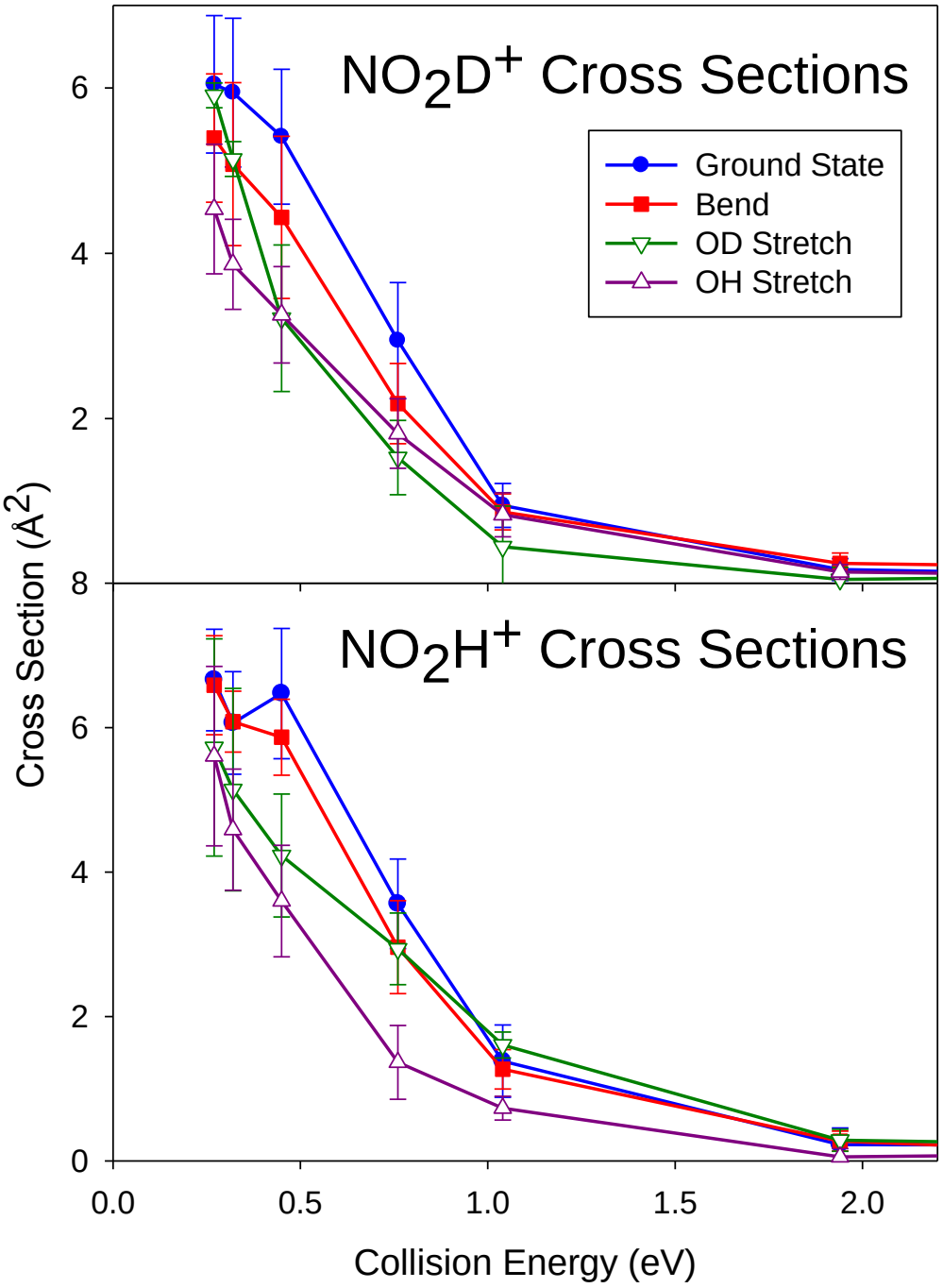

Figure 6.7. Effects of different HOD^+ vibrational levels on the cross sections for NO_2D^+ (top frame) and NO_2H^+ (bottom frame).

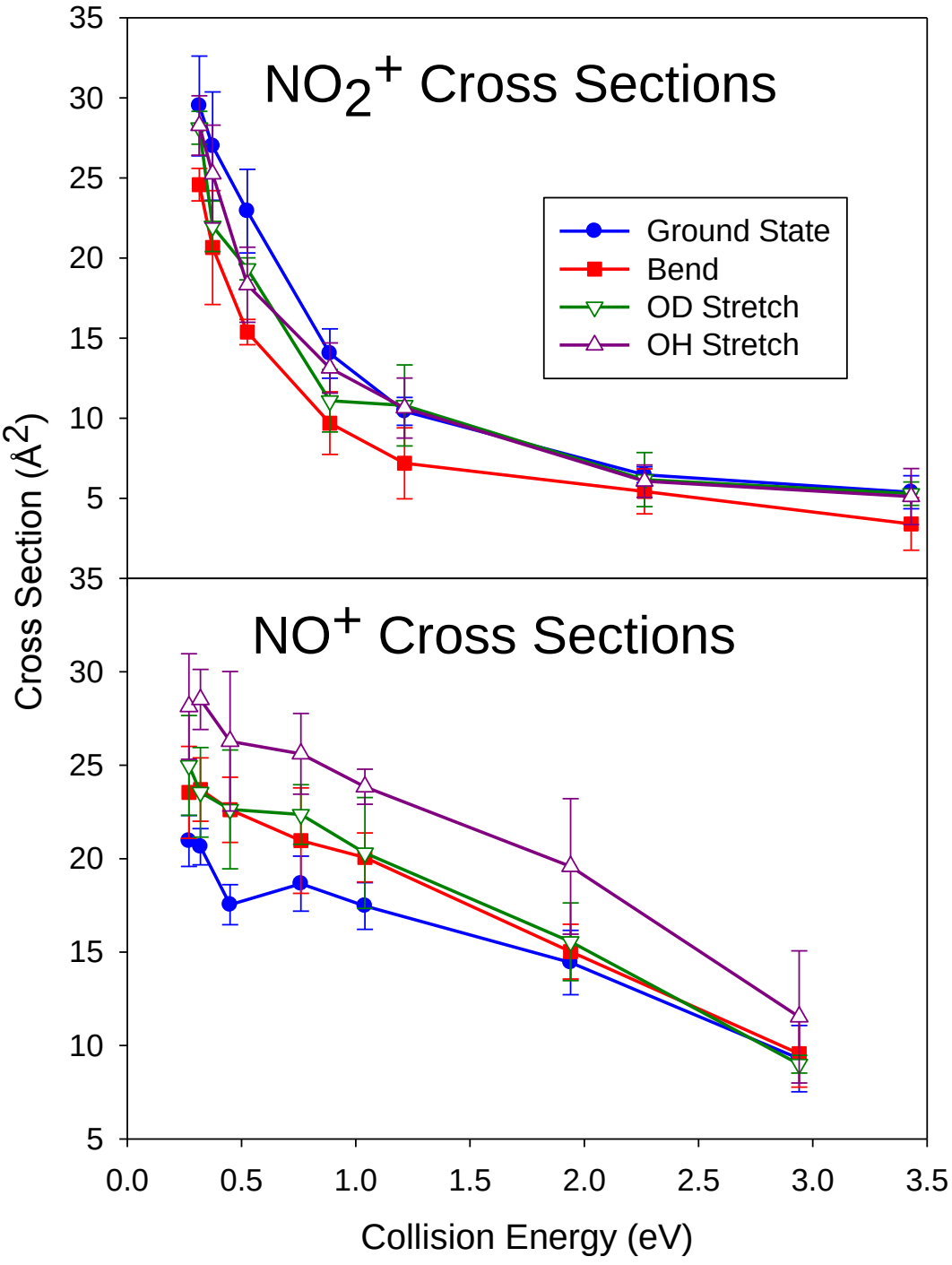

Figure 6.8. Effects of different HOD^+ vibrational levels on the cross sections for NO_2^+ (top frame) and NO^+ (bottom frame).